UNIVERSITY OF CALIFORNIA, SAN DIEGO

Synthesis, Deposition and Characterization of Ferroelectric Films for Electrooptic Devices

A dissertation submitted in partial satisfaction of the

requirements for the degree Doctor of Philosophy in

Materials Science

by

Bahadir Tunaboylu

Committee in charge:

Professor Sadik C. Esener, Chair
Professor Joanna McKittrick
Professor Marc A. Meyers
Professor Peter Asbeck
Professor Massoud Simnad

1997

Copyright

Bahadir Tunaboylu, 1997

All rights reserved.

The dissertation of Bahadir Tunaboylu is approved, and it is acceptable in quality and form for publication on microfilm:

Marc Frotté Meyers

Massoud Sivand

Peter Asbeck

Chair

University of California, San Diego

1997

To

My Family

Table of Contents

Signature Page iii
Dedication iv
Table of Contents v
List of Figures and Tables vii
Acknowledgments xi
Vita and Publications xiii
Abstract xv

1. Introduction 01

1.1 Spatial light modulators for optoelectronic computing 01
1.2 Ferroelectric materials for SLMs 07
1.2.1 Ferroelectrics 07
1.2.2 Electrooptic effect 14
1.3 Integration technologies for Si/Ferroelectric SLM 18
References 24

2. PLZT ceramics : Background 26

2.1 Bulk properties 26
2.1.1 Phase diagram and crystal structure 30
2.1.2 Microstructure and secondary phases 32
2.2 Electrical and electrooptic properties 35
2.2.1 Dielectric properties 35
2.2.2 Optical properties 40
2.2.3 Electrooptic properties 44
References 51

3. PLZT thin films 53

3.1 Summary of previous work 53
3.2 Thin-film deposition methods 59
3.3 Sputtering techniques and RF triode magnetron sputtering 62
References 67

4. This work : Growth, structural and microstructural characteristics of magnetron sputtered PLZT thin film 71

4.1 Experimental : Deposition of PLZT 9/65/35 films 72
4.2 Phase transformation kinetics 80
4.3 Thin film characteristics 87
4.3.1 Composition and crystal structure 87
4.3.2 Microstructure 98
References 110

5. This work : Characterization of dielectric, optical and electrooptic properties of PLZT 9/65/35 films on sapphire 112

5.1 Electrical properties 112
5.1.1 Measurements by an IDE structure 112
5.1.2 Results of dielectric property characterization of PLZT films on sapphire 114
5.2 Optical properties 129
5.3 Electrooptic properties of PLZT films 134
References 143

6. KTN 145

6.1 Background : Crystal properties 145
6.1.1 Phase diagrams and crystal structure 147
6.1.2 Dielectric, optical and electrooptic properties of KTN crystals 151
6.2 Previous work in KTN thin films 158
References 162

7. This work : Synthesis of sol-gel KTN and deposition of KTN thin films by sol-gel and magnetron sputtering 165
7.1 Sol-gel derived KTN 166
7.1.1 Sol-gel synthesis 166
7.1.2 Experimental : Preparation of the precursor solutions of KTN 168
7.1.3 Calcination and annealing 170
7.1.4 Hot isostatic pressing (HIP) 171
7.1.5 Preparation of thin films 172
7.1.6 Thermal analysis and crystallization of powders 173
7.1.7 Results obtained from hot-isostatic pressing of powders 177
7.2 Sol-gel derived KTN thin films 179
7.3 Magnetron sputtered KTN films 181
7.3.1 Composition and structure of sputtered KTN films 183
7.3.2 Electrical and optical properties of sputtered KTN films 186
References 194

8. Summary and conclusions 195

Appendix 201

List of Figures and Tables

Chapter I

Figure 1.1 A generic free-space optical interconnection system. 02
Table 1.1 Comparison of leading electrooptic modulator materials. Assuming E = 2 V/μm. 06
Figure 1.2 Frequency dependence of several contributions to the polarizability [7].....09
Figure 1.3 A typical ferroelectric hysteresis loop [7]. 12
Figure 1.4 Optical phase retardation in an activated PLZT electrooptic ceramic [10]. ...17
Figure 1.5 Hybrid bulk ferroelectric Si/PLZT SLM [12]. 19
Figure 1.6 Cross section of ferroelectric thin film SLM on sapphire....20

Chapter II

Figure 2.1 Perovskite ABO_3 crystal structure of PLZT (La/Zr/Ti : 9/65/35)....29
Figure 2.2 Room temperature phase diagram of PZT and PLZT system....31
Figure 2.3 Phase diagram of PLZT system showing La concentration levels for various compositions [2]....32
Figure 2.4 Pyrochlore structure of general formula $A_2B_2O_7$ showing the 6 fold coordination of B and 8 fold coordination of A atoms [9]. 34
Figure 2.5 Dielectric constant as a function of temperature for PLZT compositions with a 65:35 Zr/Ti ratio [5]. 37
Figure 2.6 Hysteresis loops (P vs E) of the different types of PLZT [5]. 39
Figure 2.7 Optical and infrared transmission versus wavelength of PLZT 9/65/35 [5]...41
Figure 2.8 Dispersion of refractive index and absorption coefficient in bulk PLZT [13]42
Figure 2.9 Birefringence of bulk PLZT versus electric field at 25°C [15]....45
Figure 2.10 Optical index ellipsoid of cubic PLZT with applied electric field. 48
Figure 2.11 Electrooptic effect in PLZT 9.5/65/35 [18]. 49

Chapter III

Table 3.1 FE thin film deposition methods. Scale 1-worst, 10-best [56]. 60

Chapter IV

Figure 4.1 RF triode magnetron sputtering system....73
Figure 4.2 Triode sputtering unit. 74
Table 4.1 Sputtering conditions. 76
Figure 4.3 The chart describing basic deposition and annealing schedule of PLZT thin films. 79
Figure 4.4 Avrami plots of $\ln\ln (1/1-x_t)$ against ln t for four different annealing temperatures....84
Figure 4.5 Arrhenius plot of rate constant k of first-order equation....85
Figure 4.6 Film lead content as a function of substrate temperature using hot-pressed single PLZT oxide targets with excess PbO. 88

Figure 4.7 RBS spectrum of stoichiometric PLZT 9/65/35 film on sapphire. The post-annealing film thickness is 0.44 μm. 90
Figure 4.8 RBS spectrum of stoichiometric PLZT 9/65/35 film on sapphire. (700°C for 1 h). 91
Figure 4.9 RBS spectra of as-deposited PLZT films on Pt/Si. 91
Figure 4.10 X-ray diffraction pattern of as-deposited PLZT thin film on saphire indicating a amorphous phase. 93
Figure 4.11 XRD patterns of PLZT/sapphire showing the perovskite phase (indexed) after RTA treatment at 730°C for 3 min. 93
Figure 4.12 The transformation of pyrochlore/amorphous PLZT to perovskite as a function of RTA temperature. The conditions: 2 min soak, N_2:O_2 atmosphere. 94
Figure 4.13 X-ray diffraction patterns of PLZT films rapid thermally annealed at 625°C, soaked from 11/2 min up to 10 min. 96
Table 4.2 Annealing temperature and the FWHM of perovskite phase. 97
Figure 4.14 XRD pattern of PLZT film deposited at 480°C and then furnace annealed...98
Figure 4.15 SEM micrographs of as-deposited PLZT thin film on r-sapphire (a) and Pt/Si (b). 100
Figure 4.16 Atomic force microscopy images showing surface topology of PLZT 9/65/35 films on r-sapphire (a) as-deposited and (b) annealed. 101
Figure 4.17 AFM of PLZT film on Pt/Si substrate (as-deposited). 102
Figure 4.18 Nanocrystalline islands of pyrochlore are nucleated in an amorphous matrix in as-deposited PLZT film on sapphire. 103
Figure 4.19 The micrographs of PLZT film after rapid thermal annealing at 550°C for 2 min. 103
Figure 4.20 SEM micrograph of furnace annealed PLZT film (700°C, 30 min). 104
Figure 4.21 SEM micrographs of PLZT films on sapphire post-RTA at 725°C for 15 sec (a), 60 sec (b) and 180 sec (c). 105
Figure 4.22 Micrograph of PLZT film furnace annealed at 750°C for 5 h illustrating an average grain size of 1.6-1.7 μm with pores on the grain boundaries 106
Figure 4.23 SEM micrographs of annealed PLZT films showing the twin-platelets (a) at lower magnification and (b) secondary (right) and backscattered electron images (left) at higher magnification. 106
Figure 4.24 Microstructure of PLZT film on sapphire after annealing at 700°C, 5 h. 107
Figure 4.25 Micrograph of PLZT (9/65/35) film on sapphire after furnace annealing, with significant Pb-deficiency. The rounder features of platelets are observed. 107

Chapter V

Figure 5.1 An interdigitated electrode (IDE) structure that was patterned onto a mask for photolithography steps. 113
Figure 5.2 Dielectric constant and loss versus temperature for the as-deposited PLZT

film on sapphire. 116
Figure 5.3 The temperature dependence of dielectric constant and loss (top) and dc-bias response (bottom) of 0.5 μm-thick rapid thermally annealed PLZT film on sapphire. 117
Figure 5.4 Dielectric properties as a function of temperature (a) response with bias voltage (b), for a 0.75 μm-thick PLZT film (post-RTA). 118
Figure 5.5 Dielectric constant and loss as a function of temperature for 0.35 m-thick PLZT film after a two-step annealing. 119
Figure 5.6 Temperature dependence of dielectric constant and loss for a PLZT film on sapphire. The film was deposited below 300°C and then furnace annealed at 700°C, 3 h. 120
Figure 5.7 Dielectric constant and loss as a function of temperature for PLZT film (0.75 μm) deposited at low temperature and annealed at 750°C for 3 h. 120
Figure 5.8 Dielectric constant and loss tangent as a function of temperature for a PLZT film deposited at 490°C and annealed at 700°C for 20 min. 122
Figure 5.9 Temperature dependence of the dielectric constant and loss of a furnace annealed PLZT film on sapphire (a), and the effect of dc-bias voltage on the dielectric constant (b) and tangent loss (c) for the same film. 125
Figure 5.10 Influence of poling the PLZT film on the dielectric constant (top) and tangent loss (bottom). 126
Figure 5.11 Resistance vs voltage and I-V curves for an annealed Pb-deficient PLZT ....
film before and after poling. 127
Figure 5.12 The structure used to model the transmittance vs. wavelength of PLZT 9/65/35 film on sapphire. 130
Figure 5.13 The measured and simulated transmission curves for annealed PLZT 9/65/35 film on sapphire, with 0.44 μm thickness. 131
Figure 5.14 Refractive index and absorption coefficient versus wavelength for annealed PLZT 9/65/35 film on sapphire. 132
Figure 5.15 Three TE modes prism coupled into as-deposited PLZT 9/65/35 film on sapphire 134
Figure 5.16 Surface electrode (Cr/Au) patterns on a PLZT film on sapphire used for EO measurements 135
Figure 5.17 Calculated minimum needed film thickness vs. electric field to achieve a retardation of 0.5 degrees. 136
Figure 5.18 Experimental setup used for electrooptic measurements of PLZT thin films 137
Figure 5.19 Sample intensity pattern obtained with CCD camera. The transect line used for the intensity values is shown on top. 138
Figure 5.20 Intensity transect values. 138
Figure 5.21 Retardation changing as a function of time, as the voltage applied to a PLZT thin film modulator is varied in discrete steps. 139
Figure 5.22 Remarkably large electrooptic effect in a 0.6 μm-thick 9/65/35 film on

r-sapphire. The electrode gap was 10 μm. 140

Chapter VI

Figure 6.1 Phase diagram of $KTaO_3$-$KNbO_3$ [14]....147
Figure 6.2 Composition dependence of the lattice parameter of $KTa_{1-x}Nb_xO_3$ [11]. 149
Figure 6.3 Phase diagrams of system K_2O-Nb_2O_5 (a) and K_2O-Ta_2O_5 (b) [21,22]. 150
Figure 6.4 Dielectric constant as a function of temperature for $KTa_{1-x}Nb_xO_3$ crystals. Values for x are: 0.226 for 1, 0.249 for 2, 0.347 for 3, 0.391 for 4 and 0.425 for 5 [11]. 152
Figure 6.5 Transmission spectrum of KTN crystal [15]. 154
Table 6.1 KTN thin films deposited on different substrates. 160

Chapter VII

Figure 7.1 Experimental setup for sol-gel synthesis of KTN. 169
Table 7.1 KTN precursor and its hydrolysis with water. 172
Figure 7.2 DTA spectrum of sol-gel KTN powder. The heating rate:10°C/min, atm:air....174
Figure 7.3 X-ray diffraction of KTN (10/90) sol-gel powder annealed at 500°C in air. 175
Figure 7.4 X-ray diffraction pattern of KTN (64/36) sol-gel powder annealed at 600°C in air for 10 h, followed by an anneal at 800°C in O_2 for 2 h. All peaks belong to the perovskite phase. 176
Figure 7.5 X-ray diffraction of annealed KTN (64/36) sol-gel powder with 15% excess K. The (*) denotes the secondary phase, the indexed peaks representing the perovskite phase....176
Table 7.2 Lattice constants of sol-gel derived $KTa_{1-x}Nb_xO_3$ powders. 177
Figure 7.6 XRD pattern of sol-gel KTN thin film on r-sapphire after RTA. 179
Figure 7.7 RBS spectrum of spin-coated KTN thin film on silicon substrate. 180
Figure 7.8 RBS spectra of sputtered KTN films on GaAs (a) and sapphire (b) substrates. The film thicknesses are 1.45 μm (a) and 0.55 μm (b) respectively. 184
Figure 7.9 XRD patterns of sputtered KTN films on sapphire (top) and GaAs (bottom) substrates. 186
Figure 7.10 Dielectric constant vs. temperature curve for KTN film on GaAs substrate. 187
Figure 7.11 Dielectric constant as a function of temperature (top) and frequency (bottom) for a 2.9 μm-thick KTN film on sapphire. The solid lines are dielectric data and dotted lines are tan delta measurements. 188
Figure 7.12 Model structure for a large permittivity perovskite film (ε_2) in series with low permittivity capacitor layers....190
Figure 7.13 Reflectance of KTN films of various thickness on sapphire (top) and the refractive index vs wavelength curve for the films (bottom) obtained through simulation....191

Acknowledgments

I am indeed grateful for the vision and independence provided during my research, to my advisor Professor Sadik C. Esener. He promoted a creative atmosphere in our research group where everyone learns and discovers the best methodology to become an inventive, competent and problem-solver scientist and engineer.

Thanks to Dr. Sanat Sashital of TRW for the helpful discussions and providing impetus to KTN part of the study during the course of my PhD. I am also thankful for the opportunity to visit and perform experiments in the labs at TRW. I would like to thank Professor Joanna McKittrick for the valuable advice and discussions as well as providing access to her lab for my research. Thanks also to my committee members, Professors Marc A. Meyers, Massoud Simnad and Peter Asbeck for the valuable suggestions.

I owe appreciation to S. S. Lau who has been extremely helpful for the success of my research by allowing access to his laboratory and particularly the use of Rutherford Backscattering Spectrometer and Rapid Thermal Annealer. The assistance of his group members, Ban Zhu, Fei Deng and Mr. Guan is greatly appreciated. I would also extend my thanks to Professor H. L. Luo for providing access to his lab and the use of the tube furnace.

I am indebted and very thankful to my friend and colleague, Phil Harvey, for great many discussions and his invaluable help in completing the electrical and electrooptic characterization of films.

David Shih and Dr. S. Krishnakumar have taught me practical skills in device processing that aided me overcome many problems. Katsuyuki Hironaka of Sony, Japan, has provided extensive support in initializing the sol-gel experiments. Drs Chi Fan and Philippe Marchand have both aided me extensively in furthering my presentation skills. I also thank Dr. C. Fan for her critique of my research.

The access to Scripps Analytical Facilities and Electron Microscopy is appreciated. The sponsorship of governmental agencies in completing my studies during my PhD is gratefully acknowledged, initially, by Turkish Science and Research Agency for NATO fellowship for one year and later, remaining years by DARPA.

I also wish to thank all my friends and colleagues for many discussions: Daniel Van Blerkom, Dr. Barmak Mansoorian, Dr. Volkan Ozguz, Mike Jin, Dan Hartmann, Osman Kibar, Mark Hansen, Selim Guncer, Lee Hendrick, Scott Gardner, Dr. Ilkan Cokgor, Huseyin Sari, Mihrimah Ozkan, Matthias Blume, Susan Wey, Mark Wang, Dr. Nicolas Mauduit, Dr. Walter Daschner, Dr. Jerry LaSalvia and Jim Thomas.

Lastly on a personal level, I owe thanks to my parents, my brother Serdar and my sister Ülkü for their love and support throughout my graduate studies.

Vita

Jan. 8, 1967	**Born, Izmir, Turkey**
1988	**B.S., Metallurgical Eng., Middle East Technical University, Ankara, Turkey**
1988-89	**Engineer, Turkish Standards Institute, Ankara, Turkey**
1989-91	**M.S., Ceramic Engineering, Alfred University, Alfred, New York** NATO Science Fellowship (89-91)
1991-97	**Ph.D., Materials Science, University of California, San Diego, La Jolla, California** NATO Science Fellowship (91-92) Research Assistant (92-97)

Publications

1. B. Tunaboylu, P. C. Harvey, F. Deng, C. Fan and S. C. Esener, "Ferroelectric PLZT thin films deposited by RF triode magnetron sputtering for spatial light modulators", *IEEE International Symposium on the Applications of Ferroelectrics*, New Jersey, Aug. 18, 1996 (in press).

2. B. Tunaboylu, P.C. Harvey, C. Fan, S. Esener, "Growth and characterization of epitaxial lead lanthanum zirconate titanate thin films on sapphire", *Proceedings of III. International Ceramic Congress*, Istanbul, vol. 2, pp. 330-339 (1996).

3. B. Tunaboylu, C. Fan and S. Esener, "Synthesis of sol-gel $KTa_{1-x}Nb_xO_3$ for bulk ceramics and thin films", *Proc. of III. Int. Ceramic Congress*, Istanbul, vol. 2, pp. 349-356 (1996).

4. B. Tunaboylu, J. R. Varner, and H. Mandal, "Effect of Al_2O_3 and Y_2O_3 additions on the sintering behavior, microhardness and fracture toughness of silicon nitride", *Proc. of III. Int. Ceramic Congress*, Istanbul, vol. 2, pp. 221-227 (1996)

5. B.Tunaboylu and J. R. Varner, "Sintering and characterization of Si_3N_4 containing La_2O_3-SrO as an additive", *J. of Materials Science Letters*, 14, p 1246 (1995).

6. B. Tunaboylu, J. McKittrick, W. J. Nellis, and S. R. Nutt, "Dynamic compaction of Al_2O_3-ZrO_2 compositions", *J. of American Ceramic Society*, 77, p 1605 (1994).

7. J. McKittrick, B. Tunaboylu, and J. Katz, "Microwave and conventional sintering of rapidly solidified Al_2O_3-ZrO_2 powders", *J. of Materials Science*, 29, p 2119 (1994).

8. J. McKittrick, B. Tunaboylu, and J. D. Katz, "Compaction of submicron and nanocystalline Al_2O_3-ZrO_2 ceramics", in *Mech. Prop. and Deformation Behavior of Materials Having Ultra-Fine Microstructures*, Kluwer Publ., p 559 (1993).

9. J. McKittrick, B. Tunaboylu, and J. D. Katz and W. Nellis, "Al_2O_3-ZrO_2 ceramics with submicron microstructures obtained through microwave sintering, plasma sintering and shock compaction", *Materials Research Society Symp. Proc.*, vol. 274, p 149 (1992).

10. B. Tunaboylu, J. McKittrick, and J. D. Katz, "Microwave and plasma sintering of alumina-zirconia ceramics", presented at *American Ceramic Society annual meeting*, Minnesota, (1992).

11. B. Tunaboylu, P. Harvey and S. C. Esener, "Microstructure of magnetron sputtered PLZT thin films on r-sapphire," submitted to *Integrated Ferroelectrics*.

12. B. Tunaboylu, P. Harvey and S. C. Esener, "Characterization of dielectric and electrooptic properties of magnetron sputtered PLZT 9/65/35 films on sapphire for electrooptic applications," submitted to *IEEE Transactions on Ultrasonics, Ferroelectrics, and Frequency Control.*

13. B. Tunaboylu, P. Harvey, S. C. Esener and S. R. Sashital, "Synthesis and deposition of KTN films by sol-gel and magnetron sputtering," submitted to *Ferroelectrics Letters.*

14. B. Tunaboylu, J. McKittrick and S. C. Esener, "Phase transformation kinetics in $Pb_{0.91}La_{0.09}Zr_{0.65}Ti_{0.35}O_3$ films," submitted to *J. Mater. Sci. Lett.*

Abstract of the Dissertation

Synthesis, Deposition and Characterization of Ferroelectric Films
for Electrooptic Devices

by

Bahadir Tunaboylu

Doctor of Philosophy in Materials Science
University of California, San Diego, 1997

Professor Sadik Esener, Chair

The use of integrable ferroelectric electro-optic thin films is a revolutionary approach in the development of high-speed, low-voltage and high-contrast ratio integrated electro-optic spatial light modulators (SLM) for free-space optoelectronic interconnects. Thin films offer improved performance over bulk ferroelectric (FE) materials because of their lower modulator capacitance and operation at high speeds with low switching energies. Integration of ferroelectric thin films with silicon technology will also impact both the uncooled infrared sensor and dynamic and nonvolatile memory technologies. Ferroelectrics such as lead lanthanum zirconate titanate (PLZT) and potassium tantalate niobate (KTN) present great potential for SLMs due to their large electro-optic (EO) effect in the bulk form. The development of thin-film SLMs require electro-optic films of high optical quality with good dielectric and EO properties.

High quality thin films of PLZT and KTN were deposited using RF magnetron sputtering on r-plane sapphire substrates which offer integration capability with semiconductor devices. PLZT films with extremely large peak dielectric constant, 2800 at the Curie temperature of 180°C, were achieved with remarkably low dissipation loss factor < 0.04. The dielectric frequency dispersion was determined to be very small up to 1 Mhz. Also, the absorption of the light in the films was very low. A giant effective quadratic electrooptic effect was demonstrated in PLZT films. These results represent a huge leap forward for the FE-SLM technology with respect to the goal of fully integrated thin film electrooptic light modulators.

Microstructural development and phase transformation kinetics in PLZT films were also analyzed for the first time and are presented here. Energy required for the formation of desirable perovskite phase was determined to be 322 kJ/mol. Single-phase PLZT films with larger average grain size showed higher dielectric constants and better EO properties as compared to films with smaller grain size. Furthermore, a method of sol-gel synthesis of KTN with reproducible characteristics was developed for fabrication of both thin films and homogeneous sputtering targets. Also for the first time, a stoichiometric KTN target was consolidated to high density by hot-isostatic pressing developed during this study.

1. Introduction

1.1 Spatial light modulators for optoelectronic computing

The trend toward increasingly massive parallel processing architectures together with the high processing speeds (clock rates ≥ 1-10 Ghz) required for future generations of supercomputers, necessitates development of ultra-fast and ultra-dense signal processing devices. Advances in various semiconductor devices and the evolution of conventional semiconductor technology have improved 'on-chip' data processing speeds dramatically. However, it is realized that some fundamental drawbacks of conventional interconnect device technology severely limit the speed and performance of interchip signal communication rates. The bottleneck is a direct consequence of the technological limitations of electrical interconnections in terms of 'area' because of the planar nature of electronic technology where electrons interact causing crosstalk, and in terms of delay and power dissipation' because of the resistive and capacitive nature of electrical interconnects.

It is now widely recognized that the performance of parallel digital electronic computers can be greatly enhanced in terms of bandwidth versus system power and volume, if free-space optical interconnections are implemented at the interchip level since they can provide highly dense global and fast interconnections in the third dimension [1]. A generic free-space optical interconnection system with its basic components is shown in Figure 1-1. The system light power is provided by an external laser source.

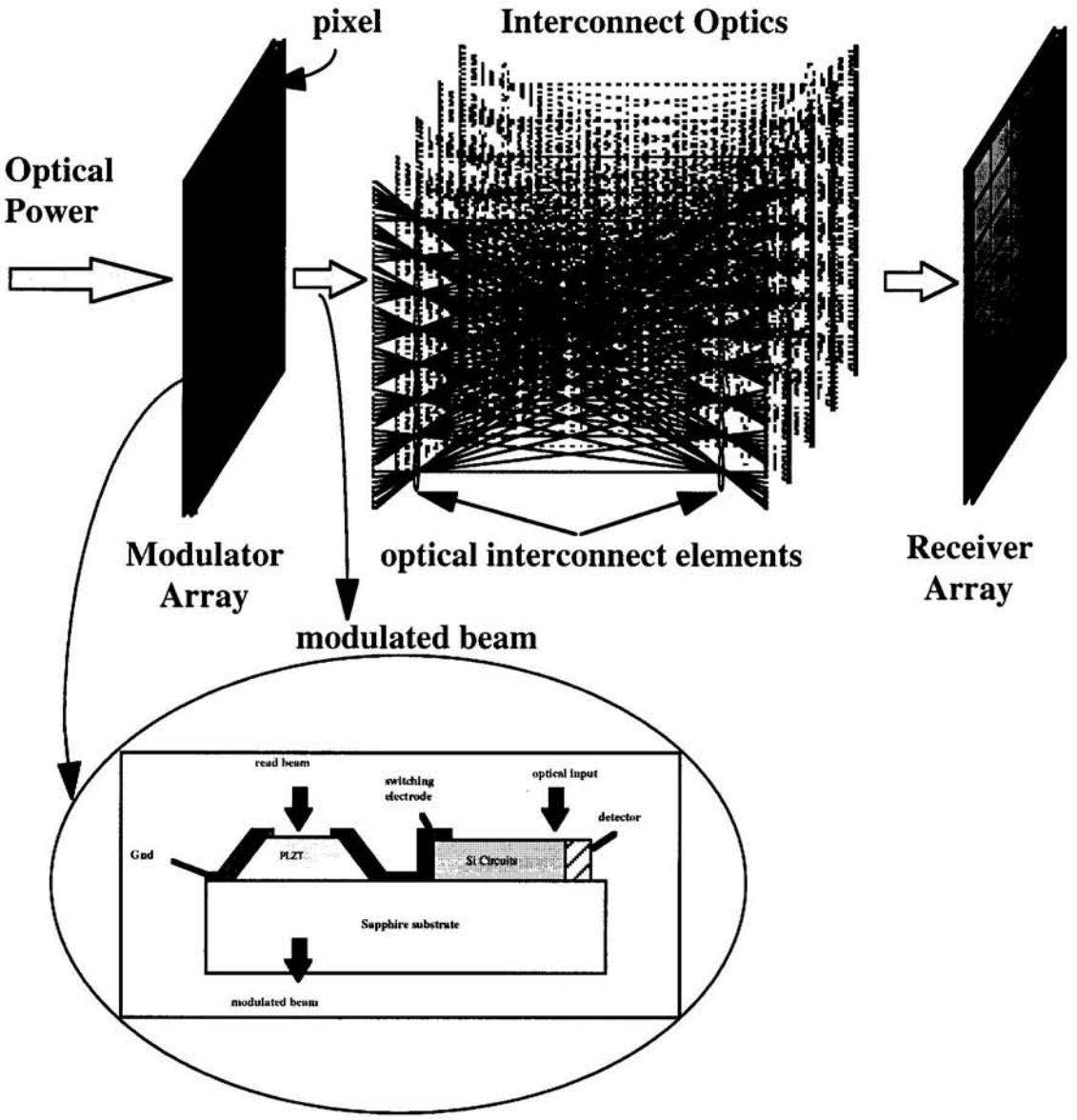


Figure 1-1 A generic free-space optical interconnection system.

The basic element of an optoelectronic computing system is an electronic integrated circuit (IC) with optical receivers for inputs and transmitters for outputs, referred to as a smart pixel. Smart pixel arrays are interconnected through free-space using optical components such as diffractive computer generated holograms and refractive optical components. An essential element of a smart pixel is the optical output transmitter (light modulator). Incoming optical data is sensed by light detectors, which convert the data into electronic form that is then fed to an electronic circuit for processing. At the output of the processing element, the processed data is converted back into optical form via light transmitters (sources or spatial light modulators), and is then routed to another processing element with free-space optical interconnections.

A Spatial Light Modulator (SLM) is defined as a device capable of modulating the characteristics of an optical field [2]. SLMs consist of two major blocks: i) the control section which is electrical or optical, ii) the readout section. The readout section must be made of a material capable of changing some properties of an incoming beam (i.e. amplitude, phase or polarization) with the information provided from the control section. Therefore, materials are needed where strong non-linear interaction of the control signal with the field of the incoming light beam occurs.

Various transmitters including light sources and modulators such as multiple quantum well (MQW) absorption modulators as well as inorganic ferroelectric (FE) electrooptic (EO) phase modulators have been proposed. These devices with complementary characteristics are potentially useful for smart pixels. Ferroelectric Liquid Crystal (FLC)

modulators can only switch at about a microsecond at best [3], which severely limits their span of applications to slower displays. Electrooptic light modulators (inorganic EOLMs) are especially important for highly dense interconnections due to their lower on-chip power dissipation and can provide large fan-out due to their non-absorptive nature. In terms of neural network applications an important limitation of MQW modulators is due to their absorptive nature; on-chip power dissipation increases with fan-out. The fan-out is defined as the number of receivers which receive a signal from a given modulator (or transmitter). In spite of major progress made toward their integration with logic circuits/detectors, smart pixels still suffer from lack of uniformly integrable, low voltage (<10V operation) and high speed (1 to 10 Ghz) EOLMs with good contrast ratio (>20:1).

The system/device requirements can be translated to material requirements for spatial light modulators. Ferroelectric oxide materials such as lead lanthanum zirconate titanate (PLZT) and potassium tantalate niobate (KTN) have unique advantage of satisfying almost all the system requirements when they are integrated into silicon technology and especially in the thin-film form due to reduced voltage requirement. These materials exhibit large electrooptic effects requiring relatively small modulation voltage. In the bulk form, however, these FE oxides require high switching energies for modulation. It is possible to reduce drive voltages to 5 - 10 V when thin films are used. A comparison of some of the leading FE candidate materials in the bulk (crystal or ceramic) form is given in Table 1-1, in terms of their dielectric constant (ε_r), electric-field induced birefringence (Δn) for a field E of 2 V/μm and EO figure of merit (defined as the amount of birefringence

divided by the switching energy, $\Delta n/\varepsilon_r E^2$) related to birefringence and switching energy. A large field-induced birefringence (Δn) is the most important parameter and needed for large EO modulation with a small electric field. Thus, a large figure of merit is desired. Birefringence is the difference in the refractive indices along otrhogonal axes (a and c-axis) of a crystal. The birefringence in the table is the amount of phase retardation induced by an applied electric field and n_i, r_{ij} and s_{ij} represent refractive indices, linear and quadratic electrooptic coefficients, respectively. As it can be seen from the Table 1-1, KTN ($KTa_{0.65}Nb_{0.35}O_3$) crystals top the list in terms of higher field-induced birefringence and the figure of merit than those of PLZT (designated 9/65/35, composition is 9 atom %La with a 65:35 ratio of Zr to Ti), SBN (strontium barium niobate $Sr_{0.75}Ba_{0.25}Nb_2O_6$, T_c = 56°C) or $LiNbO_3$ (T_c = 1230°C). On the other hand, PLZT has a high Curie temperature (T_c = 74°C) making it relatively insensitive to temperature variations and is also commercially available in high quality wafers. The Curie transition (T_c = 40°C for tetragonal KTN) of cubic KTN (T_c = 10°C) is very sharp, has been difficult to grow large crystals in optical quality. SBN, though, is the most intractable in terms of crystal growth since its high EO composition lies at a morphotropic phase boundary, making it almost impractical for applications. Therefore, KTN and PLZT are the most likely candidates for optical phase modulation.

Thin film modulators are attractive because of lower device capacitance due to reduced thickness (1 μm) that would require smaller drive voltages. Thin films, however, give smaller amount of light modulation due to reduced interaction lengths. By placing the

FE film in a Fabry-Perot interferometer, the amount of light modulation can be dramatically improved. Also, the optical thickness uniformity of the deposited materials can be compensated in a Fabry-Perot modulator array using a self-tuned Fabry-Perot structure with a input holographic mirror [4]. Therefore, it is possible to bring low-voltage high-speed FE thin film SLMs into realization by growing high quality FE films on silicon-compatible substrates for high performance desired. This thesis focuses on growing such PLZT and KTN thin films on r-plane sapphire for EO devices, and with a better understanding of their thin film properties and their relationships, potentially other applications, pyroelectric sensing and microwave devices will result. The ability to use ferroelectric materials in smart pixels successfully will depend on large extent to our understanding of these materials.

Table 1-1 Comparison of leading electrooptic modulator materials. Assuming E=2V/μm.

	PLZT (cubic) $Pb_{.91}La_{.09}Zr_{.65}Ti_{.35}O_3$	$LiNbO_3$ (trigonal)	SBN (tetragonal) $Sr_{.75}Ba_{.25}Nb_2O_6$	KTN (001) (tetragonal) $KTa_{.35}Nb_{.65}O_3$	KTN (cubic) $KTa_{.65}Nb_{.35}O_3$
Birefringence	$\Delta n = \frac{n^3 R E^2}{2}$	$\Delta n = \frac{1}{2}(n_e^3 r_{33} - n_o^3 r_{13})E$	$\Delta n = \frac{1}{2}(n_e^3 r_{33} - n_o^3 r_{13})E$	$\Delta n = \frac{n^3 r_{51}^2 E^2}{2\left(\frac{1}{n_o^2} - \frac{1}{n_e^2}\right)}$	$\Delta n = \frac{n^3 (s_{11} - s_{12}) E^2}{2}$
Refractive Indices	n=2.5	n_e=2.20, n_o=2.29	n_e=2.34, n_o=2.35	n_e=2.281, n_o=2.318	n_o=2.29
EO Coefficients	$R=3.6\times10^{-16}$ $(m/V)^2$	$r_{51}=32.6\times10^{-12}$ (m/V)	$r_{33}-r_{13}=13\times10^{-10}$ (m/V)	$r_{51}=3000\times10^{-12}$ (m/V)	$s_{11}-s_{12}=17\times10^{-16}$ $(m/V)^2$
Field induced Birefringence	1.1×10^{-2}	2.5×10^{-4}	1.5×10^{-2}	3.7×10^{-2}	3.95×10^{-2}
Dielectric Constant (ε_r)	4500	98	3000	2000	2000
Figure of Merit $\left[\frac{\Delta n}{\varepsilon_r E^2}\right]$	6.11×10^{-19}	6.37×10^{-19}	1.25×10^{-18}	4.63×10^{-18}	4.94×10^{-18}

The next section analyzes the ferroelectrics in general and lays the foundation for relating to their dielectric and electrooptic properties. The last section describes the current integration technologies of light modulators and illustrates the thin-film structure and its integration aimed in this study.

1.2 Ferroelectric materials for SLMs

1.2.1 Ferroelectrics

A ferroelectric crystal exhibits an electric dipole moment even in the absence of an external electric field. In the ferroelectric state the center of positive charge of the crystal does not coincide with the center of negative charge. Ferroelectricity is defined as the spontaneous alignment of electric dipoles by their mutual interaction. A plot of polarization versus electric field for the ferroelectric state shows a hysteresis loop.

There are ten non-centrosymmetric crystal classes which possess a unique polar axis, i.e. an axis which shows properties at one end different from those at the other. Crystals in these classes are called 'polar' because they are spontaneously polarized [5]. If the temperature of the crystal is altered a change in the polarization occurs and electric charges can observed on those crystal faces which are perpendicular to the polar axis. This is called pyroelectric effect and the pyroelectric coefficient is usually given by dP/dT in $\mu C\ cm^{-2}K^{-1}$. Ferroelectric crystals belong to the pyroelectric family. However, it is necessary also for a ferroelectric crystal to show reversibility of the polarity. Therefore a ferroelectric crystal can be defined as a pyroelectric crystal with reversible polarization.

The source of ferroelectricity arises from the fact that the local field E′ increases in proportion to the polarization. The polarization P is defined as the dipole moment per unit volume, averaged over the volume of a cell. For a material containing electric dipoles increased polarization increases the local field. The dielectric constant ε of an isotropic medium relative to vacuum is defined in terms of the macroscopic field E [6]:

$$\varepsilon = \frac{\varepsilon_0 E + P}{\varepsilon_0 E} = 1 + \chi \qquad (1\text{-}1)$$

where ε_o is the dielectric constant of free space, 8.854×10^{-12} F/m, and χ is the susceptibility.

In a noncubic crystal the dielectric response is described by the components of the susceptibility tensor or of the dielectric constant tensor. The polarizability α_i of an atom is defined by in terms of the local electric field at the atom: $p = \alpha_i E'$, where p is the dipole moment. The polarizability is an atomic property, but the dielectric constant will depend on the manner in which the atoms are assembled to form a crystal. For a non-spherical atom α_i will be a tensor [6]. The polarization of a crystal may be expressed approximately as the product of the polarizibilities of the atoms times the local electric field [6]:

$$P = \sum_j N_j p_j = \sum_j N_j \alpha_j E'(j) \qquad (1\text{-}2)$$

where N_j is the concentration and α_j the polarizability of atoms j and E′ (j) is the local field at the atom sites j.

There are four possible mechanisms for polarization in dielectrics. One process common to all materials is electronic polarization, or the shift of the center of gravity of the negative electron cloud in relation to the positive atom nucleus in an electric field. A second mechanism is the displacement of positive and negative ions in relation to one another, called ionic polarization. A third kind of polarization, uncommon in ceramics, is associated with the presence of permanent electric dipoles which exist even in the absence of electric field and line up with applied electric field. This is called either orientation or dipolar polarization. A final source of polarization is mobile charges which are present at structural interfaces as space charges results in an increase in capacitance.

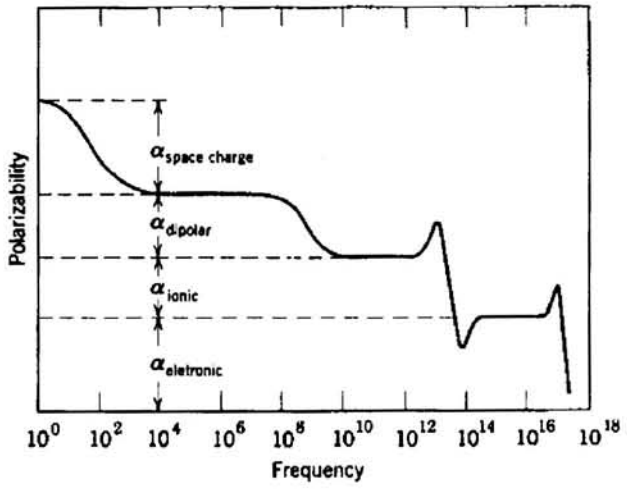


Figure 1-2 Frequency dependence of several contributions to the polarizability [7].

The total polarizibility from these four mechanisms can be expressed as [7] :

$$\alpha_T = \alpha_e + \alpha_I + \alpha_d + \alpha_s \qquad (1\text{-}3)$$

where α_e is the electronic, α_I is the ionic, α_d is the dipolar or orientation and α_s the space charge polarizability.

In an ideal capacitor the electric charge adjusts itself instantaneously to any change in voltage. In practice, however, there is relaxation time for charge transport. We then observe in fact a dependence of the dielectric constant on frequency (see Figure 1-2 [7]). The electronic polarization is the only process that can follow closely an alternating field on the order of 10^{15} Hz and in the visible part of the spectrum, the equation $\varepsilon = n^2$ is valid, n: refractive index). Ionic processes are able to follow an applied high-frequency field and contribute to the dielectric constant at frequencies up to the infrared region of the spectrum. The relaxation time (or time lag of the system) argument leads to a secondary term in a real dielectric, a loss factor, related to imaginary part of the dielectric constant, ε''. The time required for polarization, or the loss factor (tan delta), shows up as a phase retardation of the charging current (I_c) for an ac-field. Instead of being 90° advanced, I_c is advanced by some 90 - δ, where the loss angle is δ [7]. The loss factor is the primary criterion for the usefulness of a dielectric as an insulator material. For example, the loss values above 0.1 (tan delta 0.1) is not acceptable for microwave devices. For EO devices, low tangent losses in the order of 0.01 are desirable. For a commercial soda-lime-silica glass with dielectric constant of 9 for a frequency of 1 kHz, tan delta is less than 0.001 [7]. The tan delta of nickel-zinc-ferrite ($Ni_{0.4}Zn_{0.6}Fe_2O_4$) is about 3 at 1 kHz [7]. For ferroelectric ceramics, tan delta values are usually below 1 and higher values

are common to polymers. Polymers such as ploy(methyl methacryalte) (PMMA) have dielectric losses in the range of 3.6 to 4.7 at 1 Mhz [8].

One of the main advantages of ceramics as dielectrics is that this loss factor (tangent loss) is small compared with that of other available materials such as polymers. Energy losses in dielectrics result from three primary processes [7]:

1. Ion migration losses; (a) dc conductivity, (b) ion jump and dipole relaxation losses
2. Ion vibration and deformation losses
3. Electron polarization losses

The major factor affecting the use of ceramic materials is the ion migration losses which tend to increase at low frequencies and as the temperature is raised. The loss factor ($\tan \delta = \varepsilon''/\varepsilon'$) can be written in terms of the electrical conductivity as $\omega\varepsilon'' = \sigma = \omega\varepsilon'\tan \delta$ where σ is the conductivity, ω is the frequency, ε'' is the imaginary part of the dielectric constant and ε' is the real part of the dielectric constant.

In ferroelectric crystals in their polar state, there are domains which have unique polarization axes. When an electric field is applied, the polarization axis of the domain can switch to the preferred direction, lower energy states usually in parallel to the direction of applied field. However those domains which are already in the preferred direction can enlarge their size by consuming others and thus the overall polarization can be increased or even its direction reversed. The result of spontaneous polarization in ferroelectrics at some critical temperature is the appearance of very high dielectric constants together with a hysteresis loop for polarization in an alternating field.

A typical ferroelectric hysteresis loop is seen in Figure 1-3 (P_s : spontaneous polarization, P_r : remanent polarization, E_c : coercive electric field, α : the angle defined by the initial slope of polarization versus electric field curve) [7], which result mainly from the alignment of dipoles in different domains. For example, in tetragonal phase of KTN, one axis of the original cubic unit cell elongates as the tetragonal c-axis (polar axis), giving rise to the existence of 90° and 180° domains in the crystal [9]. A similar domain and domain-wall behavior is also observed in $BaTiO_3$. The reduction of dielectric constant over prolonged time that has been seen due to domain activity or polarization relaxation is usually termed as aging in ferroelectrics. This is not typically observed in its paraelectric state. The paraelectric term is used to refer to the state of a crystal above its Curie temperature as the non-polar state.

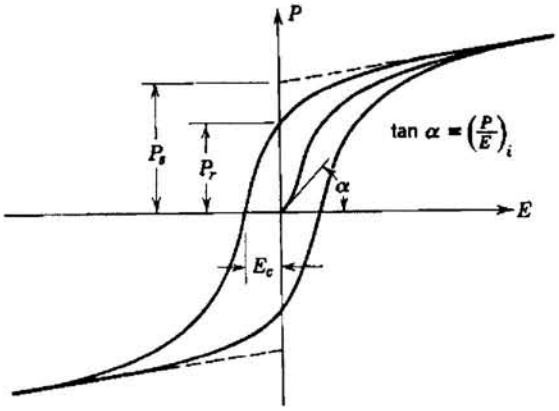


Figure 1-3 A typical ferroelectric hysteresis loop [7].

Ferroelectrics usually lose their spontaneous polarization at high temperature by randomizing their dipole moments because of increasing thermal energy. The abrupt

transition from ferroelectric to paraelectric takes place at a temperature called Curie temperature (T_c). Above the T_c, the FE becomes non-polar. The linear dependence of the inverse susceptibility on T - T_c is known as the Curie-Weiss law [5], expressed as (T : temperature):

$$\varepsilon = \chi + 1 \qquad \text{and} \qquad \chi = \varepsilon - 1 = \frac{3T_c}{T - T_c} \tag{1-5}$$

One of the consequences of orientability of the polar axis of ferroelectrics is that the polar axis, thus the optical axis can be induced in the naturally non-polar cubic state in ferroelectrics like PLZT and KTN. However, the polar axis is fixed in the tetragonal or orthorombic crystals or ceramics. Electrooptic ceramics show effects consistent with their crystal counterparts, usually though an averaging effect of overall grains/domains is reflected. The advantage of ceramic PLZT or KTN in paraelectric state is that polar axes can be defined by the electric field, also their hysteresis is fairly small. For fast switching light modulator applications, slim-loop ferroelectrics are better suited because the large hysteresis can slow the response of the modulator at high frequencies and behave in a non-linear fashion.

The ferroelectric ceramics show dielectric and ferroelectric behavior which are dependent on processing methods. The thin films of ferroelectrics are even more sensitive to deposition/processing conditions. The microstructure, grain size, residual stresses, remaining porosity all have influence on the electrical properties. The effects of such parameters were discussed for bulk and thin film PLZT in detail in the next two chapters.

Usually dielectric constant was lowered by the presence of porosity and secondary phases in bulk ceramics [7]. Grain sizes from 2 to 3 μm increased the electrooptic effect and the effect saturated for larger grain sizes in the bulk PLZT composition designated 8/65/35 (composition is 8 atom %La with a 65:35 ratio of Zr to Ti) [10]. Okazaki and Nagata [11] have observed an increase in T_c with decreasing grain size accompanying decreased dielectric constants in hot-pressed PLZT ceramics. For the thin films though, the effect of such parameters are not well known in PLZT or KTN.

1.2.2 Electrooptic effect

Most ferroelectrics are transparent in the visible to the near infrared radiation range. One of their most important characteristic is that the refractive indices of some ferroelectrics can be modulated by an electric field significantly. Ceramics like PLZT show various types of electrooptic effects which use its linear birefringence, quadratic birefringence, memory birefringence as well as a photorefractive effect. The change in birefringence of a crystal by an electric field is commonly referred as the electrooptic effect.

The propagation of optical radiation in a crystal can be described completely in terms of the impermeability tensor $\Delta\eta_{ij} = \Delta(\varepsilon_o\varepsilon^{-1})_{ij}$. According to quantum theory of solids, the optical impermeability tensor depends on the distribution of charges in the crystal. The application of an electric field will give rise to a redistribution of the bond charges and also shifting the electron clouds around positively-charged ion at the center of an oxygen

octahedron inducing a slight deformation of the ion lattice. The net result is a change in the optical impermeability tensor. This is known the electrooptic effect and the electro-optic coefficients are conventionally defined as [12]

$$\eta_{ij}(E) - \eta_{ij}(0) \equiv \Delta\eta_{ij} = r_{ijk} E_k + s_{ijkl} E_k E_l$$

$$\Delta\eta_{ij} = f_{ijk} P_k + g_{ijkl} P_k P_l \qquad (1\text{-}5)$$

where **E** is the applied electric field, **P** is the polarization field vector and η_{ij} is the optical impermeability tensor. The constants r_{ijk} and f_{ijk} are the linear (r) (or Pockels) electro-optic (EO) coefficients, and s_{ijkl} and g_{ijkl} are the quadratic (s or R) (or Kerr) EO coefficients. The terms higher than quadratic are usually ignored since they are very small. The index ellipsoid of a crystal in the presence of an applied electric field can be represented by $\eta_{ij}(\mathbf{E})x_i x_j = 1$. The directional behavior of the refractive index of a material is most generally described by the index ellipsoid.

$$\frac{x^2}{n_x^2} + \frac{y^2}{n_y^2} + \frac{z^2}{n_z^2} = 1 \qquad (1\text{-}6)$$

where x, y, z are the dielectric axes, the directions in the crystal along which the displacement vector D is parallel to electric field vector E and n_x, n_y and n_z are the principal indices of refraction. The permutation symmetry reduces the number of independent elements of r_{ijk} from 27 to 18 and the number of elements of fourth rank tensor s_{ijkl} from 81 to 36 [12].

For a given crystal orientation, the linear (r) and quadratic (R) EO coefficients can be determined from the dependence of birefringence (Δn) on the applied electric field (E) through the relationships

$$r = -\frac{2\Delta n}{n^3 E} \text{ and } R = -\frac{2\Delta n}{n^3 E^2} \tag{1-7}$$

Both the Pockels and Kerr effects can be utilized for electrooptic light modulation. The birefringence induced by an electric field can be measured as an optical phase retardation in an electrooptic ceramic like PLZT or KTN, as described in Figure 1-4 [13]. Linearly polarized monochromatic light, on entering the electrically energized ceramic, is separated into two perpendicular components x_1 and x_2 whose vibration directions are defined by the crystallographic axes of the crystallites acting as one single entity with a polar axis aligned along the direction of the electric field. Because of the different refractive indices n_e and n_o, the two components of different wavelengths will propagate through the material at different velocities, resulting in a phase shift, but these waves will not mutually interfere with each other (PLZT in this case). When added together, the two components result in a wave with a polarization rotated with respect to the original wave. The total phase retardation, Γ, (phase shift) is a function of both Δn and the optical path length t according to the relationship, $\Gamma = \Delta n\, t$, where t is the thickness of the plate.

A complete treatment of electrooptic effect in cubic PLZT 9/65/35 and tetragonal and cubic KTN are presented in the following chapters, chapter 2 and chapter 6, respectively. Strontium barium niobate (SBN) also shows high linear EO effect in its tetragonal phase

but the fabrication of the composition which shows high r coefficient lie at a morphotropic phase boundary has been extremely difficult in the single phase with optical quality.

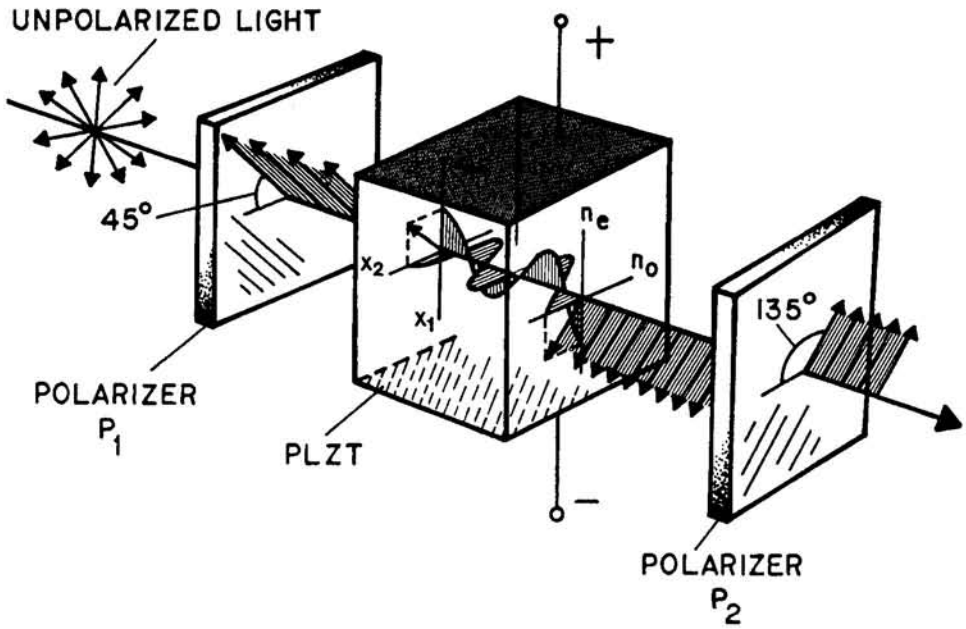


Figure 1-4 Optical phase retardation in an activated PLZT electrooptic ceramic [13].

Other electrooptic materials like polymers and ferroelectric liquid crystals can also be used as modulators. These materials are suited well for display applications. However, their EO coefficients are smaller than that of PLZT or KTN and also their switching speeds are much slower, giving responses in the order of 100 μs [3,14]. Polymers also require poling to retain high electrooptic effect, and is prone to fatigue after long operation cycles and sensitive to environment. Therefore, inorganic ferroelectric oxides like PLZT

and KTN are prime candidates for light modulating applications especially where large fan-out is desirable.

PLZT and KTN would be viable candidates for spatial light modulators if they can be integrated with silicon technology because the properties of the light modulating material incorporated with the very large scale integrated (VLSI) devices, determine the usefulness and practicability of the resulting SLM technology. The next section will discuss the state-of-the-art in integration of these materials with silicon drivers and detectors.

1.3 Integration technologies for Si/Ferroelectric SLM

There are two main approaches in integrating ferroelectric materials with electronic substrates with logic, driver elements; hybrid and monolithic techniques. The modulator drive voltage, modulator capacitance (also parasitic bond capacitance) are high in the hybrid approach compared to monolithic approaches. The hybrid integration of FE with silicon is a straight approach, usually termed as flip-chip bonding, used in silicon packaging technology (Figure 1-5) [15]. The modulators fabricated on the ferroelectric and bonded by indium contact bumps to the silicon wafer with electronic circuits, logic and detectors. The reflectivity of incoming light onto PLZT is varied by a multiple dielectric layer structure placed at the bottom of the wafer. The flip-chip technique is well developed and can be used to increase the smart pixel yield by preselecting working chips. However, the operation is costly for large arrays.

The scalability of SLMs can be improved with monolithic integration techniques. The monolithic integration of two different materials usually involves thin films. Hence, the approach involves the deposition and subsequent recrystallization of a polysilicon film on a PLZT (or alternatively KTN) substrate. Electronic circuits are then fabricated in recrystallized silicon [16]. However, the processing power of the SLMs fabricated using laser recrystallization of silicon is limited, ultimately, by the quality of the silicon film after recrystallization. Poor transistor yield results from high leakage currents, low mobility and large variations in threshold voltage caused by defects in laser recrystallized films. These defects at the boundaries of silicon are the result of high energy radiation damage induced by the laser. The number of transistors in a processing element will be restricted, imposing constraints on the size and complexity of the processing element.

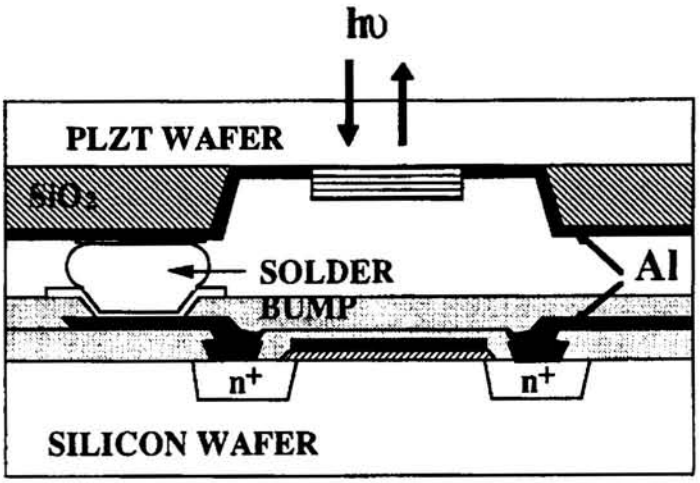


Figure 1-5 Hybrid bulk ferroelectric Si/PLZT SLM [15].

An alternate monolithic approach to produce PEs with more processing power, is to begin with a silicon on sapphire (SOS) substrate and deposit ferroelectric thin film PLZT or KTN on windows opened on the SOS wafer. By implementing silicon devices on the substrate prior to the deposition of ferroelectric films, complementary metal oxide semiconductor (CMOS) VLSI circuits of any complexity can be achieved and linked to FE light modulators on the same substrate. This feature is unique to integration techniques using thin film deposition. Furthermore, the use of transparent sapphire substrate allows transmissive or double-sided reflective SLMs. Without a transparent substrate, this flexibility cannot be realized.

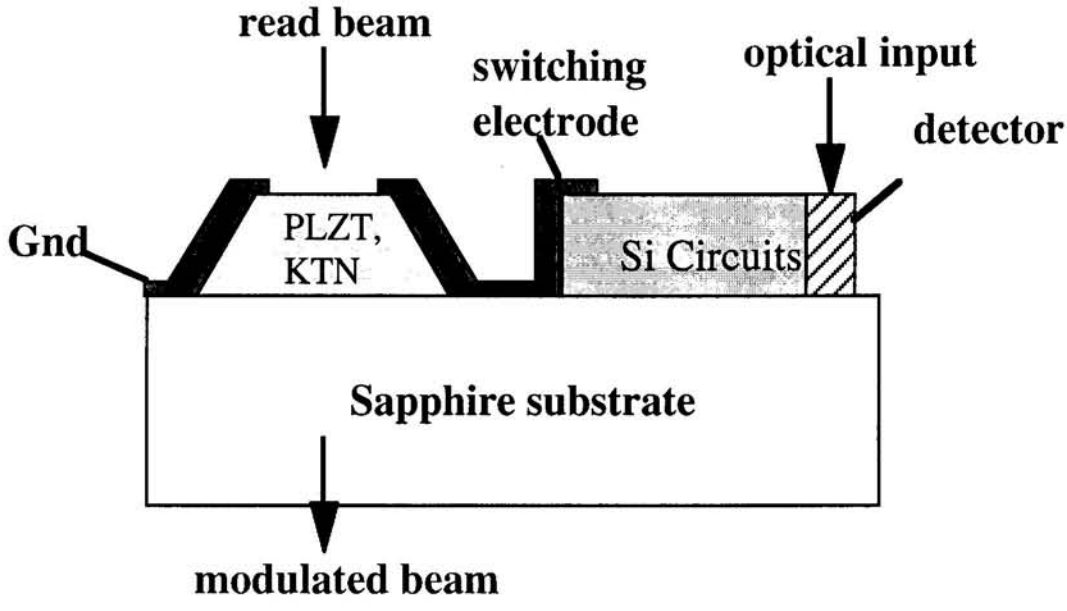


Figure 1-6 Cross section of ferroelectric thin film SLM on sapphire.

Figure 1-6 shows the cross-section of the silicon/ferroelectric thin film SLM structure. The critical step towards the development of such a device is, therefore, the growth of ferroelectric films of right composition and crystallinity on the appropriate substrate. The r-plane $(1\bar{1}02)$ sapphire was chosen as the substrate to provide compatibility with SOS technology.

R-sapphire is a good thermal conductor (3.5 Watts/m-K, which is twice that of MgO) and is less brittle than other potentially compatible substrates like silicon, GaAs etc. Silicon on sapphire (SOS) IC technology provides for smaller junction capacitance and is radiation hard. It has a hexagonal lattice with lattice parameters a = 0.4759 nm and c = 1.2991 nm, is often described as having O^{2-} anions in an approximately hcp arrangement with Al^{3+} cations occupying two-thirds of the octahedral interstices [17]. The empty sites of the cation sublattice are used to define the corners of the unit cell [17].

Epitaxial relations were found to be (111) PLZT on (0001) sapphire and [110] on [1010] sapphire despite the large lattice mismatch (> 5%) reported [18]. This is not surprising since it was reported that the epitaxy was observed for ion plated $LiNbO_3$ (012) on r-sapphire despite the 8.2% lattice mismatch [19]. The lattice mismatch of PLZT 9/65/35 with r-sapphire is about 6%, but is observed to result in (110) orientation. The lattice mismatch of (100) PLZT and (100) KTN are smaller on either $SrTiO_3$ (about 4.5%) or MgO (about 2.6%) and oriented growth is easier but they are not silicon-compatible substrates. Therefore, they are not viable candidates for substrates for

FE/SLMs. Platinized silicon and GaAs substrates were also used in this work because they offer the advantage of integration with IC technology.

The ferroelectric compositions chosen for SLM applications are also very important. First, they should show very high electrooptic effect, and second, the hysteresis behavior should be minimal since this would impair device performance by slowing down the operation speed. Therefore, compositions in the paraelectric state (T_c below room temperature) are best suited for such applications as they would show slim-loop hysteresis response and no birefringence when no voltage is applied. Fortunately, for both PLZT designated 9/65/35 (9 at% La with 65:35 ratio of Zr/Ti) and KTN (Ta/Nb: at% 65:35), the compositions with the quasi-cubic or cubic structures show the highest quadratic EO effect, as seen in Table 1-1 previously.

A shortcoming of the monolithic thin film approach is the shorter optical interaction lengths but this problem can be greatly alleviated increasing the optical path by multiple passes by using a novel self-tuned Fabry-Perot structure. Such a structure offers also compensation for thickness variations in thin films resulting from deposition process.

In this thesis, mainly PLZT 9/65/35 and KTN with Nb > 40% were studied. There is little data and information about thin films of PLZT 9/65/35 and KTN, the microstructural, electrical, optical and electrooptical properties and their interrelationships need to be understood for building future generations of Si/FE SLMs. In order to optimize the optical, electrical and electrooptic proeprties of the films for electrooptic devices, it is necessary to characterize the film's microstructural

characteristics and crystallinity with respect to specific deposition method and annealing conditions. The deposition/processing conditions affect the resulting properties, and with better understanding of the thin film behavior on r-sapphire, high quality FE films can be grown with good dielectric and electrooptic properties. Chapter 3 gives the overview of research done on PLZT thin films in the literature. Forthcoming chapters, 4, 5, and 7 deal with various aspects of deposition, annealing characteristics and compositional, microstructural, dielectric, optical and electrooptic evaluation of PLZT and KTN thin films mainly on r-sapphire substrate for future SLMs.

References

1 M. R. Feldman, S. C. Esener, C. C. Guest and S. H. Lee, "A comparison between optical and electrical interconnects based on power and speed considerations," *Appl. Opt.*, **27**, 1742, 1988.

2 S. Esener, "Silicon-based smart spatial light modulators: Technology and applications to parallel computers," SPIE Critical Reviews of Optical Science and Technology, CR35, p. 100, 1990.

3 T. J. Drabik, "Two-dimensional silicon/ferroelectric liquid crystal spatial light modulators," Mater. Res. Soc. Symp. Proc., vol. **392**, p. 111, 1995.

4 P. Harvey and S. Esener, "Thickness variation compensation in a Fabry-Perot modulator array using a self-tuned Fabry-Perot structure," *Appl. Phys. Lett.*, **70**, 1221, 1997.

5 F. Jona and G. Shirane, Ferroelectric Crystals, Dover Publications, NY, 1993.

6 C. Kittel, Introduction to Solid State Physics, sixth edition, John Wiley & Sons, 1986.

7 W. D. Kingery, H. K. Bowen and D. R. Uhlmann, Introduction to Ceramics, second edition, John Wiley &Sons, 1976.

8 L. A. Sullivan and H. S. Lackritz, "Dynamic mechanical analysis and dielectric relaxation for second order nonlinear optical applications," Mater. Res. Soc. Symp. Proc., vol. **392**, p. 69, 1995.

9 X. R. Huang, S. S. Jiang, X. Y. Xu, J. Y. Wang, Q. C. Guan, J. H. Jiang and D. Feng, "Ferroelectric domain structures and phase transitions in $KTa_{1-x}Nb_xO_3$ crystals," *Phys. Stat. Sol. (A)*, **148**, 611, 1995.

10 G. H. Haertling and C. E.Land, "Hot-pressed $(Pb,La)(Zr,Ti)O_3$ ferroelectric ceramics for electrooptic applications," *J. Amer. Ceram. Soc.*, **54**, 1, 1971.

11 K. Okazaki and K. Nagata, "Effects of grain size and porosity on electrical and optical properties of PLZT ceramics," *J. Amer. Ceram. Soc.*, **56**, 82, 1973.

12 A. Yariv and P. Yeh, Optical Waves in Crystals, John Wiley & Sons, 1984.

13 G. H. Haertling, "Electro-optic ceramics and devices," in Electronic Ceramics, edited by L. M. Levinson, Marcel Dekker, Inc., 1988, p. 371.

14 R. Lytel, "Fundamental performance limits of active polymer integrated optics," Mater. Res. Soc. Symp. Proc., vol. **392**, p. 65, 1995.

15 B. Mansoorian, V. Ozguz, C. Fan and S. Esener, "Design and implementation of flip-chip bonded Si/PLZT smart pixels," LEOS 1992 Summer Top. Meeting Dig. Smart Pixels, p. 22, 1992.

16 T. H. Lin, A. Ersen, J. H. Wang, S. Dasgupta, S. Esener and S.H. Lee, "Two-dimensional spatial light modulators fabricated in Si/PLZT," *Appl. Opt.*, **29**, 1595, 1990.

17 W. E. Lee and K. P. D. Lagerlof, "Structural and electron diffraction data for sapphire (α-Al_2O_3)," *J. Electron Micros.Tech.*, **2**, 247, 1985.

18 K. Wasa, T. Satoh, K. Tabata, K. Adachi, Y. Yabuuchi and K. Setsune, "Effects of PLT-buffer layer on microstructures of sputtered PLZT thin films epitaxially grown on sapphire," *J. Mater. Res.*, **9**, 2959, 1994.

19 H. Matsunaga, H. Ohno, Y. Okamoto and Y. Nakajima, "Heteroepitaxial growth of $LiNbO_3$ single crystal films by ion plating method," *J. Cryst. Growth*, **99**, 630, 1990.

2. PLZT ceramics : Background

2.1 Bulk properties

Ferroelectric ceramics are one of the new classes of electro-optic materials finding use in such applications as modulators, optical shutters, displays, color filters, image storage devices, and linear gate arrays for optical data processing. Their success in such applications has been mainly due to a number of characteristics [1,2] : (1) high optical transparency, (2) high electro-optic coefficients, (3) fast response time, (4) high electrical resistivity, (5) direct current (dc) operation, (6) low power consumption, (7) memory capability, (8) good property uniformity over large areas, (9) moisture insensitivity, and (10) low cost. Foremost critical characteristic is high optical transparency since many of the other properties cannot be effectively utilized in electro-optic devices unless the material is capable of coherently transmitting a large portion of the incident light. Electro-optic materials provide a medium by which electrical information can be transformed into optical information or by which optical functions can be performed upon command from an electrical signal. The PLZT ceramics were first produced in transparent form in 1969 [1] and and their large electro-optic effects reported in 1971 by Haertling and Land [2] stimulated much interest for variety of applications.

Research conducted on a large number of modified PZT materials have shown that [1,3,4] La^{3+}, as a chemical modifier, is unique among the off-valent additives in producing

transparency. The reason for this behavior is still not fully understood; however, it is known that lanthanum is to a large extent effective because of its high solubility in PZT oxygen octahedral structure, thus producing an extensive series of single-phase, solid solution compositions. The mechanism is thought to be lowering the distortion of the unit cell, thereby reducing the optical anisotropy of the crystalline lattice and also promoting uniform grain growth and homogeneous densification of a single-phase, pore-free microstructure.

Optical transparency in ceramic materials is not readily attained. Most ceramic dielectric ceramics are intrinsically high bandgap materials ($\approx$ 3 eV) that are transparent to electromagnetic radiation in the optical and near infrared regions (0.3 - 1.0 μm), but conventional ceramics normally possess entrapped pores, second phases, grain boundaries, random grain orientation, grain anisotropy, and internal grain twinning that usually lead to opacity or to moderate degree of optical translucency. Most, if not all, of these factors must be carefully controlled during processing and fabrication if true transparency is desired. Specific control techniques, however, may vary widely, as pointed out by reports [1,5] on several different polycrystalline materials that were fabricated to full density and transparency for the first time in the late 60s and 70s using such methods as hot-pressing, hot swaging, oxygen hot-pressing, liquid-phase sintering, solid-state diffusion, solute-segregation sintering, atmosphere sintering, vacuum sintering, and hot-isostatic sintering.

The solid solution system of lead zirconate and lead titanate have been widely investigated for piezoelectric, pyroelectric and ferroelectric applications [3]. The advantages of PZT ceramics include [3] (1) a high Curie temperature (~ 350°C) and thus higher operation temperatures (2) extremely large piezoelectric coefficients and coupling factors (3) ability to tailor the properties through compositional modification. PZT-PLZT ceramics possess a perovskite structure described as ABO_3. Because of the complete miscibility between lead zirconate and lead titanate and the substantial solubility (up to 40 % at the high $PbTiO_3$ end) of lanthanum oxide in the structure, a high degree of flexibility is possible for optimizing specific desirable properties. A general formula for the PLZT system can be given as

$$Pb_{1-x}La_x(Zr_yTi_{1-y})_{1-x/4}O_3 \tag{2.1}$$

where lanthanum ions replace lead ions in the A site of the perovskite ABO_3 ionic structure shown in Figure 2-1. Since La^{3+} substitutes for Pb^{2+}, charge balance is maintained by the creation of lattice site vacancies. The formula assumes B-site vacancies but it has been shown that both A-site and B-site vacanices coexist and this would provide excess Pb^{2+} ions which would be expelled from the lattice as PbO vapor [4]. Excess PbO, however, is useful in densification process by forming a liquid-phase at the grain boundaries, eliminating porosity and inhibiting grain growth in early stages of densification. Alternately used A-site formula,

$$Pb_{1-\frac{3x}{2}}La_x(Zr_yTi_{1-y})O_3 \tag{2.2}$$

assumes electrical neutrality is maintained by Pb vacancies, one Pb vacancy for every two atoms of La present. However, materials made using this formula cannot be densified without excess lead, and again it is likely that a combined A-site and B-site vacancy is actually present in these materials. The data of weight change during sintering allows the calculation of proportion of A-site and B-site vacancies in the PLZT structure. The percentage of A-site vacancies ranges from approximately 85% for the high-$PbZrO_3$ compositions to 25% for the high-$PbTiO_3$ compositions [5]. It has been reported that PLZT designated 9/65/35 (9 atom %La with Zr/Ti ratio of 65/35) composition contains 74.5% A-site vacancies [4,5]. Because of the large amount of vacancies present, the solubility of oxygen in the lattice and the high volatility of the lead oxide which accommodate for charge imbalance, the composition is recognized to be nominal. Often when La/Zr/Ti is specified, it is more directly referring to a given set of electrical and electrooptic properties.

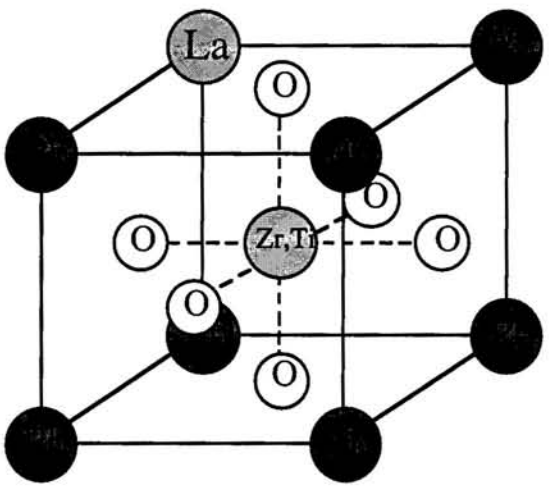


Figure 2-1 Perovskite ABO_3 crystal structure of PLZT (La/Zr/Ti : 9/65/35).

2.1.1 Phase diagram and crystal structure

The phase diagram of PLZT system at room temperature is shown in Figure 2-2 and Figure 2-3 [2,6]. There are some interesting features of this phase diagram which limited to 30% La with all the range for end members $PbZrO_3$ to $PbTiO_3$ [5,6]: (1) complete solid solution exists between the two end members ($PbZrO_3$ to $PbTiO_3$) and La in small concentrations, (2) small variations in La content produce rather large changes in areas of phase stability, (3) the solubility of La in the PZT structure is limited to less than 35%, (4) increasing La decreases the stability of the ferroelectric phases (FE) (rhombohedral and tetragonal) in favor of the nonferroelectric cubic and antiferroelectric, AFE, (a nonpolar phase possessing adjacent, oppositely aligned polar unit cells) orthorombic phases. The FE with rhombohedral structure is biaxial optically and not desirable, while FE tetragonal phase is uniaxial and better for optical applications. The La additions reduce the Curie point in a linear fashion to below room temperature (see Figure 2-3).

The slanted-loop area which is connected from $PbZr_{0.94}Ti_{0.06}O_3$ up to La additions of 27at% (Figure 2-2) existing along the ferroelectric-paraelectric phase boundary represents a region of diffuse, metastable ferroelectric phases that can be electrically induced with a sufficiently high electric field. This phenomenon is commonly described as relaxor behavior, and materials within this region exhibit a quadratic electro-optic effect. In this phase area, the PLZT compositions are transparent. On the other hand, compositions in the mixed-phase region (as-labeled) are opaque in contrast to single phase, cubic materials. Majority of compositions useful for piezoelectric applications lie near or along the

morphotropic (temperature-independent) phase boundary that separates the FE (rhom) and FE (tet) phases because these polar phases tend to show large polarization.

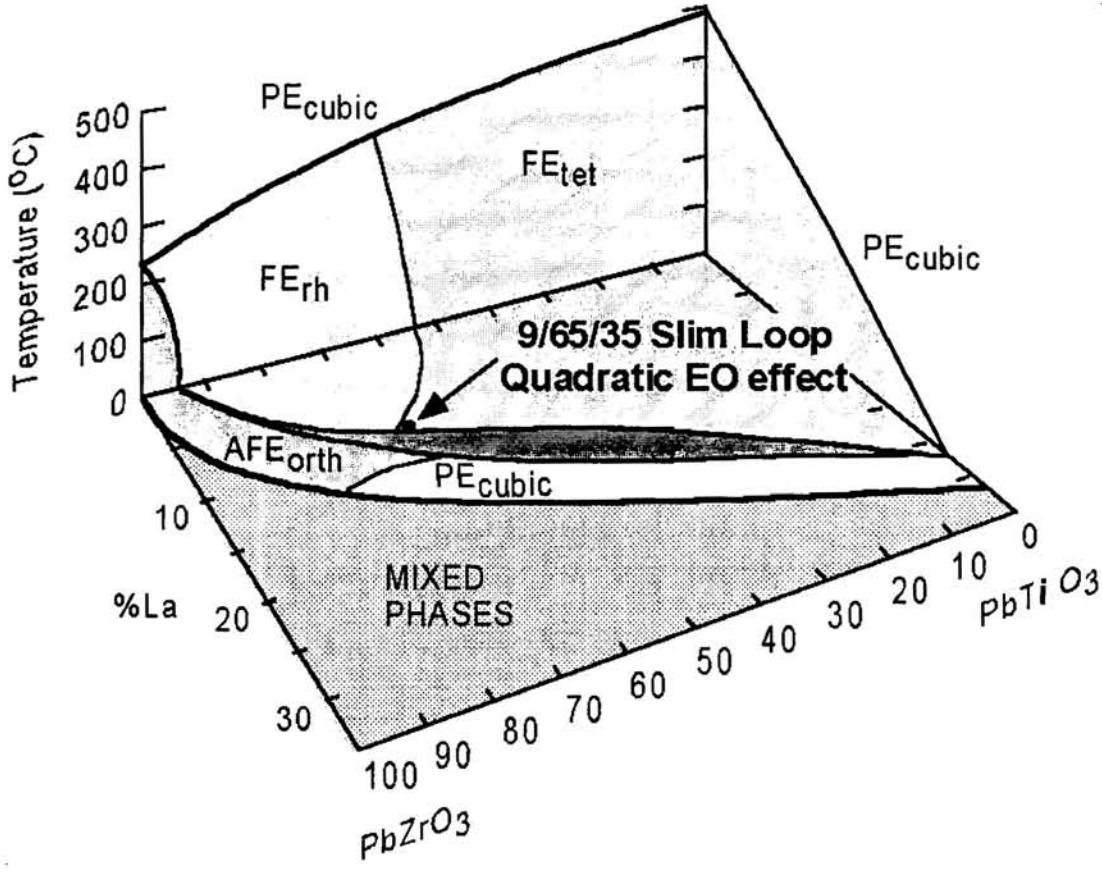


Figure 2-2 Room temperature phase diagram of PZT and PLZT system.

Electro-optic PLZT 9/65/35 and 8/70/30 compositions lie in the slanted loop area near ferroelectric-paraelectric boundary while memory compositions 7/65/35 and 8/65/35 lie in the FE rhombohedral phase region.

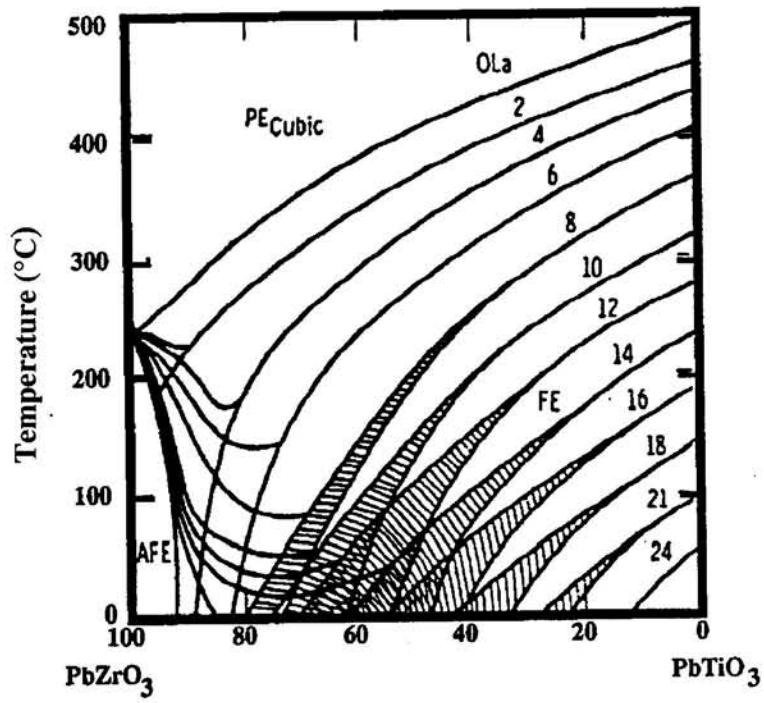


Figure 2-3 Phase diagram of PLZT system showing La concentration levels for various compositions [2].

2.1.2 Microstructure and secondary phases

The characteristic of grains in the bulk PLZT system is one of a highly uniform microstructure consisting of randomly oriented grains. The PLZT ceramics are typically hot-pressed at 1200 °C for 16 h. under 20 MPa [5] and have average grain sizes ranging

from 1 - 8 μm [5,7,8]. The porosity is of concern for electrooptic ceramics because of their required optical transparency. Domain patterns, regions of uniform and homogeneous spontaneous electrical polarization within a grain or between several grains, can also be revealed in the microstructure of ferroelectric (memory or electro-optic) ceramics when chemical etching techniques are used. Micro-regions and micro-domains are observed in ferroelectric phases, orthorombic micro-domains for 7.9/70/30 compositions [8]. With respect to the effect of grain size, grains of 2 μm or less are usually single domain, whereas grains greater than 2 μm most often consist of more than one domain. Smaller grains with single domain structure are better for memory applications. Electro-optic ceramics usually possess grain sizes in a range from 2 to 10 μm, depending on the specific electro-optic effect being optimized. If birefringence is the effect desired, then small grain size is required for memory material and either large or small size for nonmemory. However, if the scattering is of concern, then large grain size is necessary for both memory and nonmemory. Whatever the effect, though, uniform grain size is highly desirable feature from the standpoint of performance.

Another important feature of the microstructure is the presence of secondary phases, precipitates, along the grain boundaries or at triple points between grains. Second phases usually consist of unvolatilized excess PbO or other compounds, such as $La_2Zr_2O_7$ or $La_2Ti_2O_7$, which are present in the material and have developed during calcining or sintering [5]. $La_2Zr_2O_7$ has cubic lattice structure with a lattice parameter of a = 1.0805 nm [9].These phases are undesirable since they can cause opacity in even relatively small

amounts. These phases are usually described as pyrochlore phase, denoted as $A_2B_2O_{7-x}$ defect pyrochlores. The general formula of the oxide pyrochlores can be written as $A_2B_2O_7$ (A and B are metals) with four crystallographically nonequivalent kinds of atom. The space group of the ideal pyrochlore structure is Fd3m and there are eight molecules per unit cell (z = 8). The structure is composed of two types of cation coordination polyhedron as shown in Figure 2-4 [9]. The A cation (usually ~ 0.1 nm ionic radius) are eight coordinated and are located within scalenohedra (distorted cubes) that contain six equally spaced anions at a slightly shorter from the central cations. The smaller B cations (~ 0.06 nm) are six coordinated and are located within trigonal antiprisms with all the six anions at equal distances from the central cations. Since there are four nonequivalent kinds of atom, there are four possible choices of origin. The B cation is commonly the choice of origin.

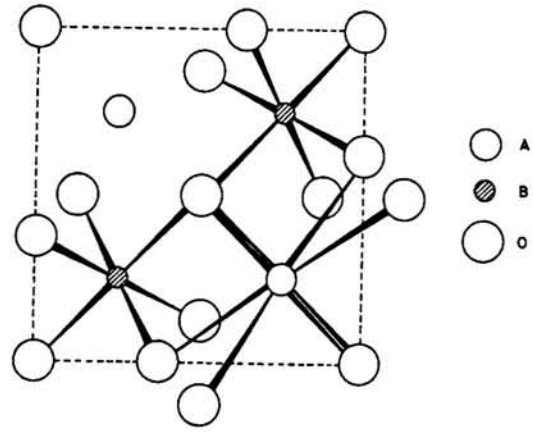


Figure 2-4 Pyrochlore structure of general formula $A_2B_2O_7$ showing the 6 fold coordination of B and 8 fold coordination of A atoms [9].

In a fluorite structure description, the A cations A and B form a face centered cubic array and the anions are located in the tetrahedral interstices of the cationic array. This type of description is of interest in case of compounds with large ionic radius, Zr^{4+} for B site. Another explanation for the existence of $A_2B_2O_6$ (ABO_3) phases with a defect pyrochlore in preference to the adoption of perovskite structure based on the electropositive character of A and B cations. It is noted that perovskite and pyrochlore structures both possess cornershared BO_6 octahedral network, the essential difference being that in perovskite the corner shared octahedra are arranged in a simple fashion and occur in linear strings, running in parallel to the cube axes. In the pyrochlore structure, however, the chain of octahedra are zig-zag lying along [110] direction with BOB angle 130° [9]. The defect pyrochlore structure has a lesser density than the perovskite structure.

2.2 Electrical and electrooptic properties

2.2.1 Dielectric properties

Small-signal, low-frequency (≈ 1 kHz) relative dielectric constant (ε) values from selected compositions in PLZT system are shown in Figure 2-5 [10]. There is a decreasing trend in the peak of dielectric constants as La is increased from 7 to 12 atom % at Zr/Ti of 65:35, and also another notable trend is the decreasing Curie point. Higher concentrations of La not only reduce the dielectric constants but also spread them over a large temperature interval. However, this gradual change in dielectric constant is

advantageous with respect to room temperature for the stable operation of devices, for example for 9/65/35 EO composition.

Diffuse phase transitions (DPT) and relaxor behavior in perovskites ABO_3 are common to some PLZT, PST ($Pb(ScTa)O_3$) and PMN ($PbMg_xNb_{1-x}O_3$) materials-quaternary solid solutions with statistical occupation of the A- and B-sites, or doping at the A-site. Some properties of materials with DPTs are common to all [11] : (1) Even below T_c, the material macroscopically shows the cubic symmetry, (2) the low frequency dielectric constant shows no Curie-Weiss-Law (CWL). The permittivity is strongly frequency dependent (relaxor behavior), (3) the weak field dielectric permittivity reaches a high peak value typical for ferroelectric perovskite near T_c, but the dielectric maximum does not mark a phase change into ferroelectric phase. There are two models that attempts to explain such behaviors, one on the basis of compositional heterogeneities, and the other on the basis of instrinsic instabilities and the broken invariance of the lattice [11]. The first model suggests that there are fluctuations in B-site (off-center ions) concentrations and that these statistical compositional fluctuations lead to large fluctuations in the Curie-temperature. The result is microdomains. So over a wide temperature range, there is a mixture of non polar and polar regions, which are growing with decreasing temperature. If the scale of heterogeneity is of the order of 10-20 nm as proposed [11,12], then for measurements with a probing radiation such as X-ray or optical frequency the random array will reflect the cubic symmetry. The second model considers the local defects which perturb the invariance of the translation symmetry and

which are coupling with the local dipole moments in the relaxor material [11]. It proposes that all materials with DPT has compositions with an intrinsic instability, e.g. with the tendency to rotate the O-octahedra of elementary cells containing a La and a Zr and to stretch the O-octahedra containing a Pb and a Ti respectively. Schmitt et al noted it was extremely difficult to directly compare these two models based on the experimental data [11].

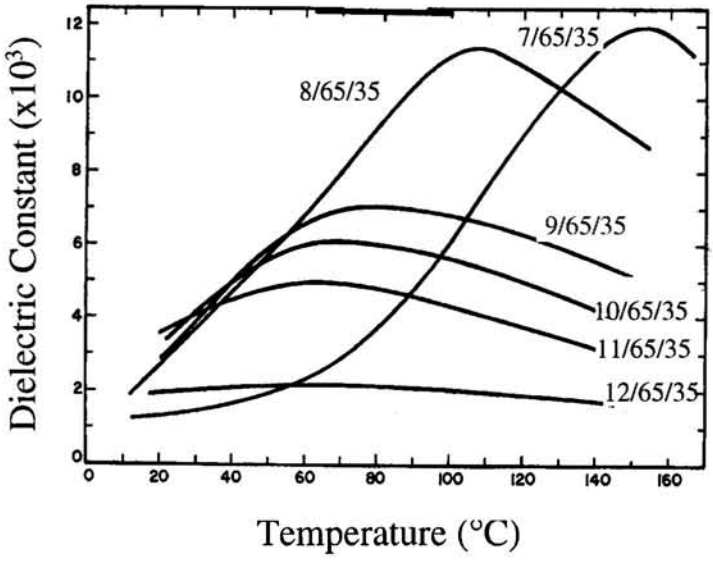


Figure 2-5 Dielectric constant as a function of temperature for PLZT compositions with a 65:35 Zr/Ti ratio [5].

Dielectric losses tend to be higher (5-6 %) for PLZT compositions along morphotropic phase boundary between the rhombohedral and tetragonal phases 8-10 % La, as compared to other PLZT compositions (1-5 %). For PLZT (9/65/35), the bulk

ceramic data indicates that the peak dielectric constant ranges from 5700 [5,10] to 8500 [6] depending on processing and the dielectric dissipation factor is listed as 6.0 % and this composition has slim-loop switching characteristics which shows no permanent polarization [5]. Dielectric constant at room temperature is nearly 4500 for 9/65/35 as seen from Figure 2-5, and at lower temperatures (77K) it was reported that the dielectric constant decreased consistently in value (-80% avg.) for most PLZT compositions [6]. It was generally observed that electric field breakdown strength was significantly higher at 77K than at room temperature with values often exceeding 100 V/μm.

Hysteresis loops for three different types of electrooptic materials in the PLZT system, memory, linear, and quadratic are shown in Figure 2-6 [5]. The memory materials possess permanent remanent polarization P_R, and electrical and/or optical information is stored in the ceramic by the incremental switching of polarization on traversing the hysteresis loop. Desirable characteristics for the memory materials are large P_R and low E_c, the switching field E_c is an indication of grain size, i.e., lower E_c = larger grain size and higher E_c = smaller grain size [5]. The linear materials also possess permanent polarization but in this case they are permanently polarized to saturation remanence P_R and left to remain in that state, and optical information is extracted by the electric field (birefringence change). The slim-loop, quadratic materials do not possess permanent polarization but do exhibit substantial induced polarization when subjected to an electric field. This electrically induced polarization effect is actually an electrically induced phase change from the paralectric, optically isotropic state to the ferroelectric, optically active

anisotropic state. Optical effects in this material are momentary and noticeable only while the electrical field is applied; removal of the field allows the material to relax back to its isotropic nonactive state. The electrically induced birefringence of this material is a quadratic function of the applied field. Desirable characteristics of 9/65/35 material are complete nonmemory (P_R=0) in the unactivated state and a large induced birefringence upon application of electric field.

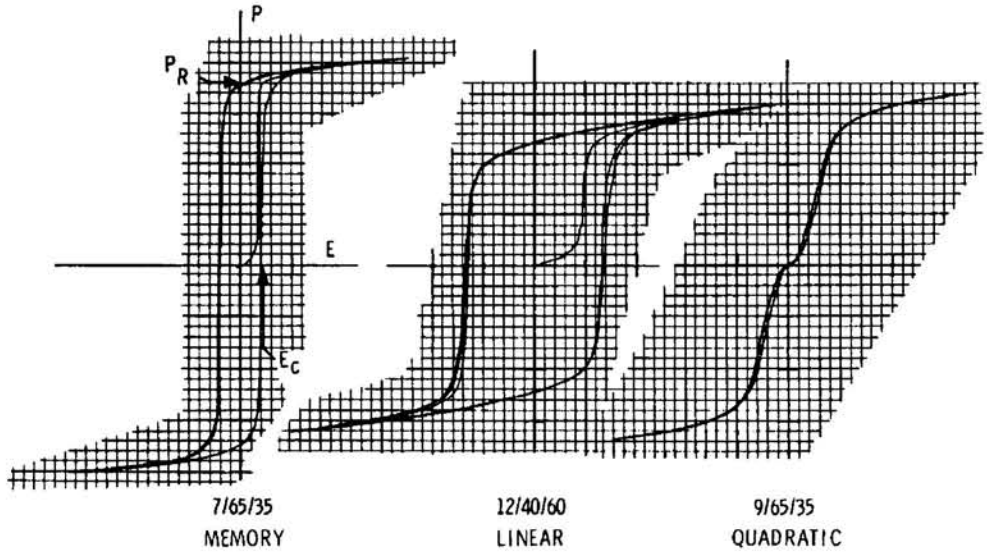


Figure 2-6 Hysteresis loops (P vs E) of the different types of PLZT [5].

Okazaki and Nagata [7] reported that T_cs increased with decreasing grain size in hot-pressed PLZT ceramics. This shift in T_c, which was accompanied by a significant decrease in peak dielectric constant or flattening of the ε versus temperature curve, was attributed to a space charge effect which locked in the ferroelectric polarization. As the

grain size decreased, the surface area of the space charge layer surrounding the ferroelectric grains increased, and the Curie transition was delayed to higher temperatures than normal as the ferroelectric polarization was shielded by this space charge. Okazaki and Nagata determined that a decrease in grain size from 2.5 μm to 0.5 μm corresponded to a greater than 20°C increase in T_c and a decrease of 7000 in peak dielectric constant for PLZT 8/65/35.

2.2.2 Optical properties

One of the most significant feature of PLZT system is its transparency for 8 atom % to 16 atom % La. At low La levels, the higher birefringence and existence of ferroelectric domain walls combine to produce large light scattering whereas at high La levels the secondary precipitated phases in the boundaries cause opacity. In the single phase the individual grains of PLZT are cubic and hence effectively, no light scattering occurs at grain boundaries [12]. The corollary is that only compositions in which the thermally depoled state has been shown to be cubic are expected to yield transparent ceramics. However the scattering is substantial even in thermally depoled state if it has a low symmetry disordered structure. On poling below T_c or applying a bias field above it, light is scattered at the boundaries of the birefringent grains, as well as at the ordered domain walls.

Polished plates of PLZT exhibit essentially 100% transmittance, neglecting reflection losses, as seen in Figure 2-7 optical and infrared transmission of PLZT 9/65/35 [5]. The

fundamental absorption edge is near λ = 0.37 μm. PLZT 9/65/35 is transparent throughout the optical range and well into the IR, 7 μm.

The optical transmission of PLZT wafer can be reduced substantially depending on the existence and the size of defects present. It is well known that defects (porosity) of the same size as the wavelength of light (0.4-0.7 μm) are most effective in scattering light. The porosity should therefore be minimized. For example, 0.2-μm pores are very effective in reducing transmission than 5 or 0.1 μm diameter pores.

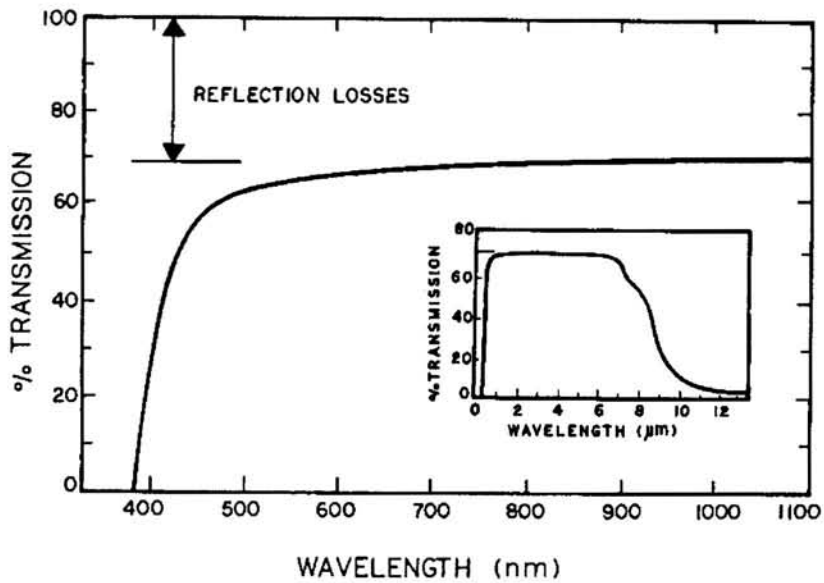


Figure 2-7 Optical and infrared transmission versus wavelength of PLZT 9/65/35 [5].

The index of refraction of a transparent solid is generally not constant but rather varies for different wavelengths (frequencies) of light. This phenomenon, known as

dispersion, is due to a natural absorption mechanism in the ultraviolet (UV) that causes the index of refraction to increase from the red end of the spectrum to the blue end. For instance, the index of PLZT 9/65/35 varies from about 2.4 for 700 nm (red) to 2.5 for 550 nm (green) and above 3.0 for 400 nm (blue). This is seen in Figure 2-8 [13], along with some other PLZT compositions.

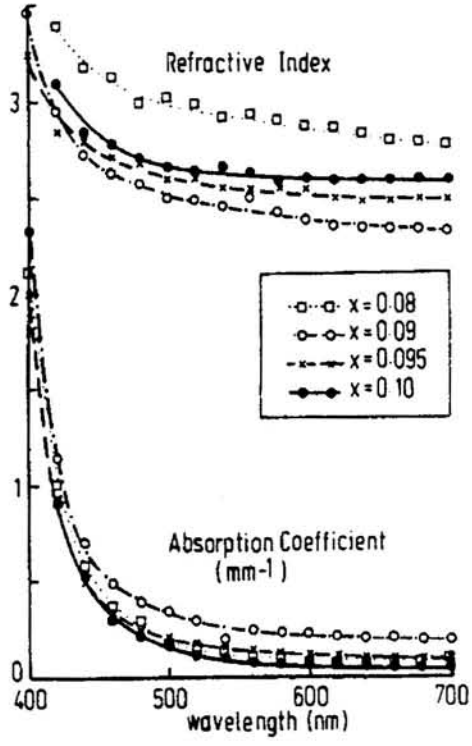


Figure 2-8 Dispersion of refractive index and absorption coefficient in bulk PLZT [13].

Maximum transmittance is limited largely by the reflection losses at the air-PLZT interface. The incoming light will be reflected at an angle equal to the angle of incidence.The fraction of light reflected is given by the Fresnel formula,

$$R = \left(\frac{n-1}{n+1}\right)^2 \tag{2-3}$$

where R is the reflection coefficient in air from a single surface at normal incidence of light and n is the index of refraction of medium. Multiple reflections at the air/PLZT/air interfaces can give rise to a total transmission of 69%. However, this loss problem can be solved by the use of antireflection coatings.

Light transmission, T, through a parallel sided slab of thickness t of material having a refractive index n and absorption coefficient a, is given by [13]

$$T = \frac{I_t}{I_o} = \frac{(1-R)^2 e^{-at}}{1-R^2 e^{-2at}} \tag{2-4}$$

where Beer-Lambert absorption is assumed. As seen in Figure 2-8, at short wavelengths, the absorption is approximately independent of La concentration and shows an exponential dependence on photon energy. The further loss process is the light scattering which is superimposed on absorption losses.

An energy band model is assumed to be applicable to PLZT ABO_3 structure for uv absorption. The band structure has a filled valence band due to oxygen 2p levels and an empty conduction band derived from the transition metal d-orbitals. The role of the A-site atoms in Pb-containing oxides has been proposed such that the s-orbitals of A-site ions from higher lying conduction levels having little effect on the fundamental absorption. On the model, the 2d valence band is split into two components, designated d_ε and d_γ, transitions to these being described by wavelengths λ_ε, λ_γ, and oscillator

strengths S_ε, S_γ respectively. Dispersion theory then shows the refractive index, n, to be given by

$$n^2(\lambda) - 1 = \frac{S_\varepsilon \lambda_\varepsilon^2}{1 - \lambda_\varepsilon^2/\lambda^2} + \frac{S_\gamma \lambda_\gamma^2}{1 - \lambda_\gamma^2/\lambda^2} = \frac{S_0 \lambda_0^2}{1 - \lambda_0^2/\lambda^2} \qquad (2\text{-}5)$$

where the single oscillator parameters, S_o, λ_o are introduced for easier data analysis and are readily related to the quantities S_ε, S_γ, λ_ε, λ_γ. It will noted from that the absorption coefficient shows a maximum for the composition x = 9 (La%) over x = 8 or 10 over the whole wavelength range examined. As a shift in wavelength of the absorption band edge, this behavior correlates with the peak in oscillator position (λ_o) from the analysis of refractive index data of bulk PLZT.

2.2.3 Electro-optic effect in PLZT

PLZT ceramics exhibit three different electro-optic effects depending on the composition [5] : (1) Quadratic (Kerr effect) electro-optic response with a squared relationship between birefringence n and electric field E, (2) linear response (Pockel effect) with a linear relationship between n and E, and (3) memory response with switchable remanent electro-optic states. The first and most widely used electro-optic response is the quadratic effect because it is displayed by essentially cubic phase located close to ferroelectric rhombohedral or tetragonal phases. They are not optical birefringent and possess no permanent polarization due to cubic high-symmetry. The birefringence is

created by a transverse electric field (or strain in the case of strain-optic effect) and dissappears when the field is removed. The strain-optic effect constitutes a significant portion of quadratic electro-optic effect in PLZT, perhaps nearly 65% as suggested by Kirkby [14].

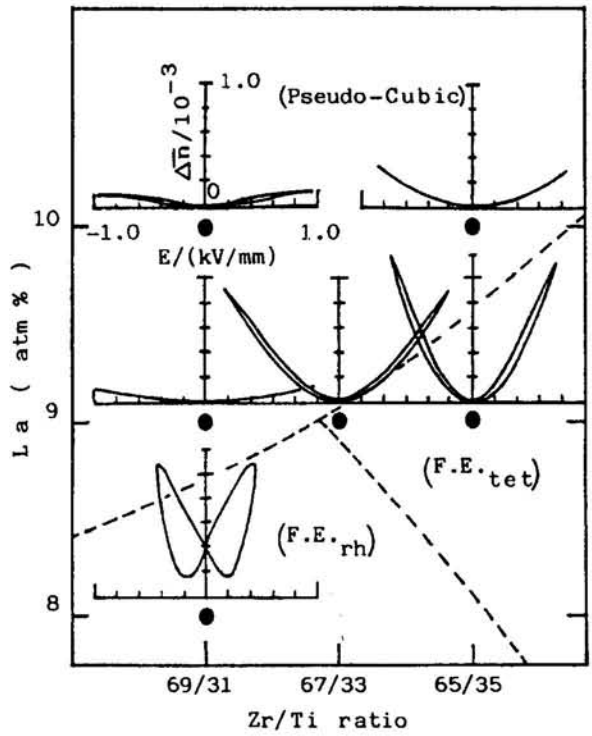


Figure 2-9 Birefringence of bulk PLZT versus electric field at 25°C [15].

Memory and quadratic responses of three compositions are seen in Figure 2-9 [15], as 9/69/31 composition shows birefringence butterfly hysteresis while 9-10/65/35 exhibit slim-loop quadratic curves. High coercivity tetragonal PLZT 12/40/60 exhibit linear EO effect. The truly linear, anhysteretic character if this effect has been found to be intrinsic

to the material, not due to domain reorientation processes that occur in the quadratic and memory materials. Similarly 8/65/35 composition show large polarization (and hysteretic) as it has rhombohedral phase, as opposed to slim-loop character of quasi-cubic 9/65/35 composition. PLZT 9/65/35 is the choice of this study because of its very large quadratic effect and slim-loop polarization versus electric field characteristic. It is ideal choice for fast switching high speed operation of light modulators in smart pixel applications.

The velocity (υ) of a monochromatic light beam propagating through a crystal is related to the index of refraction (n) in the direction parallel to the electric field vector, where c is the speed of light, is given by

$$\vartheta = \frac{c}{n} \tag{2-6}$$

The index of refraction varies with direction within the crystal, depending on symmetry. Three principal refractive indices (n_1, n_2 and n_3) are along the three principal directions (x_1, x_2 and x_3), except in crystals with the lowest symmetry (monoclinic and triclinic). The effective index of refraction and the principal polarization directions for an arbitrary direction of wave propagation in a crystal can be found by the construction of an optical indicatrix (or index ellipsoid), given by [16]

$$\frac{x_1^2}{n_1^2} + \frac{x_2^2}{n_2^2} + \frac{x_3^2}{n_3^2} = 1 \qquad \text{or} \qquad B_1 x_1^2 + B_2 x_2^2 + B_3 x_3^2 = 1 \tag{2-7}$$

where the quantities

$$B_1 = \frac{1}{n_1^2},\ B_2 = \frac{1}{n_2^2} \text{ and } B_3 = \frac{1}{n_3^2}$$

are the relative optical-frequency dielectric permeabilities. In isotropic materials (cubic crystals and glass), the three principal refractive indices are identical (n_1=n_2=n_3); the indicatrix corresponds to a sphere, and the velocity of light propagation is independent of direction within the crystal. For hexagonal, tetragonal and trigonal crystals are optically uniaxial, the indicatrix is an ellipsoid of revolution about the principal symmetry axis (defined by x_3 or optic axis) and the refractive indices n_o and n_e give the wave velocities.

PLZT 9/65/35 is cubic belonging to the point group m3 [2]. The optical index ellipsoid of light passing through the material can be written as [see Appendix for details]

$$\eta_{11}x^2 + \eta_{22}y^2 + \eta_{33}z^2 + 2\eta_{12}xy + 2\eta_{13}xz + 2\eta_{23}yz = 1 \qquad (2\text{-}8)$$

where n_{ij} is the impermeability tensor. The quadratic EO coefficients can be also written in a matrix form as given by eq. (2-9).

$$\begin{pmatrix} s_{11} & s_{12} & s_{13} & 0 & 0 & 0 \\ s_{12} & s_{11} & s_{13} & 0 & 0 & 0 \\ s_{13} & s_{13} & s_{33} & 0 & 0 & 0 \\ 0 & 0 & 0 & s_{44} & 0 & 0 \\ 0 & 0 & 0 & 0 & s_{44} & 0 \\ 0 & 0 & 0 & 0 & 0 & s_{44} \end{pmatrix} \qquad (2\text{-}9)$$

The measured electrooptic (EO) coefficients at room temperature were (s_{11}-s_{12}) reported in the literature which were used in the calculation of electric field induced birefringence of cubic PLZT [17].

In the absence of an electric field polycrystalline PLZT 9/65/35 is isotropic with an index n. When an electric field is applied along y, it can be shown that maximum birefringence occurs when the wave normal (direction of propagation) of light beam through the material is perpendicular (along z) to the applied electric field (transverse mode of operation). In this case the crystal becomes negative uniaxial with the optical axis parallel to the direction of the electric field and the principal refractive indices for an electric field E are given by

$$n_o = n - \frac{n^3 s_{12} E^2}{2} \tag{2-10}$$

$$n_e = n - \frac{n^3 s_{11} E^2}{2} \tag{2-11}$$

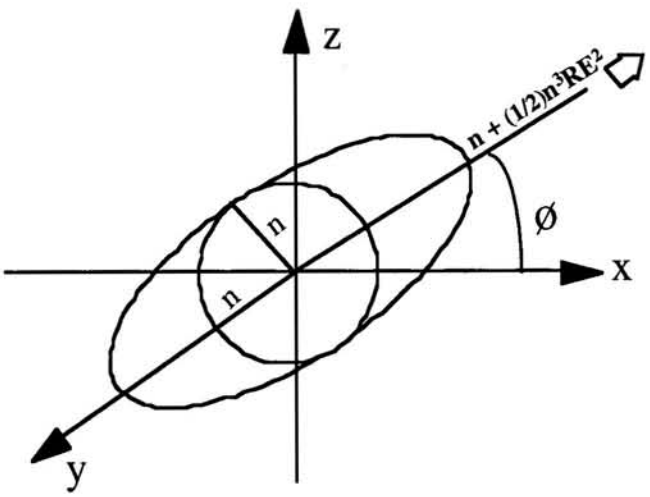


Figure 2-10 Optical index ellipsoid of cubic PLZT with applied electric field.

The phase retardation Γ of the beam is given by

$$\Gamma = \frac{2\pi t\Delta n}{\lambda} = \frac{2\pi t(n_e - n_o)}{\lambda} = \frac{\pi t n^3 E^2}{\lambda}(s_{11} - s_{12}) \qquad (2\text{-}12)$$

where t is the thickness of PLZT, λ is the wavelength of operation and R = s_{11} - s_{12}. The modulation in intensity I obtained by placing PLZT between crossed polarizers is given by I = $\sin^2(\Gamma)$.

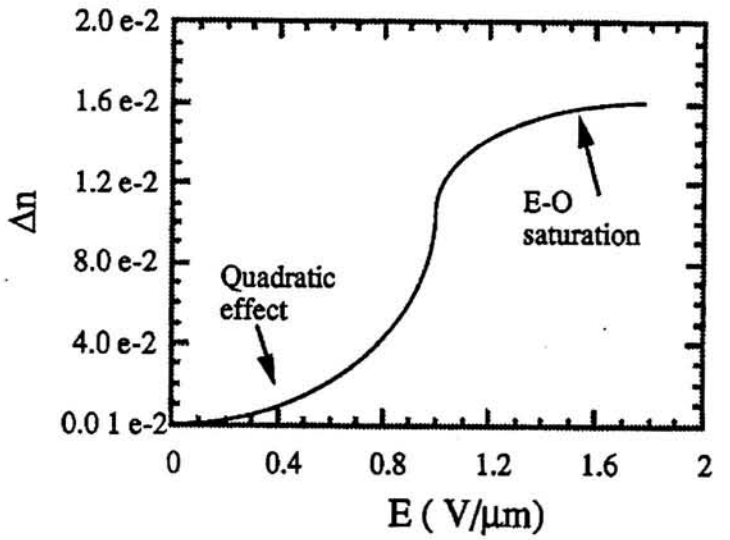


Figure 2-11 Electrooptic effect in PLZT 9.5/65/35 [18].

When a field E is applied, the index ellipsoid stretches in the direction of the field. The birefringence in this direction (major axis of ellipsoid) is n+(1/2)n^3RE^2, where R is the quadratic coefficient, as seen in Figure 2-10. In the case of PLZT 9.5/65/35, Mansoorian observed that the electro-optic effect saturates for electric field values above 1 V/μm

(Figure 2-11) [18]. This implies that the birefringence for an applied electric field E is smaller than predicted by the equation.

This chapter analyzed the characteristics of PLZT ceramics and it was seen that PLZT 9/65/35 shows attractive features for modulator applications; a very large quadratic coefficient and a slim-loop polarization versus elelctric field characteritic. A summary of previous research in thin film PLZT is given in the next chapter, chapter 3. The discussion involves deposition methods and PLZT film characteristics of various compositions and the emphasis was on the electrooptic compositions. In chapters 4 and 5, we discuss our results in deposition/annealing and characterization of PLZT 9/65/35 films.

References

1 C. E. Land, and P. D. Thacher, "Ferroelectric ceramic electrooptic materials and devices," Proc. IEEE, vol. **57**, p.751, 1969.

2 G. H. Haertling, and C. E. Land, "Hot-pressed (Pb,La)(Zr, Ti)O_3 ferroelectric ceramics for electrooptic applications," *J. Amer. Ceram. Soc.*, **54**, 1, 1971.

3 B. Jaffe, W. Cook, and H. Jaffe," Interpretation of some experimental results, " in Piezoelectric Ceramics, Academic Press, New York, p. 237, 1971.

4 K. H. Hardtl, and D. Hennings, "Distribution of A-site and B-site vacancies in (Pb,La)(Zr,Ti)O_3 ceramics," *J. Amer.Ceram.Soc.*, **55**, 230, 1972.

5 G.H. Haertling, "Electro-optic ceramics and devices," in Electronic Ceramics, ed. by L. M. Levinson, Marcel Dekker, Inc., New York, p. 371, 1988.

6 G. H. Haertling, "Room temperature and 77K dielectric properties of acetate-derived PZT, PLZT and PBZT thin films," *Integ. Ferroelectrics*, **10**, 257, 1995.

7 K. Okazaki and K. Nagata, "Effects of grain size and porosity on electrical and optical properties of PLZT ceramics," *J. Amer. Ceram. Soc.*, **56**, 82, 1973.

8 Z. W. Yin, X. T. Chen, X. Y. Song, and J. W. Feng, "Studies on microstructure and microproperty of PLZT ceramics," *Ferroelectrics*, **87**, 85, 1988.

9 M. A. Subramanian, G. Aravamudan and G. V. Subba Rao, "Oxide pyrochlores - A Review," *Prog. Solid. St. Chem.*, **15**, 55, 1983.

10 C. E. Land, P. D. Thacher and G. H. Haertling, "Electro-optic Ceramics," in Applied Solid State Science, Academic Press, vol. **4**, p. 137, 1974.

11 H. Schmitt, D. Simon and P. Pitzius, "Diffuse phase transition and relaxor behavior in perovskites,' in Proc. 1992 IEEE Int. Symp. on Appl. of Ferroelectrics, ed. by M. Liu, A. Safari, A. Kingon and G. Haertling (S. Carolina, USA, 1992), p. 76.

12 E. T. Keve, "Structure-property relationships in PLZT ceramic materials, " *Ferroelectrics*, **10**, 169, 1976.

13 C. J. Kirkby, "Dispersion of optical and electro-optic properties of hot-pressed PLZT ceramic materials," *Ferroelectrics*, **7**, 157, 1974.

14 C. J. Kirkby, "Electrostriction and strain-optic phenomena in PLZT 9/65/35," *Ferroelectrics*, **37**, 567, 1981.

15 K. Hikita, Y. Tanaka, M. Hirama and M. Ono, "Dependence of electro-optic properties of PLZT upon the chemical compositions," *Ferroelectrics*, **94**, 73, 1989.

16 A. Yariv and P. Yeh, Optical Waves in Crystals, chapter 7, Wiley Interscience, 1984.

17 G. H. Haertling and P. D. Thacher, "Electrooptic properties of PLZT ceramics," Proc. IEEE, vol. **60**, p.450, 1972.

18 B. Mansoorian, PhD Thesis, University of California, San Diego, 1994.

3. PLZT thin films

PLZT ceramics have been extensively studied for electrooptic applications as discussed in the preceding chapter. PLZT thin films, however, have not been well characterized and much work is needed for optimizing their properties with respect to specific applications. More research was done on PZT films particularly for memory applications. This chapter presents and discusses the previous work on the deposition and characterization of PZT, PLT and PLZT thin films by several different methods for variety of applications. $PbZr_{1-x}Ti_xO_3$, $Pb_xLa_{1-x}TiO_3$ and $Pb_xLa_{1-x}Zr_{1-y}Ti_yO_3$ are commonly referred to as PZT, PLT and PLZT.

3.1 Summary of previous work

Ferroelectric thin films of PZT, PLT and PLZT have received great deal of attention due to their potential in a number of potential applications in ultra large scale integrated (ULSI) dynamic random access memory (DRAM), thin film (surface acoustic wave) transducers, optical switches, displays, optical light modulators, waveguide modulators, frequency doublers, piezoelectric devices, second harmonic generation (SHG) and pyroelectric (IR) detectors. Ferroelectric films of PZT-family have been extensively studied for memory applications, however, more recently for memories PLZT thin films are reportedly gaining ground because of their higher dielectric constant and lower coercive field as well as their promising fatigue, retention and aging characteristics [i]. Electro-optic device applications of ferroelectric (FE) thin films demand high quality, highly

transparent films with large EO response with little or no polarization hysteresis. Although a number of compositions of PLT and PLZT have been investigated for EO purposes, the relationship between electrical, electro-optical and structural properties are not well investigated.

Large volumes of research on FE thin films concentrated on memory applications in the past. It has been reported that ferroelectric random access memories (FRAMs) because of their lower writing voltages, faster writing speeds, better endurance, and possibly fewer manufacturing process steps have the potential to replace current state-of-the-art floating gate non-volatile memories such as electrical erasable programmable read only memories (EEPROMs) and flash EEPROMs [2,3]. In a ferroelectric, the polarization consists of a non-remanent component which is caused by non-ferroelectric ionic and electronic polarizability as well as field-induced spontaneous ferroelectric domain wall motion and a remanent component induced by ferroelectric domain switching which represents the non-volatile memory signal margin [3]. The film thicknesses for PZT are usually very small in the range of 150-200 nm as thinner films have higher capacitance (i.e. non-remanent polarization), which is undesirable for non-volatile memory operation, while thicker films require higher voltages to switch the polarization state. For the thickness of 150 nm and 1.5 V memory operation, the energy required is 200 fJ μm^{-2} for one switching cycle as reported by Moazzami [3]. This low energy consumption for both read and write operation makes FE non-volatile memories very attractive compared with floating gate memories, especially since no high-voltage pump is

required to write to a memory cell. Memory devices require bottom electrodes (commonly Pt) which becomes critical in film processing since their interaction with the substrate/PZT posed significant challenges to researchers as they tried to grow and integrate PZT films. Numerous deposition methods have been employed to obtain PZT films on conductive electrodes and substrates.

There are only few reports on PLZT films for infared (IR) sensor applications. PLT and PLZT with lower dielectric constants have been studied for pyroelectric detector applications for better voltage responsivity, primarily on Pt and MgO substrates. Pyroelectric coefficient of $8.2x10^{-8}$ $Ccm^{-2}°C^{-1}$ was obtained for magnetron sputtered PLZT 7/80/20 thin films with 0.5% MnO_2 doping [4]. The published figure of merit data on PLT/PLZT films seem to be promising for such applications. The convention used by researchers in electro-optic compositions of PLT/PLZT is such that the designation x/y/z stands for atomic ratios of La/Zr/Ti.

Electro-optic applications of FE thin films have been pursued mainly for optical waveguides, where the light propagates in the film, and for light modulators and displays in which the optical propagation is through the film. The refractive indices of PLZT are in the range 2.2-3.0 in the spectrum 0.4-0.9 μm. Substrates that have been used for waveguiding were sapphire, quartz and $SrTiO_3$, with n = 1.76, 1.4 and 2.39 respectively, since they permit excitation and propagation of guided modes. Highly transparent and highly dense thin films are required for low-loss optical waveguides. Films usually show scattering losses, waveguiding distances up to 1 cm have been observed in some PZT

films [5]. PLT 28/0/100 thin-film channel waveguides have been formed and quadratic EO (Kerr effect) coefficients of R = 0.1-0.2x10^{-16} $(m/V)^2$ have been demonstrated on c-sapphire [6]. It was recently reported that sol-gel derived polycrystalline PLZT 28/0/100 (0 at% Zr) yielded very low losses 2 dB/cm on glass substrates [7]. Single-phase PLT/PLZT with small grain sizes are reportedly favorable for optical waveguides. The maximum linear electro-optic coefficient *r*, 81 pm/V, for sputtered PLT film [8] is significantly larger than that of sputtered $LiNbO_3$, r = 1.34 pm/V [9] or that of bulk $LiNbO_3$, r_{max} = 31 pm/V . More recently higher linear EO coefficients have been reported for sol-gel polycrystalline PZT 53/47 on glass substrates, r = 315 pm/V [10], and a somewhat less for epitaxial sol-gel PZT 65/35, r = 108 pm/V [11]. The tetragonal PLZT films on silicon were deposited by laser ablation and observed linear coefficient was r = 153 pm/V [12]. The field-induced second-harmonic generation in PLZT 28/0/100 on fused silica [13] and PLZT 35/0/100 (0 at% Zr) on platinized silicon [14] have been observed. The PLZT 35/0/100 responded with a rise time of 10 ps to a step-function electric field derived from a fast photoconductive coplanar waveguide structure switch and therefore proposed to be used for probing of electric fields in integrated circuits up to 100 GHz [13].

Reports of PLZT thin films geared towards spatial light modulators for free-space interconnects are only few. For such applications the transparency requirement is not as strict as waveguide structures, however the hysteresis effect has to be minimal as transient memory slows the frequency response of quadratic EO modulation (also lower

contrast ratios). The linear EO effect is usually smaller and is associated with tetragonality of the structure, thus larger quadratic effect with slim-loop PLZT characteristics should be favored for SLMs. Fabry-Perot structures can be used to increase optical interaction lengths and thus the effective modulation in the thin films to realize the bulk PLZT response. The high quality PLZT films grown on silicon or compatible substrates are necessary to meet standard processing and packaging methodologies of standard electronic components and realize the advantages of using PLZT thin film for the light-modulating function of an electrically or optically addressed SLM technology incorporated with the VLSI. Earlier research has been mainly carried out on uncompatible substrates, silica, c-sapphire, glass, $SrTiO_3$, $MgAl_2O_4$ although few efforts were noted on the use of coated-silicon and r-plane sapphire which is silicon-compatible due to commercial SOS (silicon-on-sapphire) technology. Mukherjee et al. [15] investigated the rf planar sputtering of PLZT 28/0/100 on silica and measured EO coefficent of 0.06×10^{-16} $(m/V)^2$ while Luo et al. [16] measured EO coefficient of 0.6×10^{-16} $(m/V)^2$ for the magnetron sputtered films of identical composition on glass substrates. Adachi et al. [8] reported sputtered PLZT 28/0/100 and 9/65/35 thin films on c-sapphire with R, 0.6×10^{-16} $(m/V)^2$ and 1.0×10^{-16} $(m/V)^2$ respectively. Their PLT-buffered PLZT 9/65/35 films showed higher R but exhibited enormous hysteresis in birefringence shift possibly due to graded composition profile [17]. Preston and Haertling studied PZT 0/65/35 and PLZT 9/65/35 films by sol-gel on randomly oriented transparent sapphire and glass substrates with PLT buffer layer [18]. Thin films on glass exhibited smaller

birefringence shift as compared to the ones on sapphire. PZT film on sapphire showed a large memory EO effect of $\Delta n = 17x10^{-3}$ and PLZT a smaller but symmetric response of $\Delta n = 2.5x10^{-3}$ with small hysteresis. PLZT 7/0/100 thick films deposited on silica by CVD exhibited very low transmission, 60%, yet showed quadratic response in the order of $4.5x10^{-16}$ $(m/V)^2$ [19]. The EO measurement errors have been estimated to be approximately 25%. The birefringence shifts were not measured for negative electric fields to check for hysteresis effects. This composition is in the tetragonal region in the phase diagram and expected to show large asymmetry in EO response with a large hysteresis. Large asymmetric hysteresis in birefringence shifts have been observed in sputtered PLZT 7/0/100 and PLZT 8.5/65/35 thin films on fused silica earlier (1990) [20]. It is apparent that PLZT 7/0/100 composition is better suited for optical storage due to its strong remanent birefringence rather than for fast-switching SLMs. Krishnakumar et al were the first to report PLZT 9/65/35 films by magnetron sputtering on r-plane with quadratic EO coefficients $R = 0.6x10^{-16}$ $(m/V)^2$ [21]. This composition on r-sapphire seems to be the most compatible for SLMs to be integrated with silicon driver electronics.

Dielectric constants of PLZT thin films are often quite lower than their bulk counterparts. The Curie temperatures have also been observed to change, often increase in thin films as compared to their bulk values. These differences are not well understood but are usually ascribed to the clamped nature, stressed, of thin films as compared to bulk ceramics and also the smaller grain sizes in the thin films. It should be noted that deposition method, the choice of substrate and processing conditions seem to have

remarkable influence on electrical properties of PLZT thin films. Teowee et al have studied the dielectric properties of sol-gel derived PLZT films and summarized the dielectric properties of a wide variety of thin-film PLZT compositions in the literature [22]. The range of reported values of dielectric constant of PLZT 9/65/35 is between 500 to 1750 at room temperature on silicon, sapphire and glass. The room temperature bulk ε_r of 9/65/35 is 4500 as reported in the previous chapter. The mismatch in thermal expansion coefficients of the substrate and the film, porosity, grain size, film/substrate interface layers all play a role in determining dielectric constant of these films. The PLZT 9.5/65/35 films (0.9 μm) on silver foil which can undergo large deformation which allows stress relaxation have been reported to have large dielectric constants, 1750, and as opposed to 420 on Pt/Si [23]. Similarly large values of ε_r, 4000, were reported on silver foil for sol-gel thin-film 9/65/35 composition. The Curie phase transitions were shifted to higher temperatures, 130 °C for 9.5/65/35 thin film on silver and 160°C on Pt/Si.

3.2 Thin-film deposition methods

PLZT thin films have been deposited by many techniques including (dc, rf) sputtering [1,15,24,25], ion-beam deposition [26], laser ablation [27,28,29,30], sol-gel [7,31,32,33], metalorganic decomposition (MOD) [23,34], and metallorganic chemical vapor deposition (MOCVD) [19,35,36]. From the point of view of commercial production of PZT/PLZT films, there are some difficulties such as low film density (porosity), compositional nonuniformities across large wafers (i.e. 10.16 cm (4″) wafers), high temperature deposition, rough surface morphology, lack of appropriate precursors in

the gas phase and non-conformal step coverage, for chemical methods and also for laser ablation. Of the physical methods, the sputtering has evolved into rf diode, rf planar magnetron and rf triode magnetron sputtering. The most versatile and best suited for multicomponent oxide deposition is the rf triode planar magnetron sputtering, which we will describe in the next section 3.3 as this technique was the choice in this study.

Table 3-1 FE thin film deposition methods. Scale: 1-worst, 10-best [37].

Method	Rate Å/min	Epitaxy 1-10	Stoichiometry 1-10	Wet/Dry	Temperature (°C) Substrate	Anneal	Devices	Cost	Miscellaneous Problems
RF Sputter	5-50	8	3	D	RT-700	500-700	1-7	H	Negative ions
Magnetron Sputter	50-300	5	5	D	"	"	1-7	H	Target surface
RF Magnetron	50-100	9	5	D	"	"	1-7	H	
Ion beam Sputter	20-100	9	6	D	"	"	1-7	H	Uniformity
Evaporation	100-1000	7	4	D	"	"	1-7	H	Rate control
Laser Deposition	50-1000	9	6	D	"	"	1,3,5	H	Debris, Uniformity
Sol-Gel	1000Å/C	2-8	9	W	RT	450-800	1,2,3,5	L	Multiple coating
MOD	3000Å/C	2	9	W	RT	500-800	1,3,5	L	High T_{anneal}
MOCVD	50-1000	5	7	D	400-800	600	1-6	H	High T_s

	Devices
1	Capacitor
2	Memory Cell
3	Actuator
4	Electro optic
5	Pyrodetector
6	IR Imager
7	SAW

Table 3-1 compares the common FE thin film deposition methods [37]. The advantages and disadvantages are listed in terms of growth rate, epitaxy, stoichiometry, deposition temperature, cost and prevalent problems. MOCVD shows great promise in deposition of high-quality FE thin and thick films. Although MOCVD offers good step

coverage characteristics, the lack of environmentally safe liquid precursors with low vapor pressures poses difficulties for future in deposition of complex Pb-La containing systems. The existence of unwanted PbO grains in the PZT/PLZT thin films [35] and the occurrence of parasitic chemical reactions between La-precursor and oxygen were noted [36]. The deposition temperatures used were not low and in the range between 535°C - 800°C.

The other two chemical deposition techniques, sol-gel and MOD usually use unheated substrates, commonly the former utilizes hydrates or alkoxides and the latter the acetates as the starting materials or chemical precursors. The spin-coating and annealing steps continue successively until the desired film thickness is reached. The sol-gel and MOD are relatively inexpensive and convenient techniques. These wet processes are successful in controlling stoichiometry. However, the grain sizes achieved are very small and film transparency is compromised due to scattering from remaining porosity [31]. The dielectric constants by such wet processes are usually lower than those of films by sputtering on identical substrates [22,34]. The epitaxy or orientation in the films are difficult to obtain due to deposition at room temperature. The research on sol-gel of PZT thin films have been largely driven for memory devices and lately thin films with good polarization characteristics have been achieved. For optical applications though, the presence of interfacial layers between coatings which leads to enhanced scattering for thicker films creates loss problems for waveguides.

Of the physical deposition techniques, the excimer laser deposition or pulsed plasma deposition (KrF excimer laser at 248 nm) is well suited for research and development as it can use relatively small singular targets [27]. Optical dielectric coatings and superconductors have been successfully deposited by this technique [30]. Physical processes such as evaporation and sputtering of many components can occur simultaneously during laser ablation. Laser desorption from the target under high intensity (plasma-forming) conditions can also produce a variety of high energy atoms, molecules, fragments and ions can result in local annealing, and chunks of loose target species reaching the substrate can lead to thickness and compositional nonuniformities across the films. The deposition of films over large substrates (10.16 cm) is problematic since it would require using much higher laser power, scanning over rotating target and moving the substrate at the same time.

3.3 Sputtering techniques and RF planar magnetron sputtering

Various sputtering processes such as dc, rf or magnetron sputtering differ in the manner in which a glow discharge is created, but basically all operate on the same basic principles. In diodes the target serves a dual purpose. It is both the source of coating material and cathode electrode for sustaining the glow discharge. The requirement for sustaining a discharge is that each electron must produce sufficient ions to release one further electron from the cathode.The probability for ion production by energetic electrons passing through low pressure argon is low. Consequently, discharges can be sustained only at relatively high working pressure where a large number of argon

collisions are provided by the production of secondary electrons. Typical operation of metal dc planar diode sputtering is around 75 militorr (10 Pa) at 3 kV discharge voltage [38].

Triode systems are particularly useful for applications where deposition at low voltage are required to avoid radiation damage [38]. Triodes operate at lower pressures than diodes, typically around 1 micron, and as a result, will have less gas incorporated in the film and improve density. In a triode system, electrons emitted from a hot filament are attracted to a positive charged electrode. The collision of electrons with the gas atoms, commonly Ar, creates ionization and a plasma that is independent of the target voltage. A negative potential applied to the target will extract the ion and sputtering takes place. Magnetrons utilize a magnetic field at a right angle to the electric field to increase ionization efficiency in the plasma. Such systems provide [38] ; 1) relatively high deposition rates, 2) large deposition areas and 3) low substrate heating. In rf magnetron sputtering, high discharge currents can be obtained at low discharge voltages leading to high deposition rates.

Deposition of PLZT is often done in argon environments and in some cases with bleeding some O_2 gas < 10% of the mixture, which is called reactive sputtering. The addition of oxygen even higher amounts reportedly helps decreasing Pb loss in the laser ablated PLT films [27]. The reactive environment however can etch the PLZT target surfaces quickly depleting the surface unevenly, thus shortening its life dramatically as well as changing the stoichiometry of the films in magnetron sputtering.

Preferential sputtering of the target is a problem in sputtering. It happens [38] 1) when the atoms in the target have relatively different sputtering yields (atoms per ion), 2) the differences in the chemical binding energy between constituents of the target and lastly 3) thermal heating of the target surface. The lead loss from the target surface can result form excessive surface heating since lead is known to have very high vapor pressures. The collision cross-section of an argon ion decreases as its energy rises and fewer collisions occur at a critical recoil zone (depth), but more energy is transferred on each impact and the yield tends to reach a peak value. It should be pointed out that the yield of most metals are about unity and are within an order of magnitude of one another [38]. This is in contrast to evaporation where the rates of different materials at a given temperature can differ by several orders of magnitude. It is this universality that makes sputtering such an attractive process for many applications.

Another critical parameter in deposition of multicomponent oxide thin films is the substrate temperature. The extent of chemisorption of sputtered species on the substrate is directly related to their sticking coefficients on the particular substrate at a given temperature. Generally, the higher the deposition temperature ($T_{substrate}$), the lower the sticking coefficient and lower the deposition rates due to reevaporation. The substrate temperature has a direct impact on the crystal structure, composition and microstructure of PLZT thin films. To generate defect-free structures, it is necessary to impart some kinetic energy for diffusion to the deposited atoms. This as-deposited film structure is precursor for the formation of the desired phase which is usually formed after an

annealing process. The excess Pb is found to be necessary in the target due to possible thermal depletion in the target and reevaporation of Pb if the substrate temperature is high. The control of Pb content is the primary challenge in sputtering of stoichiometric PLZT thin films.

In oxides like PLZT, the more electronegative constituent oxygen can be ejected from the surface as a negative ion. The energetic oxygen ion can then bombard the film surface resulting in what is called negative ion resputtering. The resputtering is likely to occur when negative ions are formed at the target and accelerated away from the negatively biased target toward the growing film. Stoichiometry changes can result due to different sputtering yields of components of a compound. Micro- and macroeffects (thickness reduction) of resputtering can be serious for growing films. Ripples, cones, ridges and etch pits of variuos shapes and sizes have been observed on films [39]. Sputtering geometry is an important parameter which influences the focusing (and angles of incidence) of negative ions, and thereby their flux at different locations. We have used an off axis geometry and larger substrate-target distances which reduces the resputtering. A low power level can eliminate both the micro- and macro-effects of sputtering but at the expense of very low deposition rates. Higher pressures can increase differential scattering the neutral atoms and the negative ions, and thus reduce resputtering, however, again lowering the growth rates.

Of the thin film deposition methods, rf triode planar magnetron is strikingly versatile and best suited for multi component oxide growth as discussed in this and the previous

section. Because of the need for high optical quality PLZT films with high density, the RF triode planar magnetron sputtering was chosen in this study as the method can yield films relatively free of radiation damage and also provides high deposition rate, large deposition areas and low substrate heating. Therefore this technique with an off-axis geometry and a large substrate-target distance was chosen for depositing PLZT films in this work which we will discuss in the next section. To understand the phase transformation behavior and to circumvent the formation of secondary phases, PLZT films were deposited at a range of substrate temperatures and subsequently annealed either by rapid thermal annealing (RTA) or furnace annealing. The use of novel RTA is new in PLZT film processing and especially novel for post-processing of sputtered films and useful for studying the phase transformation, orientation in the films since it also minimizes outdiffusion of volatile species like Pb and the interdiffusion at the interface between substrate and the film. Alternatively, furnace annealing was also used to comprehensively study the microstructural, electrical, optical and electrooptic properties of the films and the relationships among the properties with respect to processing conditions.

Results from the deposition and subsequent annealing of thin films, initially compositional and structural, and then optical, electrical and electrooptic properties are presented in the forthcoming chapters, 4 and 5. The microstructural and compositional characteristics of films (chapter 4) were studied in conjunction with their relationships with the optical, dielectric and electrooptic properties (chapter 5).

References

1 K. Suu, A. Osawa, N. Tani, M. Ishikawa and K. Nakamura, T. Ozawa, K. Sameshima, A. Kamisawa and H. Takasu, "Lead content control of PLZT thin films prepared by rf magnetron sputtering," *Integ. Ferroelectrics*, **14**, 59, 1997.

2 S. K. Dey and R. Zuleeg, "Integrated sol-gel PZT thin-films on Pt, Si, and GaAs for non-volatile memory applications," *Integ. Ferroelectrics*, **108**, 37, 1990.

3 R. Moazzami, "Ferroelectric thin film technology for semiconductor memory," *Semicond. Sci. Technol.*, **10**, 375, 1995.

4 M. Kobune, S. Fuji, R. Takayama and A. Tomozawa, "Preparation and pyroelectric properties of (Pb, La)(Zr, Ti)O_3 (PLZT) thin films," *Jpn. J. Appl. Phys.*, **35**, 4980, 1996.

5 V. E. Wood, J. R. Busch, S. D. Ramamurthi and S. L. Swartz, "Guided-wave optical properties of sol-gel ferroelectric films," *J. Appl. Phys.*, **71**, 4557, 1992.

6 T. Kawaguchi, H. Adachi, K. Setsune, O. Yamazaki and K. Wasa, "PLZT thin-film waveguides," *Appl. Optics*, **23**, 2187, 1984.

7 G. Teowee, S. Motaker, T. J. Bukowski, J. M. Boulton, D. P. Birnie III and D. R. Uhlmann, "Optical losses in sol-gel derived lead lanthanum titanate waveguides," *Microelectronic Eng.*, **29**, 323, 1995.

8 H. Adachi, T. Mitsuyu, O. Yamazaki and K. Wasa, "Ferroelectric (Pb,La)(Zr,Ti)O3 epitaxial thin films on sapphire grown by rf-planar magnetron sputtering," *J. Appl. Phys.*, **60**, 736, 1986.

9 G. Griffel, S. Ruschin and N. Croitoru, "Properties of sputtered PLT thin films," *Appl. Phys. Lett.*, **54**, 1385, 1989.

10 G. Teowee, J. T. Simpson, T. Zhao, M. Mansuripur, J. M. Boulton and D. R. Uhlmann, "Electro-optic properties of sol-gel derived PZT and PLZT thin films," *Microelectronic Eng.*, **29**, 327, 1995.

11 G. H. Haertling, "Electrooptic characteristics of sol-gel PZT films on glass substrates," Proc. IEEE 4th Intl. Symp. Integ. Ferroelectrics, p.426, 1992.

12 D. H. Reitze, E. Haton, R. Ramesh, S. Etemad, D. E. Leaird and T. Sands, "Electro-optic properties of single crystalline ferroelectric thin films," *Appl. Phys. Lett.*, **63**, 596, 1993.

13 C. Bao and J. C. Diels, "Ultrafast nonlinear response in PLZT thin films with ultrashort pulses," *Optics Lett.*, **20**, 2186, 1995.

14 L. L. Boyer, A. Y. Wu, G. W. Metzger and J. R. McNeil, "Properties of ion deposited $Pb_{1-x}La_x(Zr_yTi_z)_{1-x/4}O_3$," *J. Vac. Sci. Tech.*, **A7**, 1199, 1989.

15 A. Mukherjee, S. R. J. Brueck and A. Y. Wu, "Electro-optic effects in thin-film lanthanum-doped lead zirconate titanate," *Optics Lett.*, **15**, 151, 1990.

16 W. G. Luo, A. L. Ding, R. T. Zhang, Y. H. Huang and M. Ge, "Deposition and properties of PLT thin films by magnetron sputtering from powder target," Proc. IEEE 8th Intl. Symp. Appl. Ferroelectrics, p. 19, 1992.

17 H. Adachi and K. Wasa, "Basic thin film process for perovskite ferroelectric materials," Mat. Res. Soc. Symp. Proc., vol. **200**, p. 103, 1990.

18 K. D. Preston and G. H. Haertling, "Comparison of electro-optic lead-lanthanum zirconate films on crystalline and glass substrates," *Appl. Phys. Lett.*, **60**, 2831, 1992.

19 J. F. Roeder, S. M. Bilodeau, P. C. Van Buskirk, V. H. Ozguz, J. Ma and S. H. Lee, "Liquid delivery CVD of PLZT thick films for electro-optic applications," Proc. IEEE 9th Intl. Symp. Appl. Ferroelectrics, p. 687, 1994.

20 A. Y. Wu, F. Wang, C. B. Juang, C. Bustamante, C. Y. Yeh, and J. C. Diels, "Electro-optic and nonlinear optical properties of $(Pb,La)(Zr,Ti)O_3$, $BaTiO_3$, $(Sr,Ba)Nb_2O_6$, $Ba_2NaNb_5O_{15}$ and beta-BaB_2O_4 thin films," Proc. 4th Intl. SAMPE Electronic Conf., p. 722, 1990.

21 S. Krishnakumar, V. H. Ozguz, C. Fan, C. Cozzolino, S. C. Esener and S. H. Lee, "Deposition and characterization of thin ferroelectric lead lanthanum zirconate titanate (PLZT) films on sapphire for spatial light modulators applications," *IEEE Ultra., Ferro., and Freq. Control*, **38**, 585, 1991.

22 G. Teowee, M. P. Mebes, C. D. Baertlein, E. L. Quackenbush, E. A. Kneer, J. M. Boulton and D. R. Uhlmann, "Compositional tailoring of the dielectric and ferroelectric properties of sol-gel derived PLZT thin films," *Integ. Ferroelectrics*, **10**, 131, 1995.

23 D. E. Dausch and G. H. Haertling, "The domain switching and structural characteristics of PLZT bulk ceramics and thin films chemically prepared from the same acetate precursor solutions," *J. Mater. Sci.*, **31**, 3409, 1996.

24 Y. S. Hwang, S. H. Paek, J. H. Lee, C. S. Park, J. S. Choi, J. K. Jung and Y. N. Kim, "Formation and characteristics of lead lanthanum zirconium titanate thin films formed by using the rf sputtering method," *J. Mater. Sci.:Mat. Electronics*, **7**, 309, 1996.

25 B. Jaber, D. Remiens, E. Cattan and B. Thierry, "Optimisation of the deposition and annealing parameters of paraelectric PLZT 28/0/100 thin films grown by rf magnetron sputtering," *Sensors and Actuators*, **A 51**, 1, 1995.

26 D. A. Tossell, N. M. Shorrocks, J. S. Obhi and R. W. Whatmore, "Growth of perovskite PLZT thin films by dual ion beam sputtering," *Ferroelectrics*, **134**, 297, 1992.

27 G. A. Petersen, Jr. and J. R. McNeil, "Effects of oxygen patrial pressure on lead content of PLZT thin films produced by excimer laser deposition," *Thin Solid Films*, **220**, 87, 1992.

28 H. F. Cheng, "Structural and electrical properties of excimer laser deposited PLZT thin films," *Appl. Surf. Sci.*, **92**, 378, 1996.

29 I. P. Llewellyn, R. A. Heinecke, K. L. Lewis, K. F. Dexter, "Pulsed plasma deposition of lead lanthanum zirconate titanate (PLZT) and lead lanthanum titanate (PLT)," *Ferroelectrics*, **133**, 85, 1992.

30 V. Trtik, M. Jelinek and E. B. Kluenkov, "A study of laser-deposited PZT, PLZT, PMN and YBCO thin films," *J. Phys. D: Appl. Phys.*, **27**, 1544, 1994.

31 Y. F. Kuo and T. Y. Tseng, "Preparation and characterization of PLZT thin films by sol-gel processing," *J. Mater. Sci.*, **31**, 6361, 1996.

32 M. Sedlar, L. Ziu and M. Sayer, "Sol-gel processing of PLZT thin films," *Integ. Ferroelectrics*, **6**, 129, 1995.

33 D. Chang, Y. Choh, W. Hsieh, P. Lin and T.Y. Tseng, "The role of drying-control chemical additives on the preparation of sol-gel derived PLZT thin films," *J. Mater. Sci.*, **28**, 6691, 1993.

34 G. H. Haertling, "An acetate process for bulk and thin film PLZT," Proc. IEEE 7th Intl. Symp. Appl. Ferroelectrics, p. 292, 1990.

35 A. T. Hunt, J. E. Abbey and H. G. Hornis, "PZT, PLZT, LSC and platinum thin films produced in the open atmosphere using combustion chemical vapor deposition," *Integ. Ferroelectrics*, **10**, 1, 1995.

36 M. Shimizu, H. Fujisawa and T. Shiosaki, "MOCVD of ferroelectric PLZT thin films and their properties," *Microelec. Eng.*, **29**, 173, 1995.

37 R. A. Roy, K. F. Etzold and J. J. Cuomo, "Ferroelectric film synthesis, past and present: A select review," Mat. Res. Soc. Symp. Proc., vol. **200**, p. 141 , 1990.

38 J. L. Vossen and W. Kern, Thin Film Processes, II-4, Academic Press, 1978.

39 D. J. Kester and R. Messier, "Micro-effects of resputtering due to negative ion bombardment of growing thin films," *J. Mater. Res.*, **8**, 1938, 1993.

4. This work : Growth, structural and microstructural characteristics of magnetron sputtered PLZT thin films

It was concluded from the earlier work that in order to optimize the optical, electrical and electrooptic properties of the films for electrooptic and other devices, it is necessary to characterize the film's microstructural characteristics and crystallinity with respect to the specific method and annealing conditions. The properties of PLZT films vary significantly depending on the deposition technique, processing/annealing conditions, substrates and hence microstructures and very little is known about the microstructural characteristics of PLZT 9/65/35 films and no work was published on microstructure of films on r-sapphire. In this chapter, we report on the microstructure of RF triode magnetron sputtered PLZT 9/65/35 films on r-sapphire as a function of post-deposition conditions using rapid thermal annealing and furnace annealing.

In this study, PLZT films were deposited at substrate temperatures below 500°C and annealed in the range 700° to 730°C for 1 min. to 20 min. for complete perovskite formation either by rapid thermal annealing (RTA) or furnace annealing (FA). The optical transparency was excellent with smooth surfaces in the stoichiometric films but reduced in the Pb-deficient films. The grain sizes in the films varied from 0.1 μm to 0.8 μm and 0.2 μm to 1.2 μm after RTA and FA respectively.

4.1 Experimental : Deposition of PLZT 9/65/35 thin films

The deposition system used in this study to grow PLZT thin films on several different substrates is shown in Figure 4-1. The system is an off-axis rf triode magnetron sputtering unit with two sources. Triode sputter-unit elements are shown schematically in the Figure 4-2. The basic elements consists of a thermal-electron emitting filament, an anode, a plasma-confining enclosure and a sputtering target. The filament is heated by a high-current AC power supply to a temperature sufficient for thermal electrons to boil off its surface, set to 36 Amp. in our experiments. These electrons are then attracted to an anode biased positively by a high-voltage DC power supply. Gas atoms, argon in this case, bled into the enclosure where they collide with the accelerated electrons generating ions and thus a self sustaining arc-type plasma will be initiated. Typically, this electron-enhanced plasma will be sustained at voltages of 50-70 volts and at currents up to 10 amperes. To initiate the sputtering process, a negative voltage DC or RF bias supply is applied to the target and plasma ions are attracted and accelerated towards the target surface.

As discussed in preceding chapter, the triode sputter systems can operate at low pressures, 1-2 mTorr, and reduce the amount of gas atoms embedded in the films, improving the density of films. If a low gas flow (with subsequent low chamber pressure) is desired, filament emission must be increased to enhance collision probabilites with the fewer gas atoms and thus sustain the plasma.

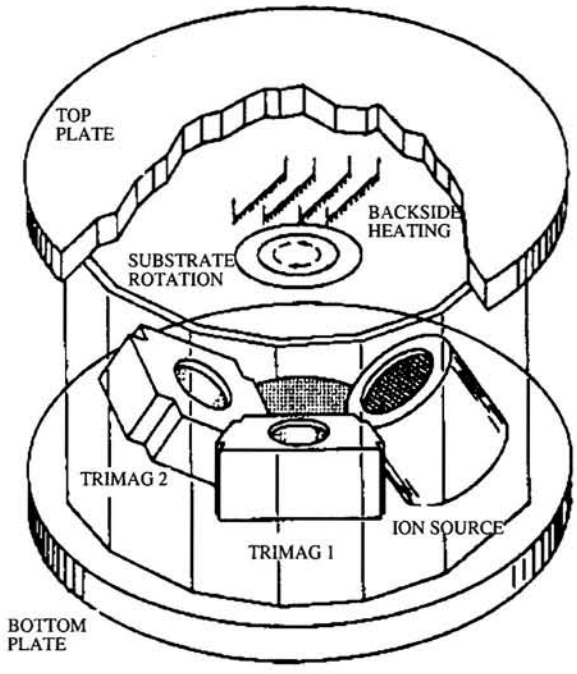


Figure 4-1 RF triode magnetron sputtering system.

Both mechanical and magnetic plasma confinement is used in this system. The source uses an enclosure that fits around the target periphery, which is electrically floating so that it will not be sputtered by the plasma ions and acting as a shield. Therefore, the targets of different sizes can be used provided that proper enclosure is available. The second type of selectively confinement of plasma discharge is due to magnets placed on both sides of the target. Magnetic fields will trap electrons emitted from cathode as an orbit around the field lines and electrons will undergo a drift motion $\vec{E}x\vec{B}$ in the direction perpendicular to both the electric and the magnetic fields. These electrons make large number of collisions, thus producing an intense plasma discharge.

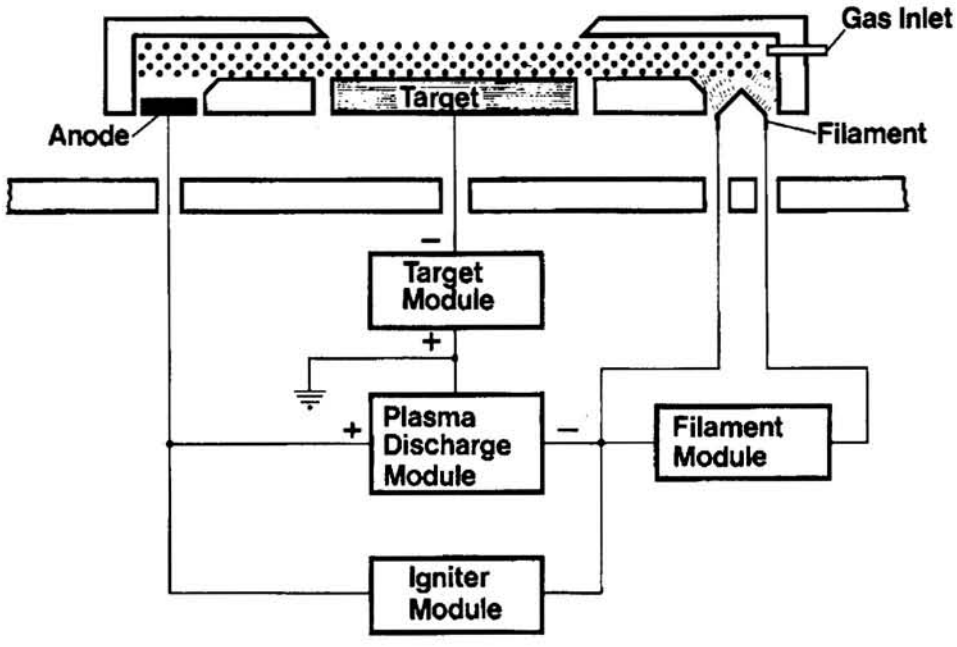


Figure 4-2 Triode sputtering unit.

Unlike the earlier work by Krishnakumar [1] and others who used sintered targets, in this study the PLZT sputtering targets of specified compositions were manufactured by hot-pressing by Balzers Materials (Hudson, NH). The target composition was nominally 9/65/35 with varying excess PbO, its size was 5.715 cm (2.25″) in diameter. The target was uniform in composition and of high density. High quality starting PLZT targets is important for repeatability and uniformity in the deposited films. Deposition results by loosely compacted powder or sintered targets are not very reproducible since the target stoichiometry can change due to Pb loss on the surface of low-density targets. The purity of hot-pressed PLZT targets are higher than the sintered targets used by other researchers, and the target lifetimes are also longer. This is due to repeated calcination and sintering cycles, which incrases the impurity contamination of the PLZT starting

powders from containers, ball mill and crucibles. More importantly, controlled addition of PbO into the targets is extremely difficult with the several-cycle pressureless-sintering technique. However, it is quite important to introduce excess Pb into the target to optimize deposition temperatures and to obtain stoichiometric films. It is possible to densify PLZT targets with controlled excess PbO by hot-pressing. After testing the sputtering from a stoichiometric PLZT target, we have utilized sputtering targets which had 20 at% PbO excess and 30 at% excess PbO. The composition of thin films from these targets are presented with respect to substrate temperature in the next film analysis section.

The target was bonded to a copper backing-plate using a conductive silver epoxy at room temperature. The target is water cooled during the magnetron source is on. Copper has a high thermal conductivity, 0.94 cal/sec-cm-°C and removes the excessive heat and conducts high bias voltages to the target. As mentioned earlier, the application of uniform magnetic fields over the target surface results in electrons undergoing a cycloidal path towards the target. Hence confinement of the plasma closer to the target leaves the film relatively unaffected by the rapidly changing dynamics of the plasma specifically from radiation damage. The argon plasma is sustained independent of rf voltage applied to the target and because of the reproducible plasma conditions, triode sputterer is suited to achieve high quality PLZT films. The target was periodically rotated 45° since the target erosion along cathode-anode direction was slightly faster than the rest of the target. The cryopump CTI-8 (CTI-Cryogenics, Mansfield, MA) used in the system for high vacuum

sustain pressures down to 2 mTorr for such a large system with a heavy argon load more than 100 cc/min. The substrate-target distance and the azimuth angle (41°) of the sources was optimized by simulation for maximum film uniformity from 12.7 cm (5″) targets. The system parameters and some typical sputtering conditions were listed in Table 4-1. The sapphire substrates were epitaxially polished on one side and optically polished the other side (Union Carbide, Crystal Products, Washougal, WA). The sapphire or silicon substrates were mounted on a molybdenum substrate holder block with molten indium. The substrate holder was rotated for the film uniformity and no dc voltage was applied to the substrate. The moly-block was heated by halogen lamps on the back side. The substrate temperature was monitored by chromel-alumel thermocouple attached to moly-block holder.

Table 4-1 Sputtering conditions.

Target Diameter	57 mm
Target-Substrate Distance	250 mm
RF Power	200 W
Sputtering Gas	Argon
Chamber Pressure	0.55 Pa
Substrate Temperature	210 - 500 °C
Growth Rate	1.1 nm/min

PLZT films were first deposited at a range of substrate temperatures between 210 to 600 °C and then analyzed by x-ray diffraction (XRD) and Rutherford Backscattering Spectrometry (RBS) to check the crystal structure and the composition respectively. For the films deposited at low substrate temperatures (below 300 °C), an amorphous phase was detected and higher temperatures resulted in crystallization of PLZT into pyrochlore, perovskite or a mixture of both. In order to get crystalline single-phase perovskite, substrate temperatures of 600 °C are required. However, at such high substrate temperatures significant Pb loss takes place in sputtered films. Therefore, the deposition has to be carried out at lower temperatures. The color of the films was light yellow on sapphire in the as-deposited state. The films were then annealed to fully transform them to desired perovskite phase, which also makes films fully transparent and colorless. Post-deposition annealing improves the optical, electrical and electro-optic properties dramatically. Two different types of annealing approaches were used to achieve high quality, single phase PLZT 9/65/35 thin films: 1) rapid thermal annealing and 2) furnace annealing in PbO/O_2 ambient. A generalized summary of the approach is given in Figure 4-3.

Rapid thermal annealing (RTA) is increasingly used in semiconductor submicron device processing (Si or GaAs-based) for various steps [2]. Previous investigations have indicated that RTA processing based on either infrared or visible light (near UV), with usual heating times in the 10-300 s range, can reduce the thermal budget significantly in semiconductor processing and supply enough thermal energy to activate the surface of the

wafer for numerous processes like recrystallization, junction formation, diffusion, nitridation, oxidation and recovery of lattice distortion. The RTA used in ferroelectric thin films is known to produce fine grained ceramic films and to reduce the reaction between the film and the substrate [2,3]. Since the annealing times are very short, serious diffusion with the underlying semiconductor or the electrode and also the elemental loss at the surface can be minimized.

The RTA processor used in this study included a 2.54 cm (1″) quartz tube surrounded by banks of tungsten halogen lamps for fast heating. The thin-film sample was placed on a 25mmx13mm graphite (or quartz) plate holder with 1 mm walls on top to contain the sample and the silicon wafer underneath. A chromel-alumel thermocouple was extended through an quartz encasing tube to be in contact with the back of silicon wafer to monitor the temperature. The graphite holder was observed to be more consistent in temperature calibration measurements than the quartz holder probably due to much higher radiation absorption and slower heating of quartz due to its lower absorptivity. However, the thin films had to be covered by sapphire wafers to protect them from oxidizing products of graphite in nitrogen or oxygen environments.

Furnace annealing was carried out in 2.54 cm (1″) quartz tubes in oxygen with PbO ambient provided by PLZT ceramic of the same composition with excess PbO located near the thin-film sample. Alternatively, the thin films were sealed in quartz tubes (13 mm diameter) with compensated PbO source. Furnace annealing has been a common process since it is convenient and the wafers are in thermal equilibrium. The temperature

distribution across the wafers is very uniform in this case as compared to RTA process where faster heating and cooling can induce higher residual stresses. In furnace annealing, PLZT films need to be protected from evaporation of Pb due to longer holding time. As an alternative to PbO-ambient annealing, the as-deposited films were coated by protective SiO_2 or Si_3N_4 layer on top by plasma enhanced chemical vapor deposition and then furnace annealed in flowing oxygen and subsequently etched. However, this method caused an interaction of SiO_2 or Si_3N_4 with the underlying PLZT through diffusion as determined by RBS. Therefore, the former annealing process with PbO ambient was used in furnace annealing the PLZT films in this study.

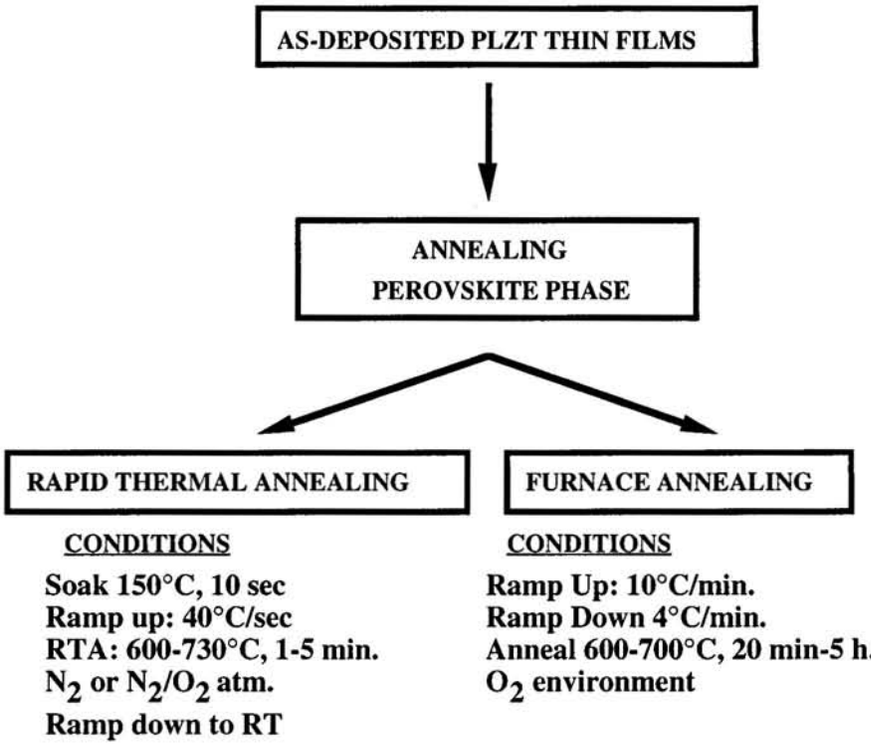


Figure 4-3 The chart describing basic deposition and annealing schedule of PLZT thin films.

In general, the as-deposited ferroelectric films are amorphous or a mixture of crystalline pyrochlore and perovskite phases and post-deposition annealing is necessary to transform the film into desired perovskite phase. The pyrochlore is reported to be present as an intermediate phase present from 300°C-600°C, and transforms to perovskite at higher temperature given enough time [1,4]. Although some efforts have been reported in the study of this transformation kinetics in PZT thin films, no such investigations have been done on PLZT 9/65/35 thin films. Isothermal formation kinetics of perovskite powder PLZT 8/65/35 from nitrate solutions has been studied [5] and it was inferred from the experimental data that the mechanism of random nucleation prevailed, with nucleation as the rate-determining step. The activation energy of crystallization of these chemically prepared PLZT powders was found to be 297 kJ/mol. In only one study reported on thin-film PLZT, the peak intensity (111) of sol-gel derived PLZT 8/65/35 on Pt/Si has been determined to show a $t^{1/2}$ dependence as a function of heat treatment temperature previously [6]. In this work we studied the pyrochlore-perovskite transformation in thin-film PLZT 9/65/35 on sapphire by rapid thermal annealing, which is presented in the following section.

4.2 Phase transformation kinetics

An understanding of crystallization of perovskite phase in PLZT thin films is important for the development of better ferroelectric, dielectric and electrooptic properties as the single-phase material with a controlled microstructure is required for better device performance. Whatever the deposition process, metallorganic

decomposition, sol-gel, laser ablation or sputtering, often a post-deposition annealing is necessary for better electrical or electrooptic properties. This is because an intermediate phase(s) forms at lower processing temperatures which is usually termed as pyrochlore phase with cubic fluorite structure with a lattice constant around 10.8 Å. This phase is nonferroelectric and has very low dielectric constant, and transforms to perovskite phase fully or partially at higher deposition/annealing temperatures. In our work, the pyrochlore phase found was $La_2Zr_2O_7$ at deposition temperatures below 450°C and also in annealed PLZT 9/65/35 thin films. The annealing was done by RTA in the range 475°C to 720°C, and transformation to perovskite above 600°C is studied in the present work by x-ray diffraction (XRD) and scanning electron microscopy (SEM).

The crystallization of amorphous PLZT into pyrochlore and perovskite phases take place simultaneously in this work. Therefore, generalized Avrami analysis for combined nucleation and growth can be applied, where the linear growth rate u of an unimpinged particle of β growing into α phase is independent of time. At annealing temperatures above 575°C, the incubation time for the nucleation of perovskite phase is less than 15 seconds by RTA process. It is reasonable to assume that shortly after the incubation period nuclei will grow isotropically in three dimensions until the thickness of the particles is equal to the thickness of the film. The thickness of the films studied here is 400 nm. Further grain growth involves mass transport from the lateral directions parallel to the plane of the substrate, and the growth rate in the direction perpendicular to the

substrate plane becomes very small and will lead to a two-dimensional growth. The final grain of this thin plate may resemble a flat disk if the lateral growth is isotropic.

The kinetics of transformations where nucleation and growth occur simultaneously is expressed by Burke and Turnbull [7] and $V_t/V_o = X_t$, volume fraction transformed to perovskite can be written as

$$x_t = 1 - \exp\left(-\int_0^t V_p dN_c \right) \tag{4-1}$$

where V_p is the volume of the particle and N_c is the number of nuclei per unit volume. If u is a vector quantity, then the volume of the particle can be written as $Vp = g u_x u_y u_z (t-t')^3$, where u_i is the growth rate in the i direction and the g is the shape factor and a linear dimension of the particle at time t where $t > t'$ will be given by $u(t-t')$. In this work, the particle shape is assumed to be cylindrical thin plate with radius $u(t-t')$ and thickness δ. The volume of the particle then is $V_p = \pi u^2 (t-t')^2 \delta$ and the nucleation frequency $I = dN_c/dt = dN/\delta dt$ where N is the number of nuclei per unit area as measured from the electron micrographs and δ is the thickness of the film. It can be written that

$$x_t = 1 - \exp - \left[-\int_0^t \pi u^2 (t - t')\delta\left(\frac{N}{\delta}\right) dt' \right] \tag{4-2}$$

$$x_t = 1 - \exp\left[-\left(\frac{\pi}{3}\right) u^2 N t^3 \right] \tag{4-3}$$

Johnson-Mehl equation (2-17) is derived assuming that u and I are independent of time [7]. In this study, the growth rate is relatively constant but it showed decreasing trend at the later stages of growth. Most likely, the I was not independent of time

throughout the temperature range we studied, 475°C-720°C, but a function of time due to some preferred nucleation sites due to interface between the film and the substrate and existing grain boundaries. The exponential decay of *I* was accounted for in Avrami's model. The nucleation and growth process can be expressed as [7]:

$$x_t = 1 - \exp(-kt^n) \qquad (4\text{-}4)$$

where k is the Arrhenius type reaction-rate constant related nucleation and growth and n is the time exponent (Avrami exponent) which is temperature independent and related to the mechanism of nucleation and growth and geometry of particle. Taking logarithms and rearranging Eq. 4-4 results in

$$\ln \ln (1/1-x_t) = \ln k + n \ln t \qquad (4\text{-}5)$$

The exponent n and rate constant k can be found from the plot of $\ln \ln (1/1-x_t)$ as a function of ln t. The transformed perovskite (pe %) can be deduced from the integrated intensities of XRD peaks of perovskite (I_{pe}) and pyrochlore (I_{py}) using the intensity ratio, $I^{(110)}_{pe}/ I^{(222)}_{py} + I^{(110)}_{pe}$. The slope in Eq. 4-5 is n and the y-axis intercept gives the ln k. This plot is shown in Figure 4-4, for temperatures 600°, 625°C, 650°C and 720°C. The constant n values are 0.83 at 600°C, 1.35 at 625°C, 0.57 at 650°C and 0.15 at 720°C. The value of reaction order (Avrami exponent) n is below 2.0 suggests that the growth of perovskite phase is possibly a diffusion-controlled process. The scatter in the data is thought to result from a transformation process to perovskite phase from both pyrochlore and amorphous phases rather than from pyrochlore alone. This finding ($n < 2$) is in agreement with the reported reaction order exponent n = 1 for PLZT 8/65/35

powder, which was obtained from the isothermal crystallization data from temperatures of 409°C to 483°C [5]. In the powder case, a random nucleation with nucleation as the rate-determining step was inferred. In addition, a diffusion-controlled reaction was suggested for the perovskite formation of sol-gel PLZT 8/65/35 films on platinized silicon substrates [6]. For the transformation from $La_2Zr_2O_7$ to perovskite phase the exponent less than 2 can be explained in terms of a diffusional process.

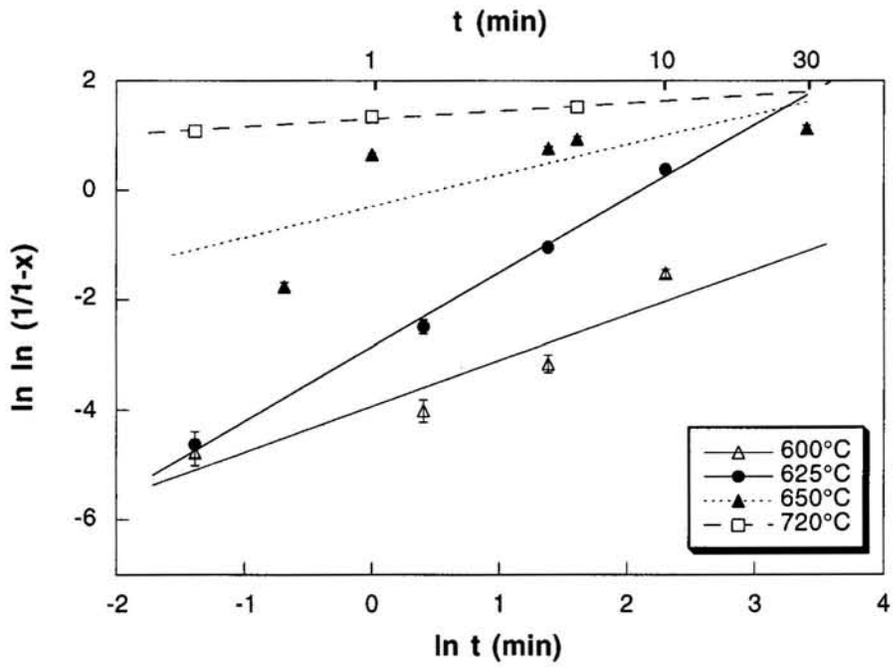


Figure 4-4 Avrami plots of ln ln $(1/1-x_t)$ against ln t for four different annealing temperatures.

The temperature dependence of effective reaction-rate constant k in Eq. 4-5 demonstrates a simple Arrhenius behavior and expressed as

$$k = \nu \exp [- E_a/(RT)] \qquad (4\text{-}6)$$

where ν is the frequency factor, E_a the effective activation energy for the formation of perovskite phase and R the gas constant. According to the transition-state theory, ν can be identified with the vibration (parallel to the reaction coordinate) frequency of the atom in the transition state incorporating into a new growing phase.

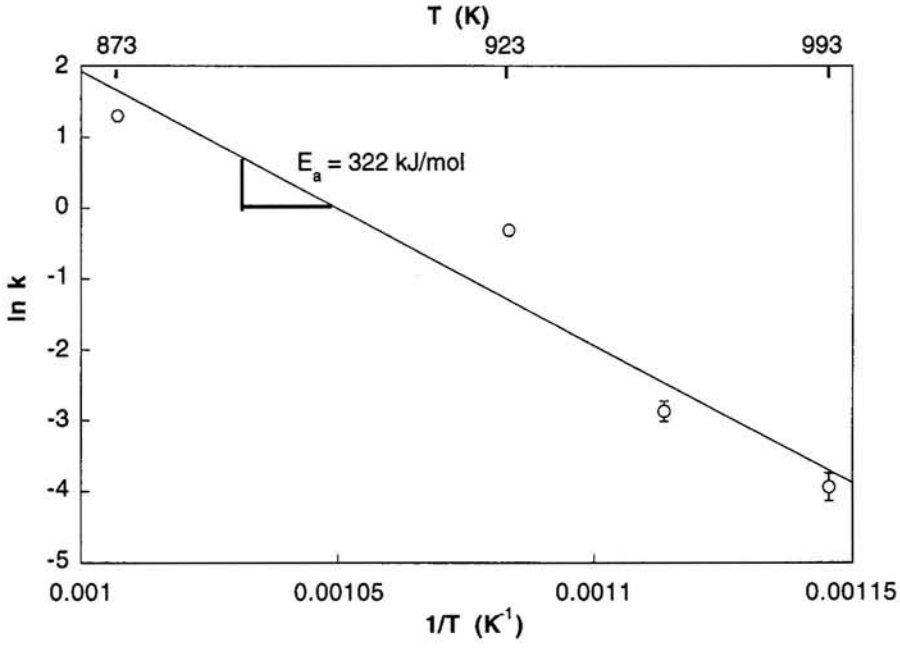


Figure 4-5 Arrhenius plot of rate constant k of first-order equation.

Figure 4-5 plots the ln k values obtained from Eq. 4-5 versus the reciprocal of absolute temperature, for annealing temperatures 600°C, 625°C, 650°C and 720°C. The slope of the line from the linear regression analysis reveals an activation energy for the formation of perovskite phase in PLZT thin films, E_a = 322 kJ/mol. The process is near completion at 720°C and growth rate is gradually decreasing at this temperature and adding the data for this sample reduces the calculated activation energy. This value of activation energy (322 kJ/mol) for PLZT 9/65/35 films on sapphire is higher than the activation energy reported for PLZT 8/65/35 powder, 297 kJ/mol. The strain-free powders are not clamped like the thin films on substrates. The critical temperatures for pyrochlore-perovskite transformation were usually lower for lead zirconate titanate (PZT), lead titanate (PTO) thin films and activation energies of metallo-organic, sol-gel derived or sputtered films reported ranged from 26 kJ/mole [8], 295 kJ/mole [9], 494 kJ/mole [10] and to 660 kJ/mole [11] for PZT films usually with n = 2.0 and 404 kJ/mole for $Ba_{0.6}Sr_{0.4}TiO_3$ powders, with n = 1.0 [12].

The frequency factor can also be obtained from linear regression analysis of the data and a value of $\nu = 4.3 \times 10^{17}$ min^{-1} was found, with a correlation coefficient of 0.970 indicating a good fit. In the case of the sol-gel derived $PbTiO_3$ powder, an activation energy of 265 kJ/mol and a value of $\nu = 1.0 \times 10^{17}$ min^{-1} were reported [12]. This frequency factor is similar to the value found in this work.

4.3 Thin Film Characteristics

4.3.1 Composition and crystal structure

The composition of the as-deposited and annealed thin films was examined by Rutherford backscattering spectrometry (RBS) and by electron microprobe analysis and Auger electron spectroscopy in some cases to correlate the results of RBS (2.3 MeV He^{++} ion beam). Typical energy resolution values are 10-20 keV for FWHM, which enables the technique to resolve atomic mass differences between Pb, La, Zr, Ti and oxygen. The analysis is straightforward for PLZT films on sapphire or silicon substrates but difficult to resolve the Pb content when the film is on Pt due to their similar atomic weights, 207 and 195, respectively. The RBS spectra are simulated (RUMP® simulation program) for a given stoichiometry and fitted to the experimental measurement to obtain the final composition of the film.

The sputtered film composition as a function of substrate temperature is shown in Figure 4-6. The volatility of Pb was a significant feature in PLZT sputter deposition as is observed from the plot. The lead depletion at very low temperatures is probably due to the geometry of the system as well as the type of sputter sources selected for deposition. The large source to substrate distance contributed to the low arrival rates of Pb as well as causing lower deposition rates. However, the choice was useful in obtaining films with good uniformity. It should be noted that two multicomponent hot-pressed and compensated PLZT targets were used that contained 20 at% and 30 at% excess PbO. It is known that powder multicomponent PLZT oxide targets [13] or elemental targets [1] give

irreproducible results with compositional nonuniformities. In our as-deposited films, the Zr/Ti atomic ratio was relatively constant in the substrate temperature regime, analyzed by RBS. The sputtering gas was 100% inert argon and no oxygen was added as the reactive ambient caused compositional shifts in the target as well as on the films.

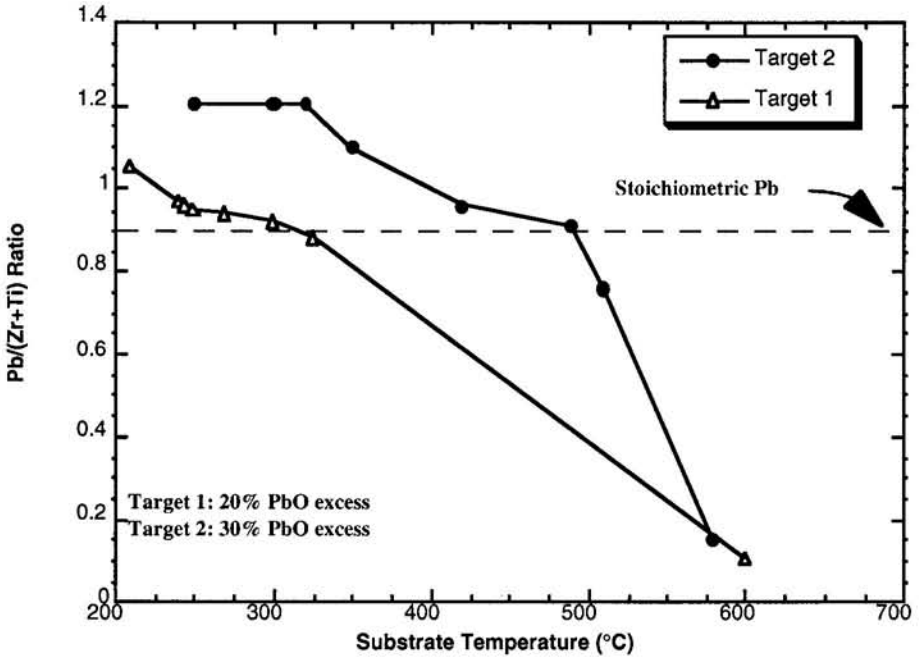


Figure 4-6 Film lead content as a function of substrate temperature using hot-pressed single PLZT oxide targets with excess PbO.

The films deposited at temperatures between 300°C and 450°C show excess Pb content and loss of Pb/PbO is noticeable above 450°C, and is depleted dramatically at 600°C. The excess Pb in the films deposited at low substrate temperatures in the range 6 % Pb excess to 29 % Pb excess was confirmed by RBS. Figure 4-7 shows a stoichiometric PLZT 9/65/35 film on sapphire which was obtained at temperatures just below 500°C

and rapid thermally annealed at 700°C for 3 min. RBS spectrum of a furnace annealed (700°C, 1 h) stoichiometric PLZT 9/65/35 film on r-sapphire is illustrated in Figure 4-8.

The PLZT films were annealed in either PbO-O_2 atmosphere in a tube furnace or rapid thermally annealed in N_2 or N_2/O_2 atmosphere. The lead contents were relatively constant at RTA temperatures 650° to 730°C for less than 3 min and longer hold-times induced only a little Pb loss, regardless whether the ambient was N_2 or O_2. It was seen that furnace annealing in O_2 atmosphere containing PbO-PLZT specimens/powders was effective in preventing Pb and O_2 loss. Pb and O_2 depletion were found in the surface region (5 nm) of sol-gel PZT films on Pt/Si annealed at 650°C for 15 min in air ($p(O_2)$ = 0.2 atm) or oxygen ($p(O_2)$ = 1 atm) and the formation of these depletion layers were attributed mainly to the volatilization of PbO [14]. A large quantity of vacancies were created when the films were annealed at low oxygen partial pressure (for example, 10^{-3} to $2x10^{-5}$ atm). An additional phase on the surface of sol-gel PLZT layers was also attributed to evaporative loss of PbO and an additional PbO cover-coat seemed to reduce this problem [6].

The vapor pressure for PbO(s) at 650° to 700°C is of the order of 10^{-8} atm. This value is much less than the vapor pressure at 1000°C ($3x10^{-4}$ atm), where evaporative loss is significant for bulk ceramics, however, the surface area to volume ratios are significantly larger for thin layers, typically 10^3 to 10^4 times greater than for bulk ceramic powder compacts. PbO was not observed to reduce to Pb metal on PZT or PLZT thin

layers but rather evaporate as Pb and O from the surface as measured by thermogravimetric PbO weight losses.

The deposition rate decreased with increasing chamber pressure (Ar gas) and with increasing substrate temperature due to depletion of lead from the films. The power density increase from 200 W to 300 W caused slight 2 at % Zr enrichment in the films and a decrease in rf-power to 100-150 W decreased the deposition rate.

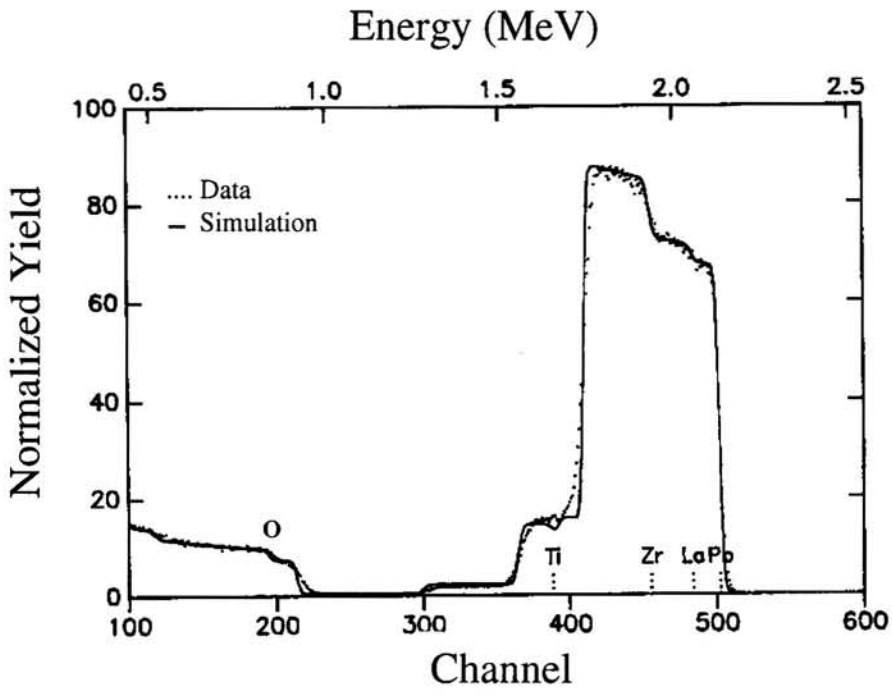


Figure 4-7 RBS spectrum of stoichiometric PLZT 9/65/35 film on sapphire. The post-RTA film thickness is 0.44 μm.

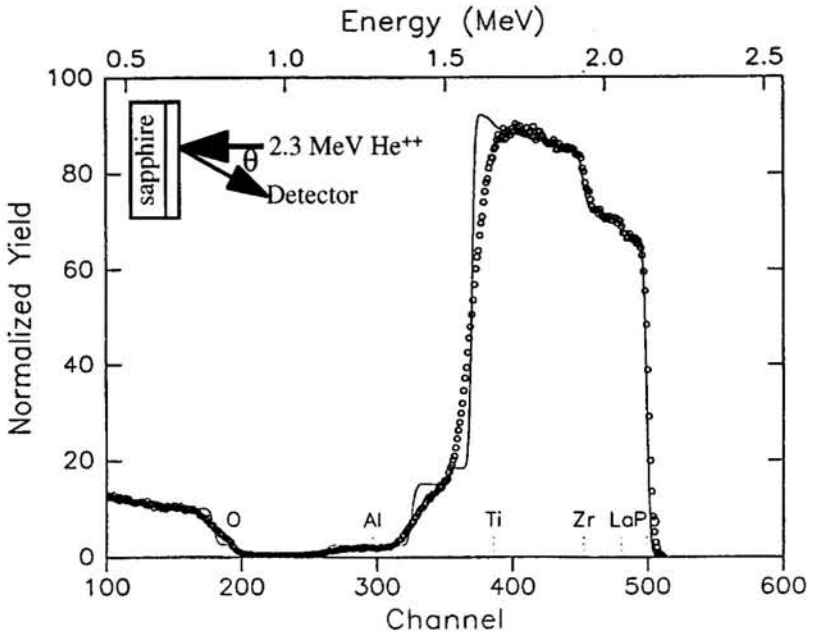


Figure 4-8 RBS spectrum of stoichiometric PLZT 9/65/35 film on sapphire (700°C for 1 h).

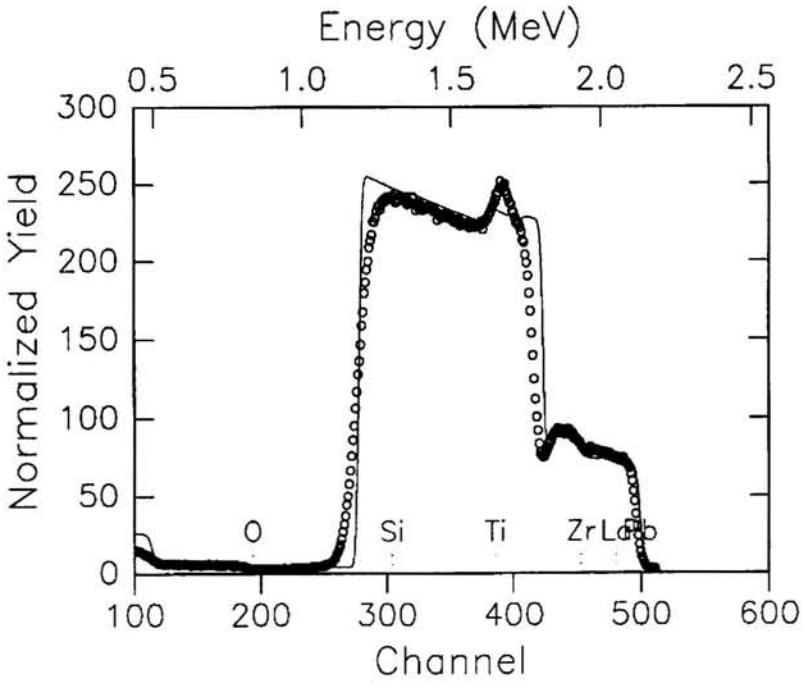


Figure 4-9 RBS spectra of as-deposited PLZT films on Pt/Si substrate.

As it was noted in PZT films, in addition to Pb loss by evaporation, Pb can react with the Pt electrode or the Ti adhesion layer which are used in integrated structures [6]. Figure 4-9 shows that there is probably some compositional nonuniformity across the PLZT thin film, likely to be at the interface, on as-deposited on 400 nm-Pt/Si. The small deviation of data (circles) from simulation (solid line) at channel ~ 420 indicates that there is probably a reaction at the interface. The film was Pb-deficient as compared to films on sapphire with similar processing conditions. Further chemical elemental analysis by Auger spectroscopy or other techniques is necessary to find out the concentration profile across the film. Crystal structures formed in the as-deposited or annealed films were determined by x-ray diffraction. PLZT films deposited on sapphire at substrate temperatures below 300 °C showed an amorphous phase (Figure 4-10) whichcrystallized into the perovskite phase after RTA processing at 730 °C for 3 min, as shown in Figure 4-11 for deposition temperatures of (a) 245°, (b) 250° and (b) 260°C). The peak denoted as 'o' belongs to pyrochlore.

It is interesting to note that the PLZT films were oriented in (110) direction and they had tetragonal lattice structure since both (101) and (110) reflections were present. The tetragonal distortion from cubic lattice was very small and the calculated lattice constants were a = 0.4086 nm and c = 0.4109 nm. It is possible to circumvent the formation of pyrochlore by rapid thermal annealing which also yielded transparent films with smooth surfaces. The films had (110) orientation and the degree of orientation (PO) was 96% and 88% for the films annealed at 730°C and 700°C respectively. The PO(110) was estimated

from the integrated intensities ($I^{(hkl)}$) of (110) and (100) reflections, using the equation PO = $I^{(110)}/(I^{(110)}+I^{(100)})$.

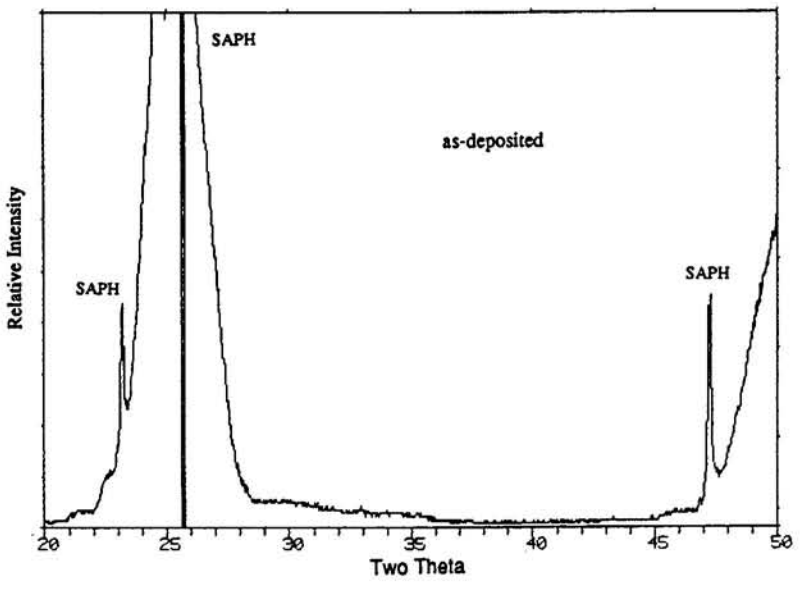


Figure 4-10 X-ray diffraction pattern of as-deposited PLZT thin film on sapphire indicating an amorphous phase.

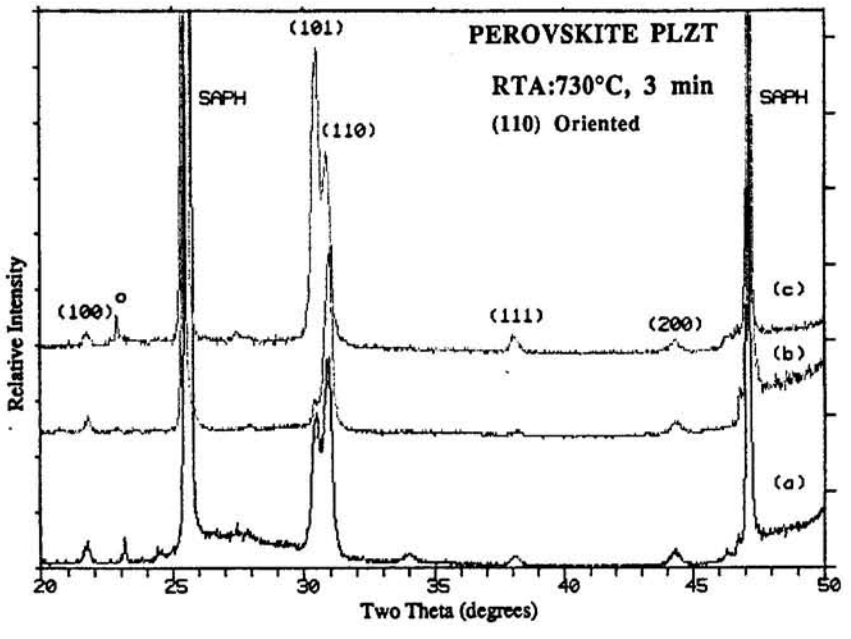


Figure 4-11 XRD patterns of PLZT/sapphire showing the perovskite phase (indexed) after RTA treatment at 730°C for 3 min.

The progression of pyrochlore to perovskite conversion is seen in Figure 4-12 as the RTA temperature was increased from 550° to 650°C for 2 min in a flowing N_2/O_2 atmosphere. The pyrochlore forms at 600°C annealing and the perovskite phase forms at slightly higher tempreatures. The intermediate phases (pyrochlore) formed at deposition temperatures below 420°C seemed to be $La_2Zr_2O_7$ (JCPDS Index # 17-450) and above 450°C the phase is assumed to be O- or Pb-deficient compounds, $Pb_2La_y(Zr, Ti)_2O_{7-x}$ or possibly $PbTi_2O_7$, and this phase could not be directly indexed to existing JCPDS files. The peaks denoted as 'p' belong to pyrochlore phase.

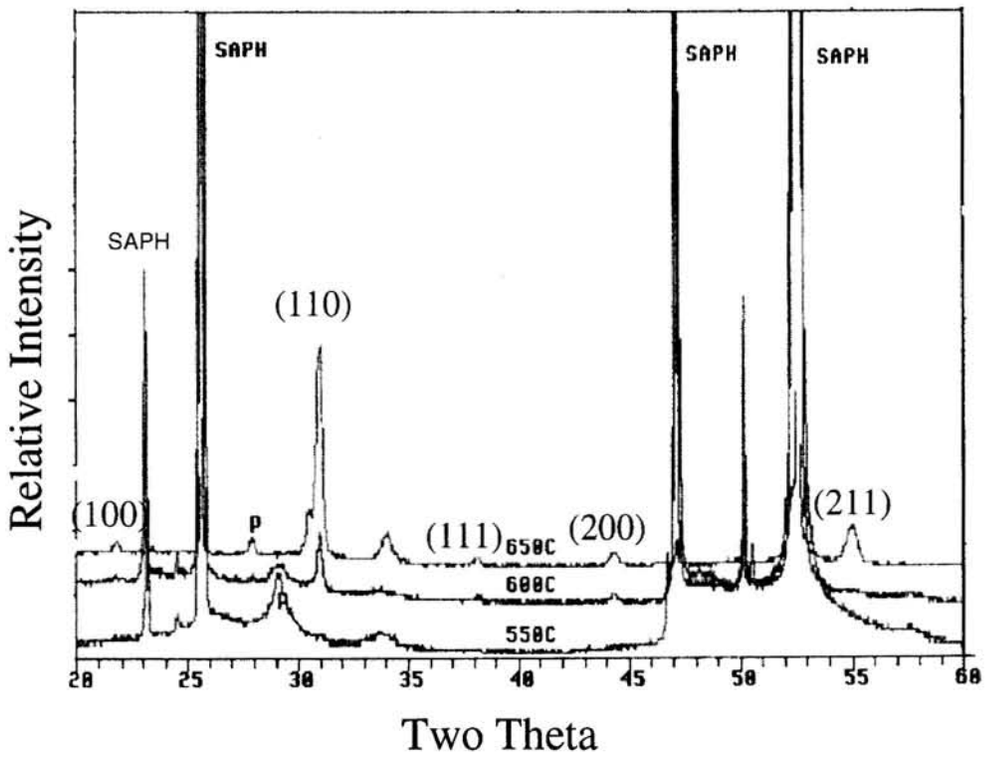


Figure 4-12 The transformation of pyrochlore/amorphous PLZT to perovskite as a function of RTA temperature. The conditions: 2 min soak, N_2:O_2 atmosphere.

Amorphous or pyrochlore phases present in the PLZT films on sapphire were characterized by a yellowish color and the single-phase perovskite phase films were transparent and colorless. The films have to be cooled slowly after the RTA soak especially above 650°C since cracking can occur due to residual stresses caused by the thermal expansion mismatch between the film and the sapphire substrate. The results from XRD analysis of the films deposited as pyrochlore at elevated temperatures after annealing (RTA in N_2) for soak time from 11/2 min sec to 10 min are presented in Figure 4-13 625°C-annealing. The perovskite peak at $2\theta \sim 30.80°$ appears only after 30 min annealing at 550°C, however it appears after 4 min at 600°C and 1 1/2 min at 625°C. The crystallite sizes of perovskite and pyrochlore were obtained using the measurements of the FWHM (full width half-maximum) from XRD peaks, perovskite (110) at ~ 30.80° (2θ), pyrochlore peaks at ~ 29° or 34°. The FWHM was determined by using a program called Profile Fitting (Scintag, USA).

The growth rate and the crystallite size can be inferred from XRD peak broadening measurements. The crystallite size increased linearly during early stages of annealing and it can be calculated using Scherrer formula [15].

$$D = 0.9 \lambda /(B \cos \theta) \qquad (2\text{-}22)$$

where D is the crystallite size, λ the wavelength of x-ray source (CuKα radiation in this case), θ the diffracting angle and corrected broadening, B, of the diffraction line at FWHM is $B^2=B_M^2-B_S^2$, where B_M and B_S are the measured line widths at half-peak intensity

(PLZT thin film) and the standard (quartz or bulk PLZT) respectively. Pyrochlore cystallite size of as-deposited PLZT film (T_{dep} = 300°C) is determined to be around 30 nm, by XRD and SEM and perovskite crystallite size is larger, 60 nm, for as-deposited thin film (T_{dep} = 460°C). The results for perovskite formation based on (110) reflection is given in Table 4-2, at RTA temperatures 550°C and 650°C for various annealing soak-times. The crystallite size increased as the holding time increased at a given annealing temperature. The films after RTA result in uniform and smooth surface but small grain size.

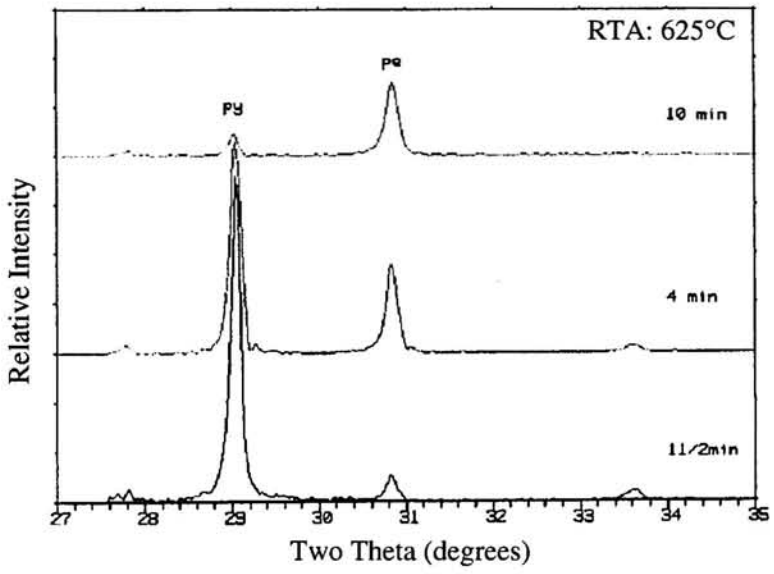


Figure 4-13 X-ray diffraction patterns of PLZT films rapid thermally annealed 625°C, soaked from 11/2 min. up to 10 min.

Furnace annealing at high temperatures above 500°C without the PbO + O_2 atmosphere causes severe Pb depletion and perovskite phase cannot be obtained from

severely nonstoichiometric films. PLZT films deposited at substrate temperatures of 480 °C showed negligible Pb-deficiency and a combination of perovskite and pyrochlore phase resulted. The only strong perovskite peak was of (200) reflection. These films were annealed at 700°C only for 15 min to 1 h to suppress the pyrochlore phase and to achieve (110) oriented films with nearly complete perovskite phase. One such film on sapphire is illustrated (FA at 700°C for 20 min) in Figure 4-14. The PLZT 9/65/35 film on r-sapphire which were furnace annealed showed a cubic structure, with a lattice constant of 0.409 nm.

Table 4-2 Annealing temperature and the FWHM of perovskite phase.

RTA time	550°C, FWHM	650°C, FWHM
15 sec	0.532	0.150
60 sec	0.500	0.145
5 min	0.208	0.142
30 min	0.148	0.083

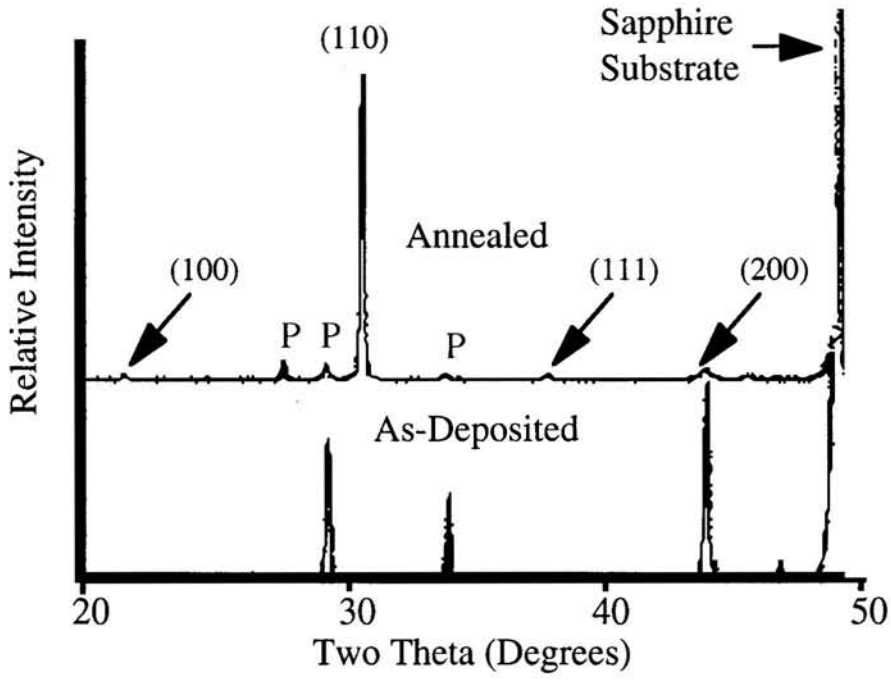


Figure 4-14 XRD pattern of PLZT film deposited at 480°C and then furnace annealed.

4.3.2 Microstructure

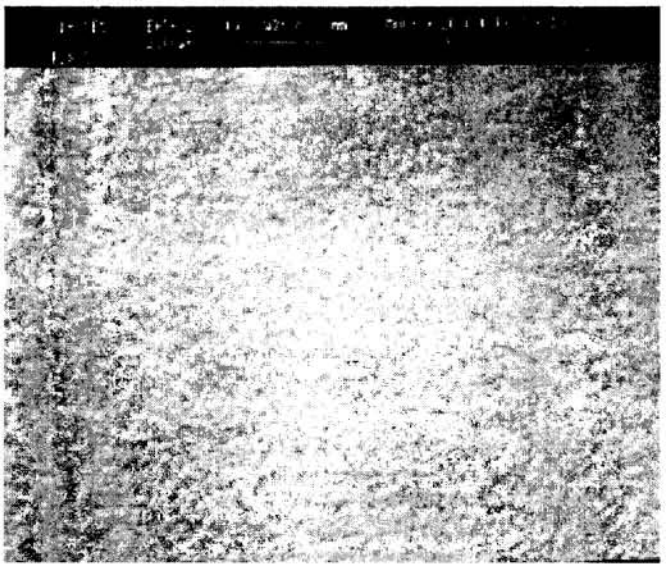
Bulk PLZT 9/65/35 has a grain size ranging from 2 to 8 μm depending on the processing and hot-pressing conditions. However, thin films of PLZT are known to possess smaller grain sizes for various deposition methods and grain sizes reported range from 0.5 to 1 μm for uniform microstructures on a variety of substrates including Ag foil, Pt/Si,SnO_2-coated PLZT, MgO, sapphire [16,19]. The substrate had a substantial effect on the microstructure of acetate-derived PLZT thin films [17]. Very little work was done on the microstructural development of PLZT 9/65/35 thin films. PLZT films with 9/65/35 compositions magnetron sputtered on (0001) sapphire substrates showed (111)

orientation [18] and the size of the crystallite of the surface was about 200 nm in diameter [19]. It was reported by Wasa et al that a buffer layer of PLT between the film and the substrate enhanced the epitaxial growth of PLZT (111) films [19]. The epitaxial relations were previously reported as (111)PLZT//(0001) sapphire and [110]//[1010] sapphire [19].

A strong correlation exists between microstructural development and the processing conditions of PLZT films on r-sapphire. At lower deposition temperatures, the films contain an amorphous phase and a nanocrystalline phase exhibiting smooth and uniform surfaces on optical or SEM (scanning electron microscopy) micrographs. Grains of rather circular (or hexagonal) shapes form in microstructures after high temperature post-annealing, which represent the perovskite phase. At intermediate temperatures, a smooth pyrochlore/amorphous featureless matrix coexists with newly nucleating round clusters of perovskite crystallites. The pyrochlore phase that forms at deposition temperatures of 300°C usually has a crystallite size of 20-30 nm while the perovskite crystallite size is larger, 60 nm, at its first nucleation, usually around T_{dep} = 480°C. The films deposited on single-crystal r-plane sapphire showed smoother surfaces than that on platinized silicon substrates, as seen in SEM micrographs of PLZT films in Figure 4-15 (a) on r-sapphire and (b) on Pt/Si. This is probably due to the epitaxially-polished surface of sapphire versus rougher surface of sputtered platinum on silicon, and perhaps aided by the chemical film-substrate interactions in the case of Pt/Si. The film roughness of as-deposited and annealed PLZT films on both substrates is illustrated by AFM (Atomic

Force Microscopy) images in Figure 4-16 (a) as-deposited PLZT on r-sapphire, (b) annealed film on r-sapphire and as-deposited film on Pt/Si (Figure 4-17). The rapid thermal annealing in nitrogen ambient resulted in smoother surface microstructures than that of oxygen.

(a)



(b)

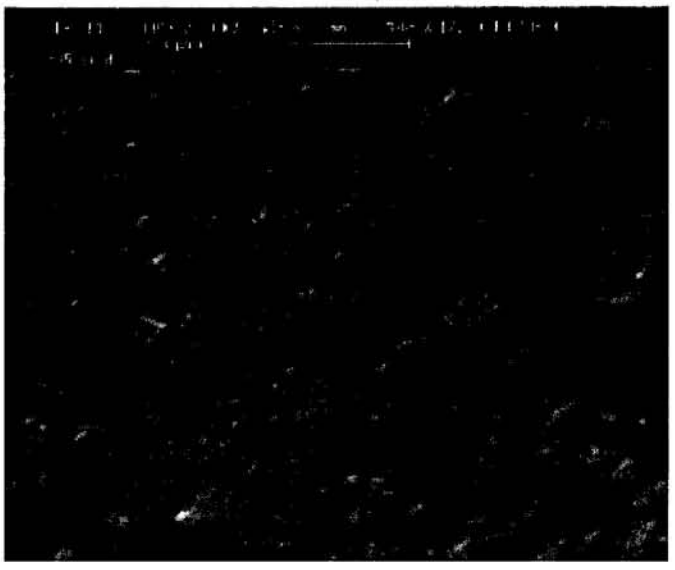


Figure 4-15 SEM micrograph of as-deposited PLZT thin film on r-sapphire (a) and Pt/Si (b).

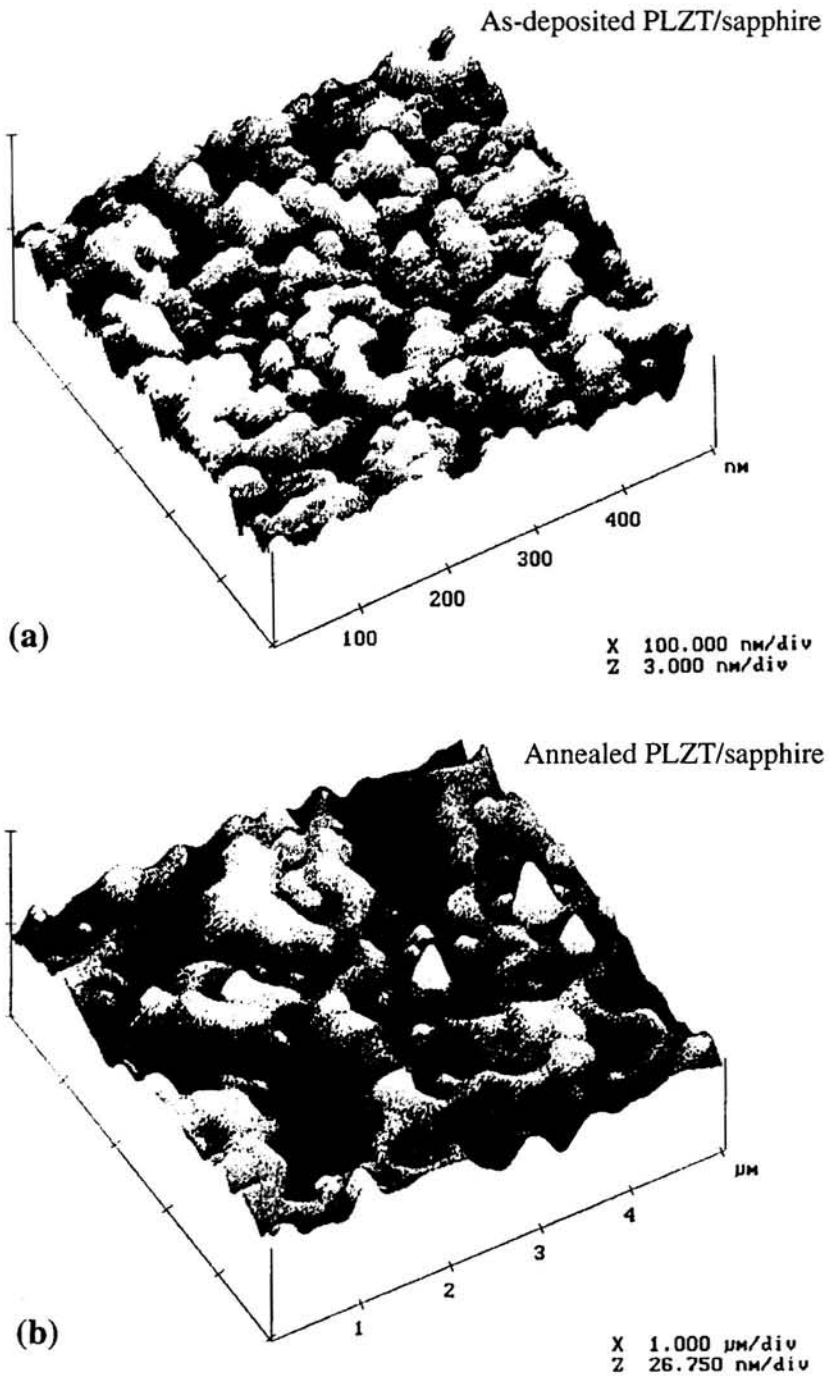


Figure 4-16 Atomic force microscopy images showing surface topology of PLZT (9/65/35) films on r-sapphire (a) as-deposited, and (b) annealed.

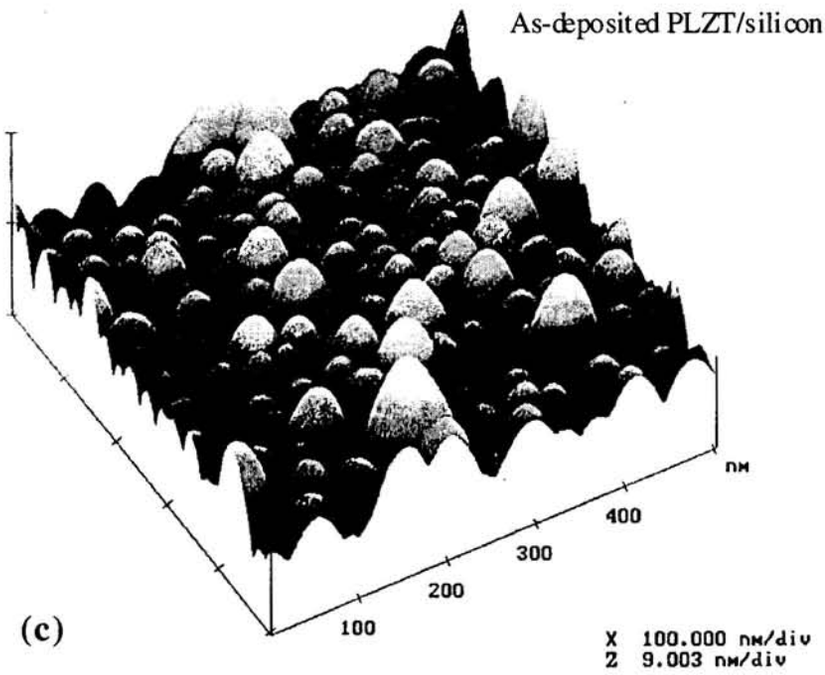


Figure 4-17 AFM of PLZT film on Pt/Si substrate (as-deposited).

The nucleation of nanocrystalline pyrochlore phase in a featureless amorphous matrix was seen in PLZT films deposited between 300°-400°C (Figure 4-18). Figure 4-19 shows a SEM microstructure consisting of pockets of round pyrochlore grains (lighter phase) in an amorphous matrix of a PLZT film after RTA at 550°C for 2 min. Some of the denser areas of these pyrochlore clusters form perovskite phase at higher annealing temperatures. The microstructures were usually lightly etched with buffered HF to reveal the image of the boundaries. The final annealed microstructures showed a dense, uniform matrix of approximately round perovskite grains and the average grain sizes ranged from 0.1-0.8 μm for RTA and 0.2-1.2 μm for furnace annealing under various conditions. A

representative microstructure common to PLZT films on r-sapphire after furnace annealing at 700°C for 30 min is presented in Figure 4-20.

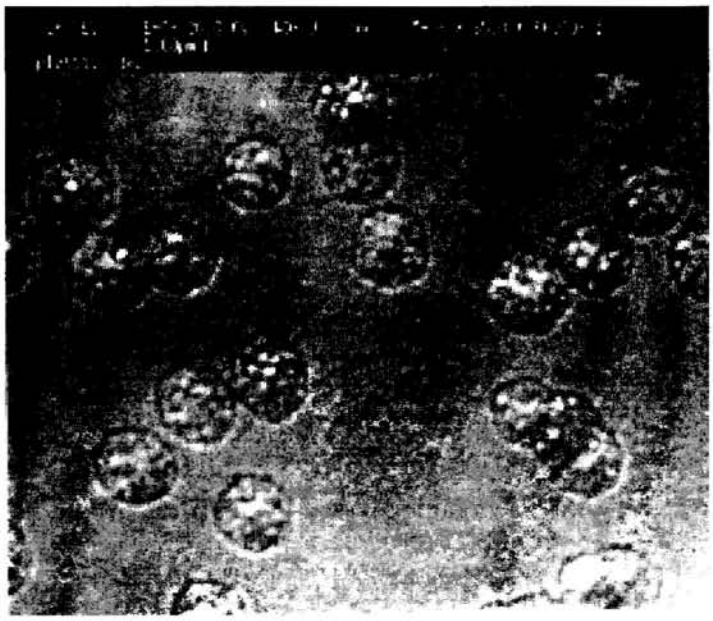


Figure 4-18 Nanocrystalline islands of pyrochlore are nucleated in an amorphous matrix in as-deposited PLZT film on sapphire.

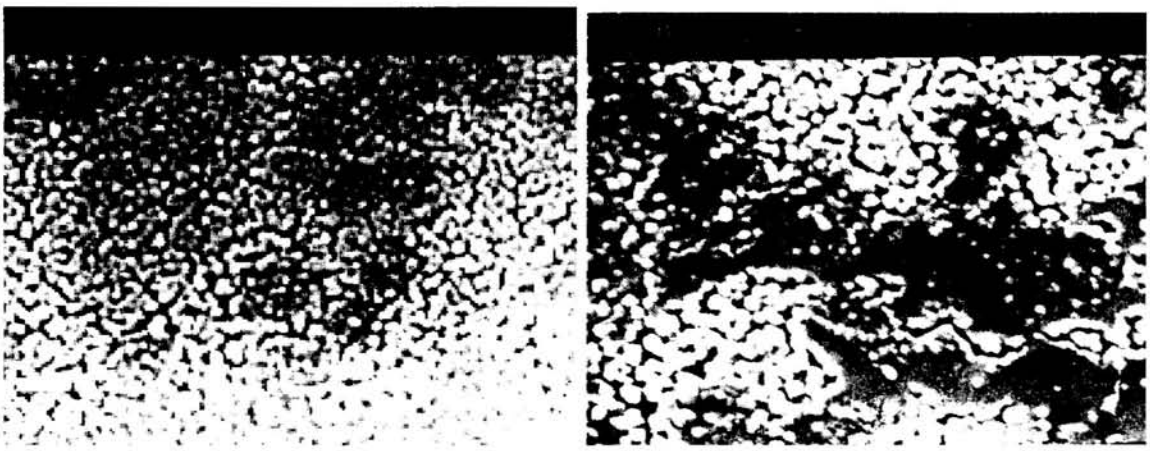


Figure 4-19 The micrographs of PLZT film after rapid thermal annealing at 550°C for 2 min.



Figure 4-20 SEM micrograph of furnace annealed PLZT film (700°C, 30 min).

The fast heating rates help in circumventing the pyrochlore formation at sufficiently high RTA temperatures (>700°C) however, the cracking can occur if slow cooling rates are not used [20]. Two-step heating by RTA (500°C and then to 750°C) was not successful for converting pyrochlore to perovskite phase as we suggested earlier [20]. The majority of the films were processed according to the schedule given in Figure 4-3. The grain size of perovskite phase was around 0.3 μm for 0.4 μm-thick PLZT film on sapphire after RTA at 725°C for 15 sec, 60 sec and 180 sec with decreasing porosity for etched surfaces as shown in Figure 4-21.

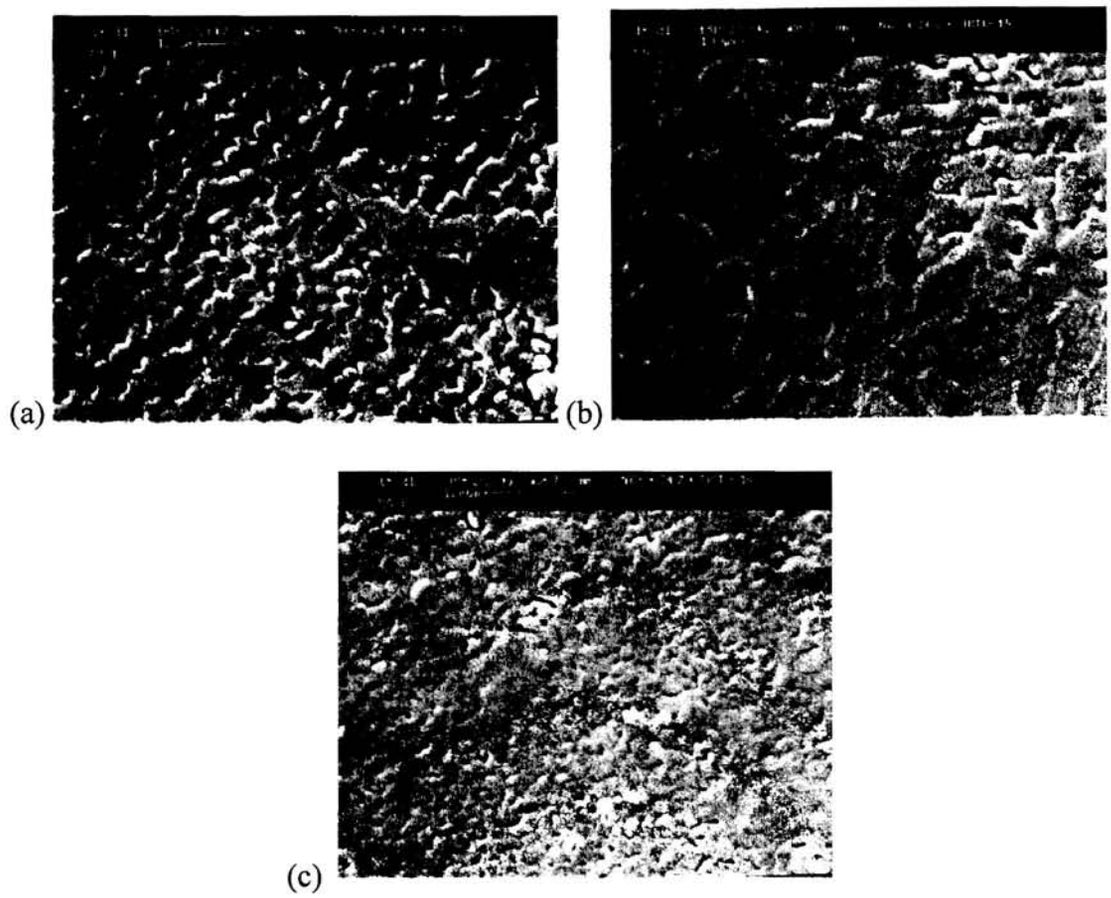


Figure 4-21 SEM micrographs of PLZT films on sapphire post-RTA at 725°C for 15 sec (a), 60 sec (b) and 180 sec (c).

The average grain size was around 1.7 μm for the film furnace annealed at higher temperatures 750°C for a longer period of time, 5 h, as seen in SEM micrograph in Figure 4-22. Grain growth apparently occured for the perovskite grains, larger ones consuming the smaller ones, and the pores were visible in the surface at the grain boundaries probably due to PbO evaporation.

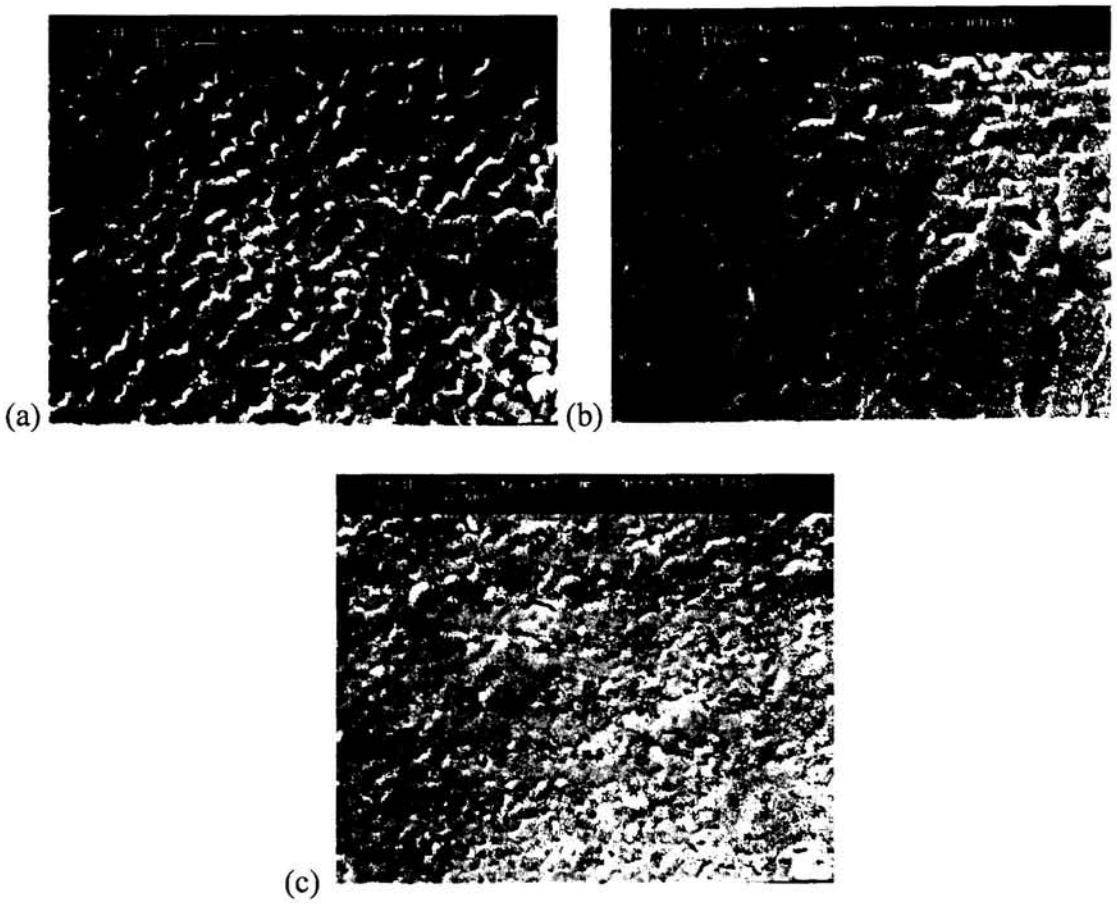


Figure 4-21 SEM micrographs of PLZT films on sapphire post-RTA at 725°C for 15 sec (a), 60 sec (b) and 180 sec (c).

The average grain size was around 1.7 μm for the film furnace annealed at higher temperatures 750°C for a longer period of time, 5 h, as seen in SEM micrograph in Figure 4-22. Grain growth apparently occured for the perovskite grains, larger ones consuming the smaller ones, and the pores were visible in the surface at the grain boundaries probably due to PbO evaporation.

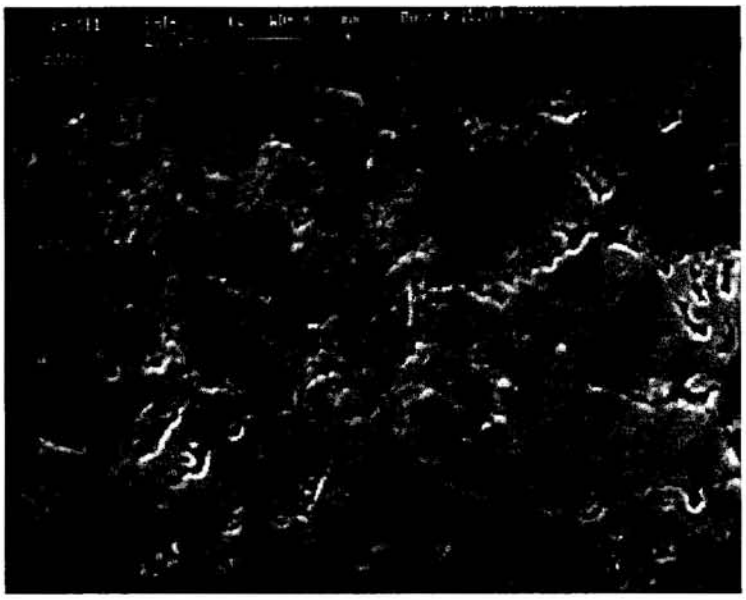


Figure 4-22 Micrograph of PLZT film furnace annealed at 750°C for 5 h illustrating an average grain size of 1.6-1.7 μm with pores on the grain boundaries.

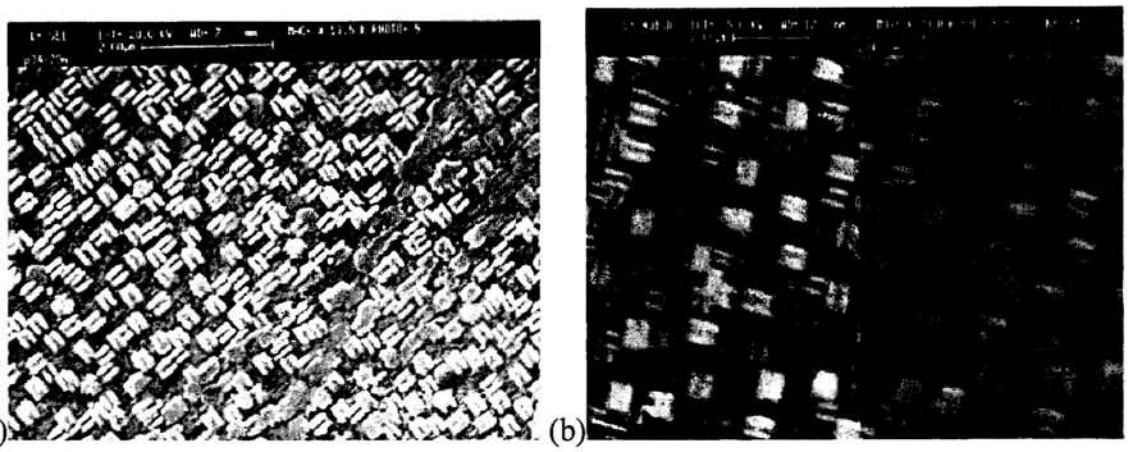


Figure 4-23 SEM micrographs of annealed PLZT films showing the twin-platelets (a) at lower magnification and (b) secondary (right) and backscattered electron images (left) at higher magnification.



Figure 4-24 Microstructure of PLZT film on sapphire after annealing at 700°C, 5 h.

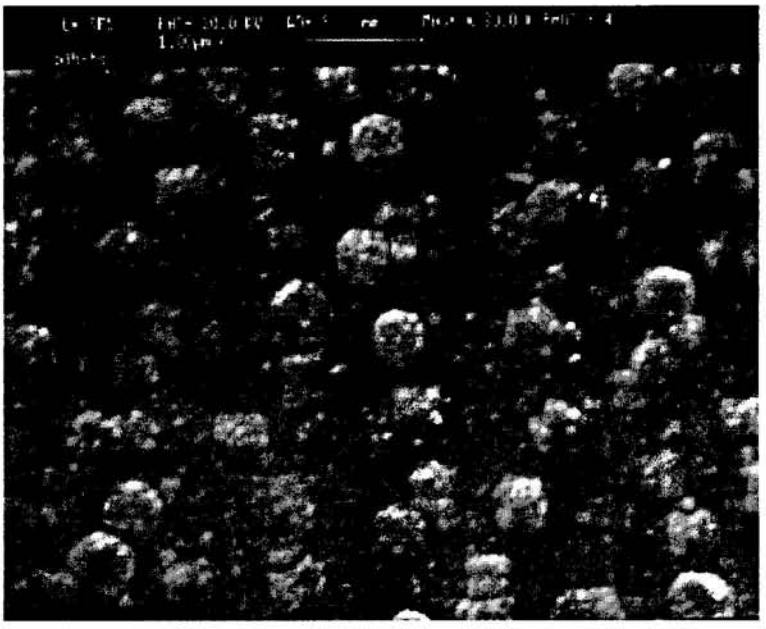


Figure 4-25 Micrograph of PLZT (9/65/35) film on sapphire after furnace annealing, with significant Pb-deficiency. The rounder features of platelets are observed.

Some interesting features emerged in films deposited at 480° and then furnace annealed to 510°C. Precipitates appeared shaped like paired-plates oriented perpendicular to each other across the surface. These twin-platelets were believed to be (110) oriented, given the films had this preferred orientation after annealing. These films were crystalline in the as-deposited condition, possessing a mixture of both pyrochlore and perovskite with (200) orientation. Figure 4-23 (a) shows the microstructure of such a PLZT film on sapphire after furnace annealing at 700°C for 20 min. Backscattered electron imaging (left) and secondary electron imaging (right) are seen in the SEM micrograph (Figure 4-23 (b)), which indicates little evidence for any chemical difference between the platelets and their surrounding. The platelets appear brighter and at a higher level than the surface. Each plate is approximately 85 nm wide and 300 nm long, and they seem to grow larger as the annealing time increases from 5 min to 3 h. It is thought that the formation of these plates at higher deposition temperatures are probably due to the elastic stresses from thermal expansion mismatch betwen the film and the substrate. More work is needed to identify the formation mechansims and orientational relationships of the plates (splitting of plates, etc.) in these films.

An unetched film on sapphire (annealed for 5 h in PbO ambient) which shows an uniform interpenetrating microstructure of such platelets with no apparent porosity, is seen in Figure 4-24. When there was severe Pb-depletion in the annealed films, it caused these platelets to become rounder, as illustrated in Figure 4-25. The PLZT films became less transparent when they had significant amount of Pb-depletion, probably due to

scattering from pores of various sizes. The dielectric constants were reduced with increasing porosity in the films and decreasing grain size. RTA films are characterized by uniform but smaller grain sizes when fully densified. Both the film microstructure and internal stresses are believed to influence the properties of the films. The properties of the PLZT films are presented in the next chapter.

In summary, the microstructure of PLZT 9/65/35 films on r-sapphire was characterized and a correlation was seen between the microstructure, crystal structure and the processing conditions. PLZT films have in general smaller grain sizes after RTA and a small tetragonal distortion, however, films after FA processing show larger grain size with cubic perovskite structure. The perovskite formation was readily achieved by RTA in nitrogen environments even for as-deposited amorphous films due to high heating rates. Furnace annealing is done in protective ambients which has to be PbO-rich to avoid lead deficiency. The grain sizes are for furnace annealed films and dielectric constants were also higher. The dense and stoichiometric film were uniform in composition and optically transparent. The films deposited at substrate temperatures above 480°C exhibited paired-plates across the surface after furnace annealing and more work needs to be done to understand the formation of such plate-like structures.

References

1 S. Krishnakumar, PhD Thesis, University of California, San Diego, 1993.

2 Y. T. Lin, R. Subrahmanyan, A. R. Sitaram and M. Orlowski, "Combined simulation and measurement study of temperature uniformity in rapid thermal processing," Mater. Res. Soc. Symp. Proc., vol. **303**, p.231, 1993.

3 J. Chen, K. R. Udayakumar, K. G. Brooks and L. E. Cross, "Rapid thermal annealing of sol-gel derived lead zirconate titanate thin films," *J. Appl. Phys.*, **71**, 4465, 1992.

4 Y. S. Hwang, S. H. Paek, J. H. Lee, C. S. Park, J. S. Choi, J. K. Kung and Y. N. Kim, "Formation and characteristics of lead lanthanum zirconium titanate thin films formed by using the rf sputtering method," *J. Mater. Sci. : Mater. Electronics*, 7, 309, 1996.

5 Y. Yoshikawa and K. Tsuzuki, "Crystallization of fine, chemically prepared lead lanthanum zirconate titanate powders at low temperature," *J. Am. Ceram. Soc.*, **73**, 31, 1990.

6 T. Tani and D. A. Payne, "Lead oxide coatings on sol-gel derived lead lanthanum zirconium titanate thin layers for enhanced crystallization into the perovskite structure," *J. Am. Ceram. Soc.*, **77**, 1242, 1994.

7 M. E. Fine, Introduction to Phase Transformations in Condensed Systems, Chap. 3, The Macmillan Company, New York, 1965.

8 K. C. Chen and J. D. Mackenzie, "Crystallization kinetics of metallo-organics derived PZT thin film," Mat. Res. Soc. Symp. Proc., vol. **180**, p. 663, 1990.

9 C. H. Peng and S. B. Desu, "Investigation of structure development in MOD $Pb(Zr_xTi_{1-x})O_3$ films by an optical method," Mater. Res. Soc. Symp. Proc., vol. **243**, p. 335, 1992.

10 C. K. Kwok and S. B. Desu, "Formation kinetics of $PbZr_xTi_{1-x}O_3$ thin films," *J. Mater. Res.*, **9**, 1728, 1994.

11 J. H. Joo, D. S. Kil and S. K. Joo, "Effect of Pb content on the transformation of sputtered $Pb_xZr_{0.4}Ti_{0.6}O_3$ thin film," Mater. Res. Soc. Symp. Proc., vol. **321**, 591, 1994.

12 S. I. Jang, B. C. Choi and H. M. Jang, "Phase-formation kinetics of xerogel and electrical properties of sol-gel derived $Ba_xSr_{1-x}TiO_3$ thin films," *J. Mater. Res.*, **12**, 1327, 1997.

13 P. J. Borelli, P. H. Ballentine and A. M. Kadin, "Compositional and structural properties of sputtered PLZT thin films," Mater. Res. Soc. Symp. Proc., vol. **243**, p. 417, 1992.

14 C. K. Kwok and S. B. Desu, "Role of oxygen vacancies on the ferroelectric properties of PZT thin films," Mater. Res. Soc. Symp. Proc., vol. 243, p. 393, 1992.

15 B. Cullity, Elements of X-ray Diffraction, Addison-Wesley Co., Reading, MA, 1956.

16 D. E. Dausch and G. H. Haertling, "The domain switching and structural characteristics of PLZT bulk ceramics and thin films chemically prepared from the same acetate precursor solutions," *J. Mater. Sci.*, **31**, 3409, 1996.

17 K. D. Preston and G. H. Haertling, "Microstructural investigation of acetate-derived PLZT films," *Integ. Ferroelectrics*, **1**, 89, 1992.

18 H. Adachi, T. Mitsuyu, O. Yamazaki and K. Wasa, "Ferroelectric $(Pb,La)(Zr,Ti)O_3$ epitaxial thin films on sapphire grown by rf-planar magnetron sputtering," *J. Appl. Phys.*, **60**, 736, 1986.

19 K. Wasa, T. Satoh, K. Tabata, K. Adachi, Y. Yabuuchi and K. Setune, "Effects of PLT-buffer layer on microstructures of sputtered PLZT thin films epitaxially grown on sapphire," *J. Mater. Res.*, **9**, 2959, 1994.

20 B. Tunaboylu, P. C. Harvey, F. Deng, C. Fan and S. C. Esener, "Growth and characterization of oriented lead lanthanum zirconate titanate thin films on sapphire," Proc. III. Intl. Ceramic Congress, Istanbul, vol. **2**, p. 349, 1996.

5. This work : Characterization of dielectric, optical and electrooptic properties of PLZT 9/65/35 films on sapphire

Dielectric, optical and electrooptic properties have been observed to vary significantly in PLZT films depending on the deposition method and post-deposition processing as reported in chapter 3. To date, there has been little investigation on the dielectric and electrooptic properties of PLZT 9/65/35 films on r-sapphire as function of processing conditions. In this chapter, we present our results on the characterization of dielectric, optical and electrooptic properties of PLZT films on r-sapphire. Dielectric and electrooptic properties of magnetron sputtered PLZT 9/65/35 films were found to be strongle dependent on annealing conditions. The peak dielectric constant of the films were 1200 and 2800 with Curie temperatures of 100°C and 190°C after RTA and FA processing respectively. The dielectric losses in the films were fairly low; tan deltas were less than 0.02 after RTA and less than 0.04 after FA processing. The films showed good optical transmission characteristics after annealing and a large effective quadratic electrooptic effect was observed in a furnace annealed film.

5.1 Electrical properties

5.1.1 Measurements by an IDE structure

Electrical properties of PLZT thin films on insulating sapphire substrate were measured by surface interdigitated electrodes (IDE) patterned using a lift-off technique.

Sandwich parallel-plate electrodes could be used on conductive substrates, such as platinized silicon. The capacitance between two electrodes placed on the PLZT film surface is very small and its measurement by standard LCZ meters could lead to large errors for dielectric constants varying from 10 to 5000. Hence, an IDE structure is needed to measure the capacitance of insulating films on insulating substrates. The Cr/Au electrodes (20 nm Cr/200 nm Au) were patterned onto the films by lift-off lithography and a successive evaporation procedure. The masks were prepared (by e-beam lithography) containing several geometries of IDE patterns as well as specific patterns for EO measurements.

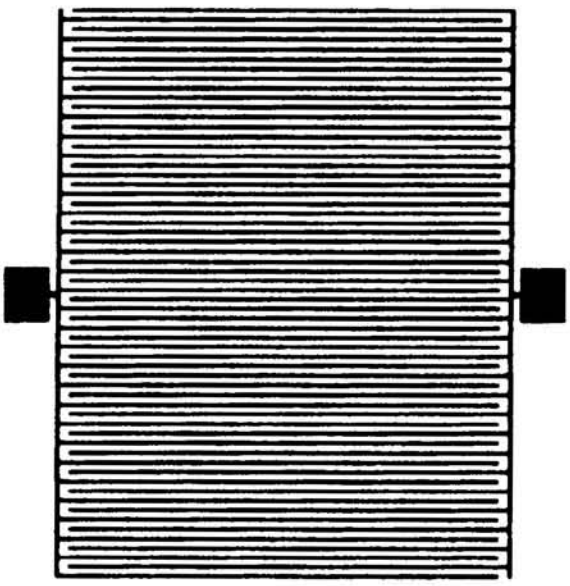


Figure 5-1 An interdigitated electrode (IDE) structure that was patterned onto a mask for photolithography steps.

The dielectric constant of the film (ε_f) was calculated from the measured capacitance of the IDE using the equation [1]

$$C = Knl \{(\varepsilon_s+1) + (\varepsilon_f - \varepsilon_s) [1 - \exp(-4.6t/L)]\} \quad (5\text{-}1)$$

where $K= 6.5 (D/L)^2 + 1.08 (D/L) + 2.37$ and D is the finger width, n is the number of fingers in the IDE, l is the finger length of the IDE, ε_s is the dielectric constant of the substrate, t is the film thickness and L is the center-to-center spacing between adjacent fingers of the IDE. In our study, the width of the electrodes chosen ranged between 2 to 4 μm and the gaps between electrodes were 4 to 8 μm. These optimum parameters in the design were obtained to minimize the error in the measurements using simulation. The capacitance was measured at 2° intervals and at the temperature range between 250 K (-23 °C) - 580 K (307 °C) to observe the critical phase transitions. The capacitance and tangent delta (dielectric loss) measurements were made at frequencies of 10 kHz, 100 kHz and 1 MHz using a LCZ impedance analyzer. An example of an IDE pattern is shown in Figure 5-1.

5.1.2 Results of dielectric property characterization of PLZT films on sapphire

The dielectric constant (ε_r) of the as-deposited films was in the range of 25 to 50 at room temperature. Figure 5-2 shows the ε_r versus temperature (T) curve for a film with the pyrochlore structure, indicating a ε_r of 40 at room temperature for frequencies between 10 kHz and 1 Mhz. However, the dielectric constants of films annealed were much higher ranging from 700 to 2500 (at 10 kHz) at room temperature, depending on both deposition and annealing conditions. The presence of a low ε_r phase, at the grain boundaries or film surface, even in small amounts would be expected to have

disproportionately large effect on the apparent dielectric constant, due to its function as an additional low capacitance in series.

The ε_r versus T curve of annealed films shows a characteristic diffuse ferroelectric-to-paraelectric transition similar to bulk behavior. Curie temperatures (T_c), however, are shifted to higher temperatures between 110°C and 190°C, depending on the annealing conditions. This shift to higher T_c's is in agreement with previous results on the PLZT 9/65/35 films [2,3]. Also, the thin-film dielectric constants are lower than the bulk values for this composition. These differences are attributable to smaller grain sizes as compared to that of the bulk ceramic and also the internal stresses developed in the films as they are cooled to room temperature. The average grain size observed in the films is around 1 μm which is smaller than reported bulk values ranging from 2.5 to 8 μm in the literature.

The PLZT has an average coefficient of thermal expansion (CTE) of $5.4 \times 10^{-6} °C^{-1}$ which is smaller than the CTE of r-sapphire substrate, $5.8\text{-}7.7 \times 10^{-6} °C^{-1}$ in the temperature range of 20° to 500°C. Therefore, we can expect that a two-dimensional compressive stress is imparted on PLZT thin films deposited on sapphire as the substrate contracts more than the film upon cooling down to room temperature.

The peak dielectric constants (ε_{max}: 800-1200) and T_cs (110-130°C) of rapid thermally annealed films were both lower than those of furnace annealed films, 1700-2800 and 130-190°C, respectively. The films deposited in the amorphous state and then annealed generally exhibited somewhat lower peak ε_r than the films deposited crystalline and then annealed to achieve a single-phase perovkite, regardless of the type of annealing.

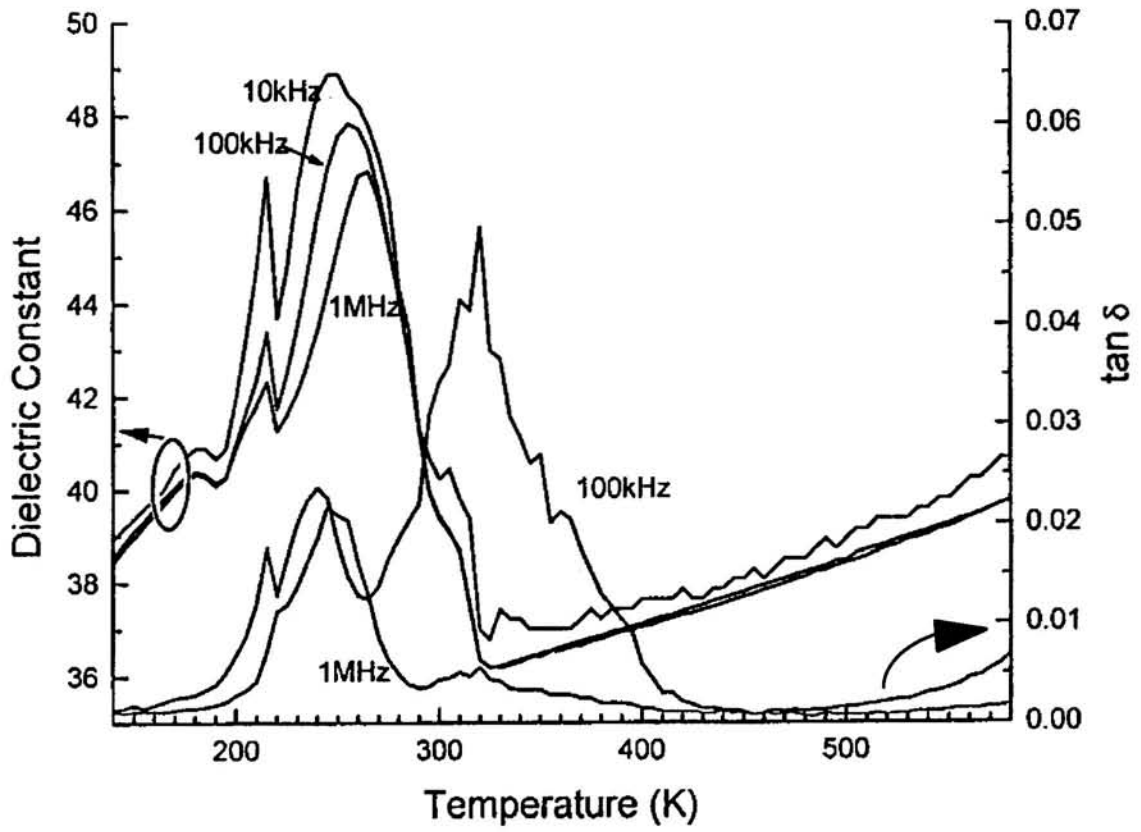


Figure 5-2 Dielectric constant and loss versus temperature for the as-deposited PLZT film on sapphire.

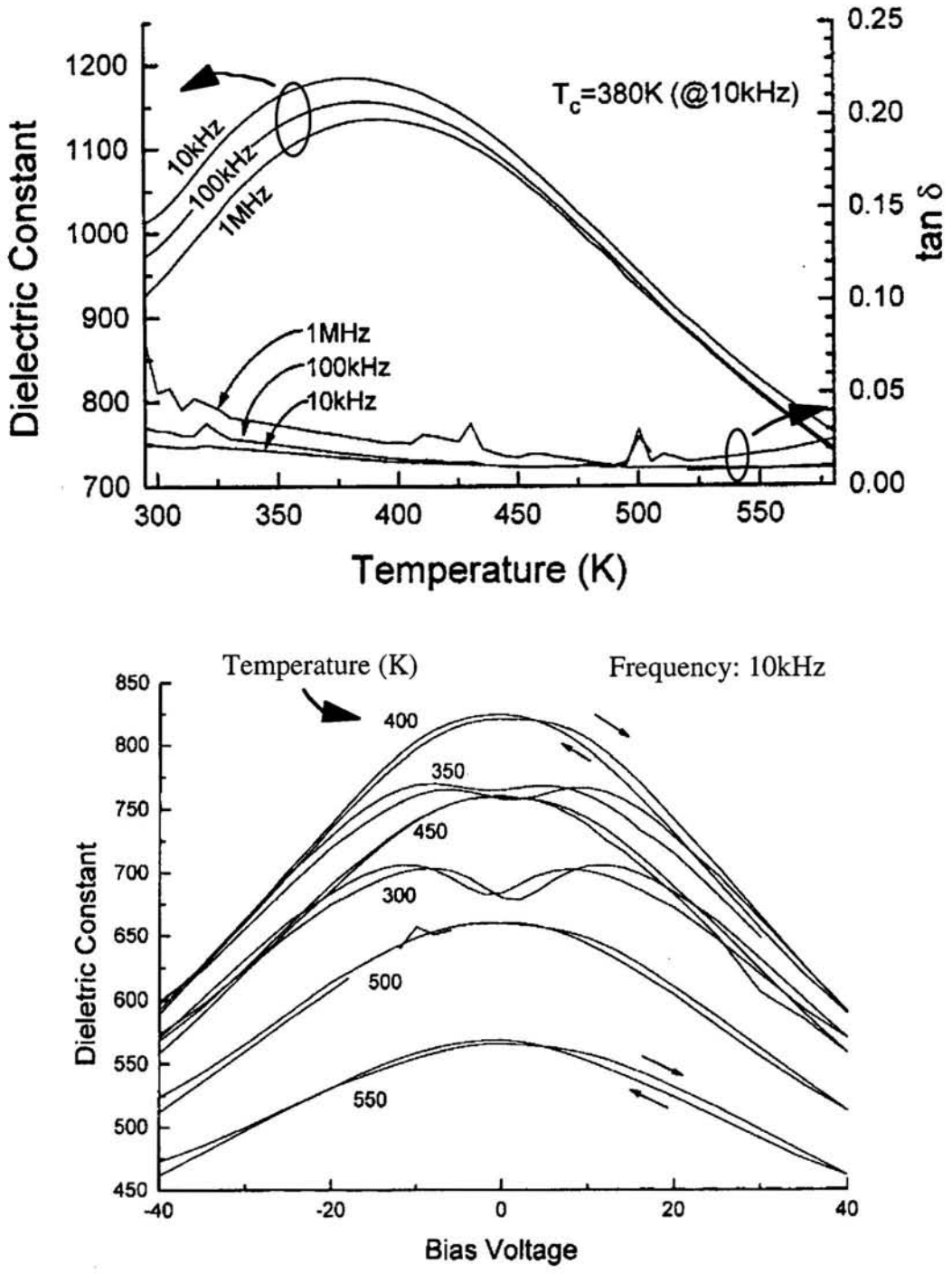


Figure 5-3 The temperature dependence of dielectric constant and loss (top) and dc-bias response (bottom) of 0.5 μm-thick rapid thermally annealed PLZT film on sapphire.

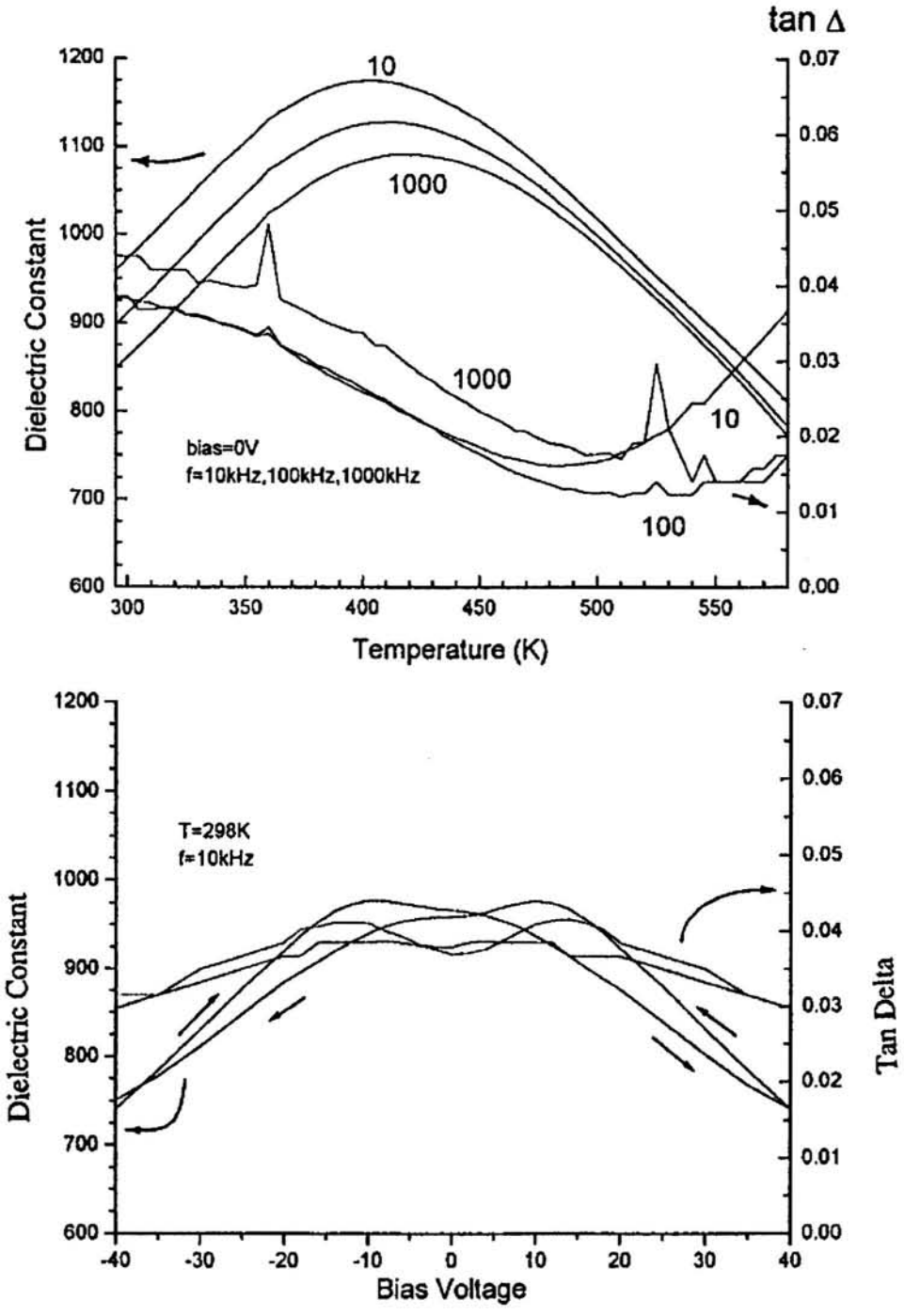


Figure 5-4 Dielectric properties as a function of temperature (a) response with bias voltage (b), for a 0.75 μm-thick PLZT film (post-RTA).

Figure 5-3 (a) shows the temperature dependence of dielectric properties of rapid thermally annealed PLZT film (730°C for 3 min) about 0.5 μm thick. The transition is at ~110°C and the room-temperature ε_r and peak ε_r are approximately 1000 and 1200 (at 10 kHz), respectively. The dielectric loss, tan δ, is approximately 0.03 in the temperature range of measurement from 25°C to 290°C. The dc-bias response of the film is shown in Figure 5-3 (b) as the voltage is varied from -40 V to +40 V and back to -40 V at 50° temperature intervals. For temperatures above T_c, a more symmetric response with a slimmer-loop is observed as expected from the quasi-cubic paraelectric phase. The hysteretic behavior of the film at room temperature is suggestive of its ferroelectric character, in agreement with its tetragonal distortion observed by x-ray diffraction.

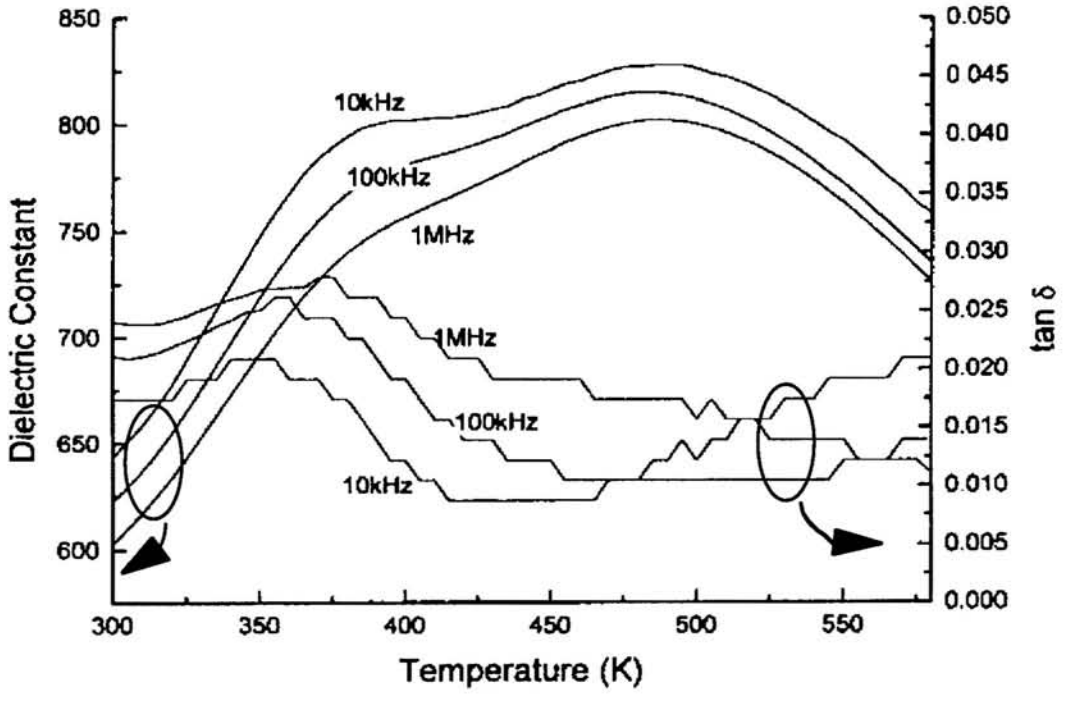


Figure 5-5 Dielectric constant and loss as a function of temperature for 0.35 μm-thick PLZT film after a two-step annealing.

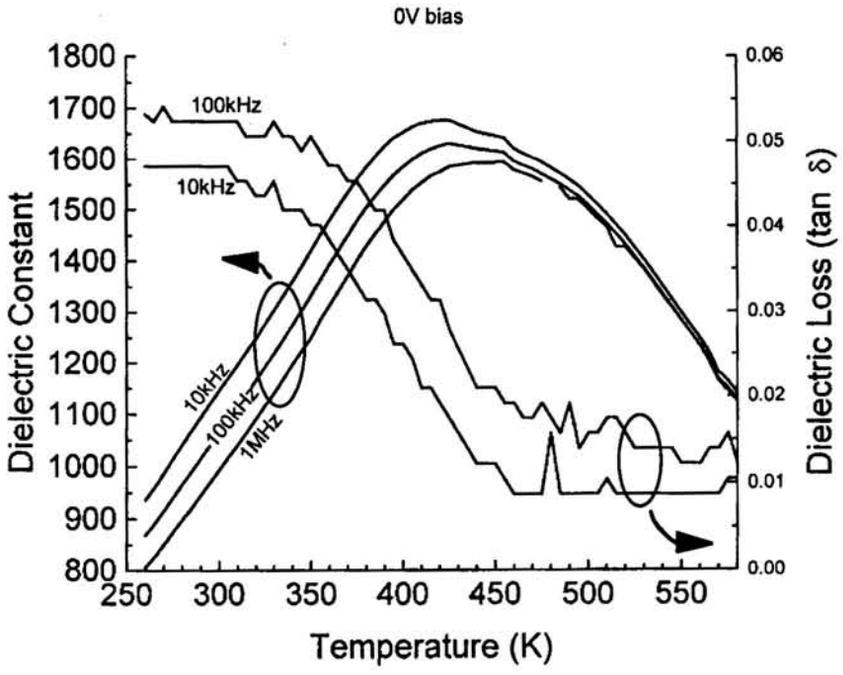


Figure 5-6 Temperature dependence of dielectric constant and loss for a PLZT film on sapphire. The film was deposited below 300°C and then furnace annealed at 700°C, 3 h.

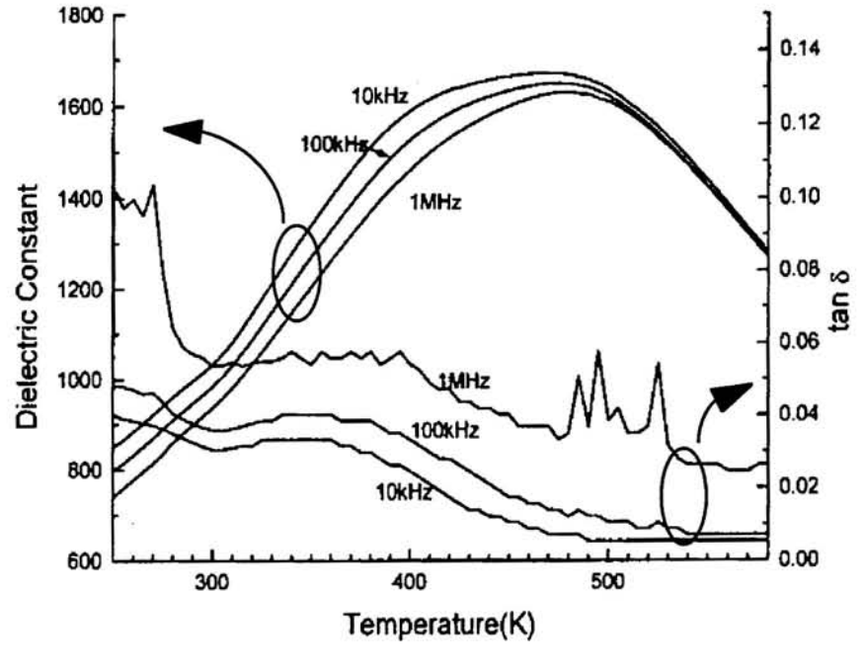


Figure 5-7 Dielectric constant and loss as a function of temperature for PLZT film (0.75 μm) deposited at low temperature and annealed at 750°C for 3 h.

Another somewhat thicker, 0.75 μm, film subjected to the same RTA treatment showed a very similar ε_r-vs-T curve with similar ε_r values but its tan δ was higher (0.04) and it exhibited a more memory-like dc-bias response with a larger hysteresis loop (Figure 5-4 (a) and (b)). In addition, T_c of this film is nearly 130°C, a little higher than the former.

The dielectric constants of rapid thermally annealed PLZT films seemed to decrease with decreasing film thickness below 0.5 μm. The room temperature of a 0.35 μm thick film was about 550 as compared to thicker films which showed higher ε_rs, 900-1000. A 0.35 μm-thick film which was furnace annealed at 600°C for 1 h after the initial RTA-step exhibited a dielectric constant vs. temperature with two distinct transitions. The first transition was at 110°C and the second was at approximately 200°C with a maximum ε_r of 825, as seen in Figure 5-5. The room temperature ε_r remained around ~ 650. Formation of microdomains in the grains due to internal stress relief after annealing for 1 h may be responsible for double peaks in the dielectric response. However, a new phase formed on the film surface could also alter the dielectric properties with respect to temperature to account for such an unusual ε_r-vs-T behavior.

For PLZT films furnace annealed to 650°-700°C ($PbO+O_2$ ambient), higher peak ε_r values were observed, from 1700 to 2800. This is probably due to films having higher densities as well as larger grain sizes and also possibly due to the stress-relief in the films. The room temperature ε_r values were similar, in the range 900-1000, for films deposited at low temperature as amorphous followed by furnace annealing to the perovskite phase.

The dielectric constants were relatively independent of the thickness for annealed films but were fairly dependent on the processing conditions and the microstructure.

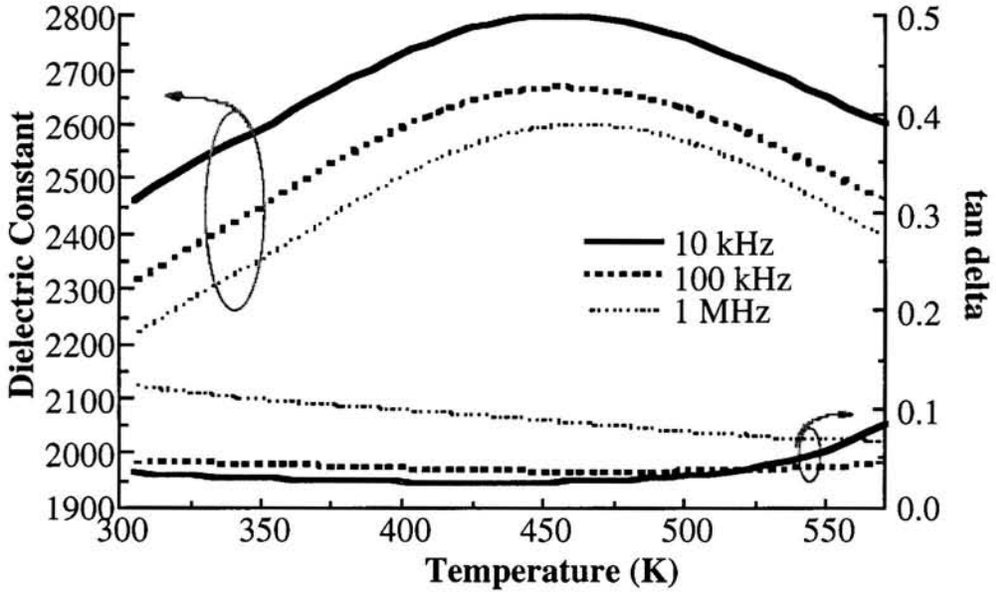


Figure 5-8 Dielectric constant and loss tangent as a function of temperature for a PLZT film deposited at 490°C and annealed at 700°C for 20 min.

Figure 5-6 demonstrates a ε_r-vs-T of PLZT film (0.67 μm thick) deposited below 300°C and then annealed at 700°C for 3 h. It can be seen that ε_r (RT) is 950 and becomes ~1700 at Curie temperature of 137°C, exhibiting a sharper transition. The dielectric loss is around ~ 0.05 at room temperature and decreases to 0.01 above the T_c, which is a fairly small value. Films annealed to 750°C for few hours after low temperature deposition, show similar peak dielectric constant values with a broader transition with a T_c of ~200°C and higher losses, tan δ of 0.06 for 1 MHz at room temperature (Figure 5-7). However,

the room temperature ε_r was very high, 2450 for a PLZT film (0.6 μm) deposited at higher temperature as crystalline (pyrochlore+perovskite) followed by furnace annealing at 700°C for 20 min, as shown in Figure 5-8. The peak ε_r was extremely high, 2800, highest reported value for a PLZT 9/65/35 film on sapphire. The dielectric loss was low, tan δ of 0.04 (at 10 kHz), and fairly constant between 25° to 230°C and gradually increasing at higher temperatures.

It should be noted that sputtered and annealed PLZT films in this study exhibited remarkably low frequency dispersion characteristics. For instance, a drop of only 10% in the dielectric constant (from 2450 to 2220) was observed from 10 kHz to 1 Mhz in these sputtered films as compared to earlier reports where a drop of 85% (from 1700 to 250) [4] and 63% (from 1750 to 650) [5] were seen from 10 kHz to 1 MHz. Also, the dissipation factor (tan δ) values observed in this study, 0.01-0.04, are much smaller than values reported earlier, ranging from 0.098-0.14 [6,7]. When a low tan δ was obtained, 0.05, however, it was at the expense of dielectric constant for a sol-gel derived PLZT 9/65/35 film, ε_r of 470-910 [8]. A high dielectric constant, 4001, observed for the acetate-derived PLZT 9/65/35 film on a ductile silver foil substrate was accompanied by a high dielectric loss, 0.17 [9]. As reported by Dausch and Haertling [9], unlike the bulk behavior, these 9/65/35 films on silver and Pt/Si exhibited ferroelectric hysteresis loops with a memory character, a high field coercivity, (E_c) 9 kV cm^{-1} and a remanent polarization of 11 μC cm^{-2}. The hysteresis loop of this film composition (9% La), however, remained much slimmer than films with 6-8 La%. The substrate and the

deposition method seem to have a significant effect on the ferroelectric nature of these films. For example, Teowee et al observed a higher E_c value, 44 kV cm^{-1}, for sol-gel PLZT 9/65/35 films on Pt/Si [8]. The residual internal stresses in the PLZT thin films could be responsible for the more ferroelectric-like response, as suggested earlier by other researchers [9].

In an earlier work, the effect of externally applied stress (tensile and compressive) on the dielectric constant of the 9/65/35 film on silver was found to be fairly small and the PLZT 28/0/100 film on silver suffered a larger reduction in ε_r [10]. The results on the sapphire substrate could be different, of course, because a plastically yielding metal silver substrate would be more forgiving in relaxing stress than Al_2O_3 (i.e. sapphire). In general, it can be assumed that both the microstructure (small grain size) and the internal stress have influence on the dielectric constant of PLZT 9/65/35 films on r-sapphire and are thought to be responsible for the lower ε_r exhibited by RTA-processed films. Furnace annealing in PbO ambient, of films deposited as amorphous or crystalline, resulted in higher dielectric constants than the RTA processing for sputtered PLZT 9/65/35 films on sapphire.

The dielectric constant and loss tangent as function of temperature for rapid thermally annealed or furnace annealed films were similar and curves overlapped on both heating and cooling. For films furnace annealed at temperatures 715°C or above, the ε_r and tan δ values were slightly higher, a rise in ε_r of 50-100, on cooling, as shown in Figure 5-9 (a). This can be attributed to the remanent polarization and slow polarization

relaxation in the sample which are increasing the polarizability and thus the dielectric constant. Another possibility is the defects on the surface of the film which may induce space-charge sites on grain boundaries or domain walls, leading to the small increase in the dielectric constant below the T_c.

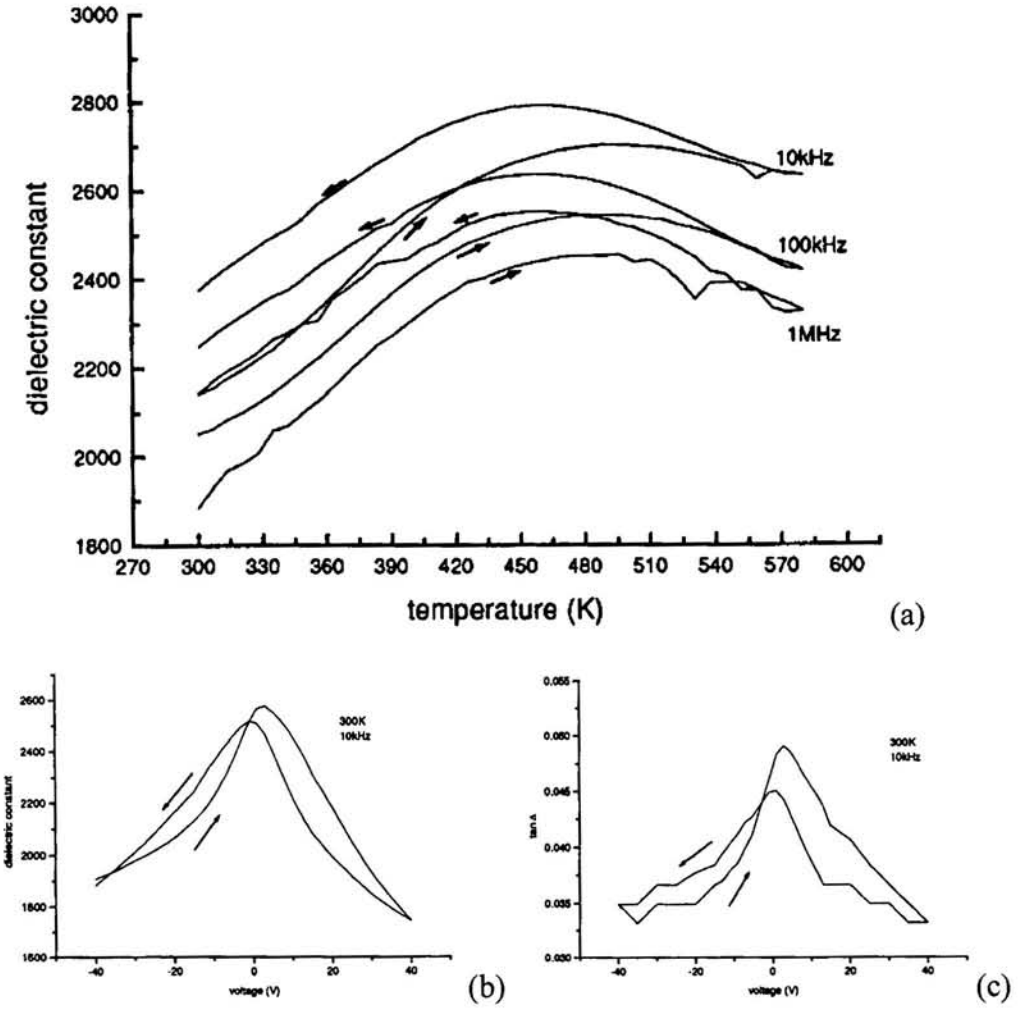


Figure 5-9 Temperature dependence of the dielectric constant and loss of a furnace annealed PLZT film on sapphire (a), and the effect of dc-bias voltage on the dielectric constant (b) and tangent loss (c) for the same film.

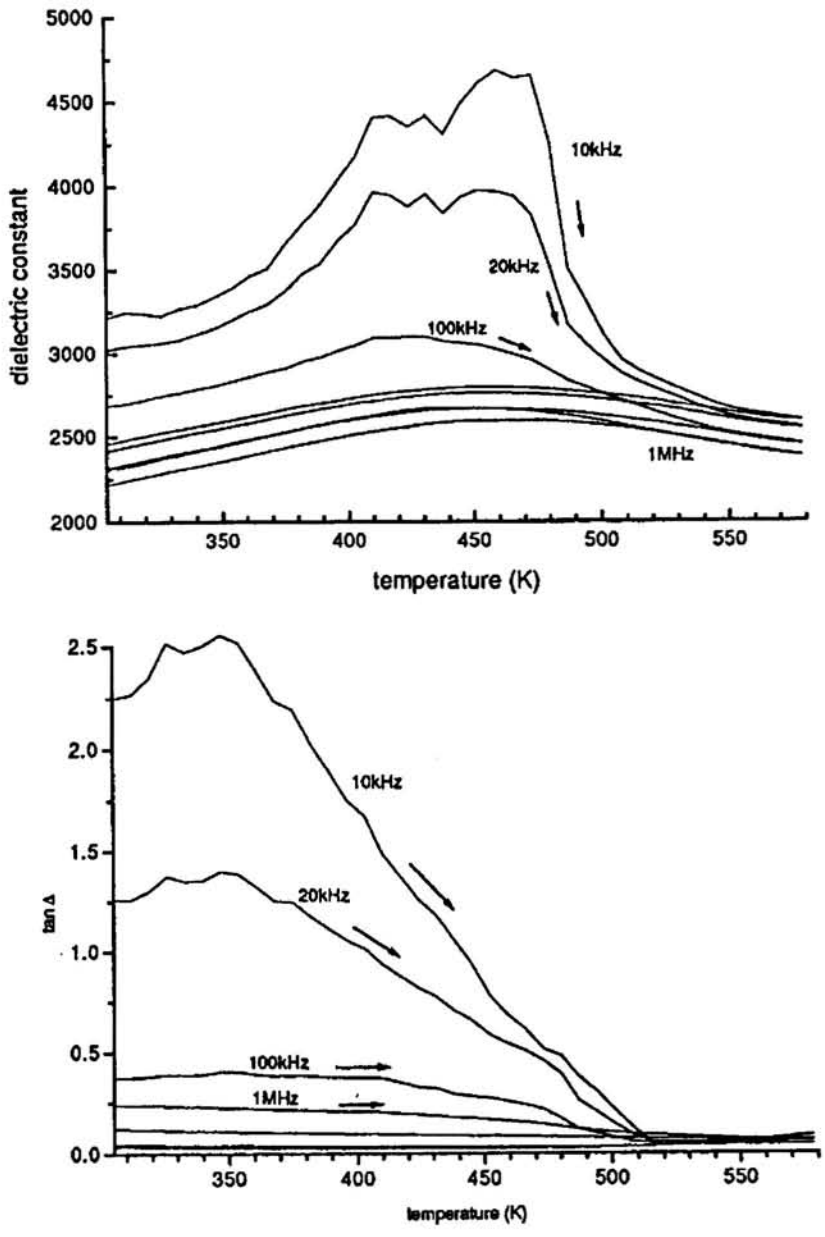


Figure 5-10 Influence of poling the PLZT film on the dielectric constant (top) and tangent loss (bottom).

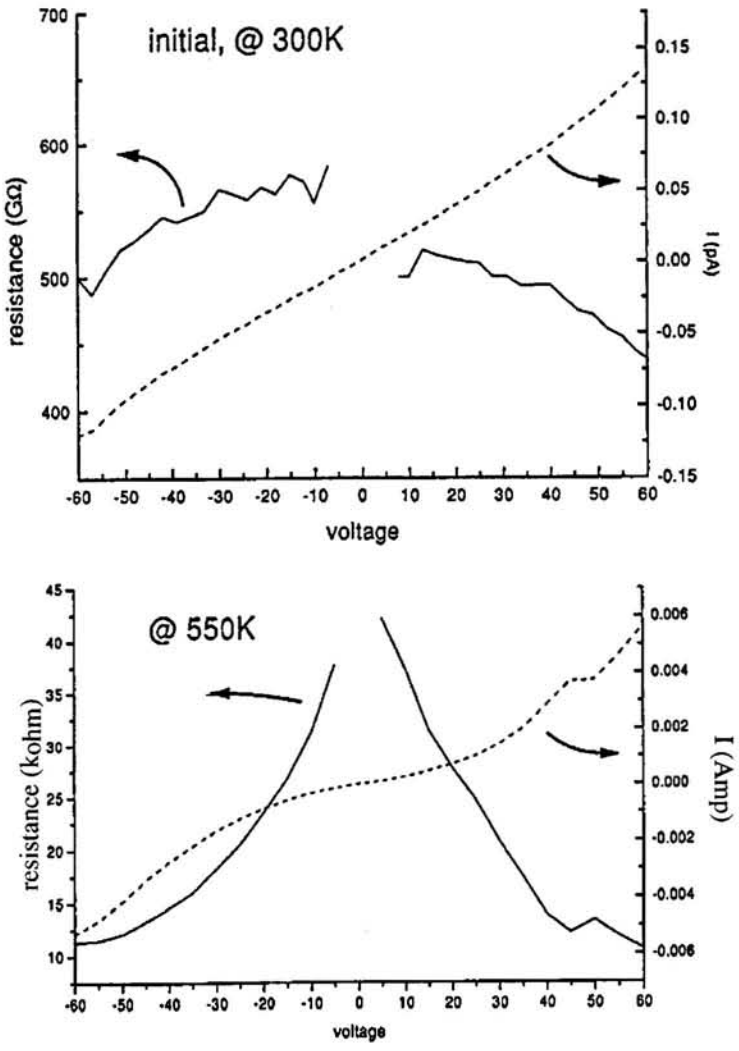


Figure 5-11 Resistance vs voltage and I-V curves for an annealed Pb-deficient PLZT film before and after poling.

The loss tangent values were very similar on both heating and cooling but Curie temperature was shifted to a slightly lower temperature. The film showed a relaxor slim-loop behavior with bias voltage as a dc-bias was applied from -40 V to +40 V, as seen in Figure 5-9 (b) and (c) for both the dielectric constant and tan δ vs. the bias voltage at room temperature at 10 kHz.

The influence of poling (10 V, 550K) the furnace annealed PLZT film was the jump in dielectric constant in the heating cycle and lowered back to normal virgin sample values at 277°C (550K) and upon cooling to room temperature, as seen in Figure 5-10 (a). The loss tangent displayed a dramatic increase for the poled film as compared to its virgin state below T_c, especially for low frequency 10-20 kHz, and then lowered above T_c and upon cooling (Figure 5-10 (b)). The poling apparently aligns any existing macro-micro domains along the electric field and hence increases the remanent polarization in the grains in a specific orientation, giving rise to the jump in dielectric constant at low frequencies.

The annealed PLZT films are commonly insulating films with substantial resistivity. The resistance measured are usually in the GΩ range. An important finding from the poling measurements was that an annealed film showed decreasing resistance with increasing bias field after poling while most of the films had constant resistance before and after poling. Initially this film showed a high resistance and its resistance was reduced with voltage in a quadratic fashion after poling as seen in Figure 5-11 (a) and (b). I-V characteristic is also plotted for both cases, indicating an increase in leakage current in the poled film. This examined film showed a significant Pb-deficiency of about 8% from the stoichiometric composition. Therefore, it is plausible to think that this post-poling behavior in this film is attributable to a possible surface layer with a lower ε_r and a space-charge field generated due to Pb^{2+} and O^{2-} vacancies. Further analysis is necessary to figure out all the parameters involved to reach a conclusion for this peculiar behavior of PLZT films on sapphire. One conclusion, however, from this result is that the resistivity

has to be taken into account in making electro-optic measurements since the thermal effect here could affect, most likely increase, the observed EO response in the films. Therefore, care was taken in making EO measurements on PLZT films on sapphire in this study and we considered the films with and without resistance change, as reported in the next section.

5.2 Optical properties

Optical properties of PLZT thin films on sapphire substrate have been investigated in terms of optical transmission and wave-coupling measurements. The optical transmittance has been measured with a spectrophotometer in the wavelength range from 300 nm to 900 nm. The dispersion curves of the refraction indices and absorption coefficients as well as the thickness of the films have been determined from the interference oscillations of the transmission spectra. The transmission curves of the substrate with and without the film layer are analyzed. The absorption of the substrate as well as the light scattering on the film were assumed to be negligible. The thickness (t) of the film was also determined independently both by RBS and prism-coupling measurements and correlated with the transmission data.

The film transmittance T_f can be shown to be $T_f = 1/(1+T^{-1}-T^{-1}_s)$ where T is the measured transmittance of the sample and T_s is the measured or calculated transmission of uncoated sapphire substrate. The need for elaborate fitting procedure for determination of absorption coefficient can be avoided by averaging data between two adjacent extrema.

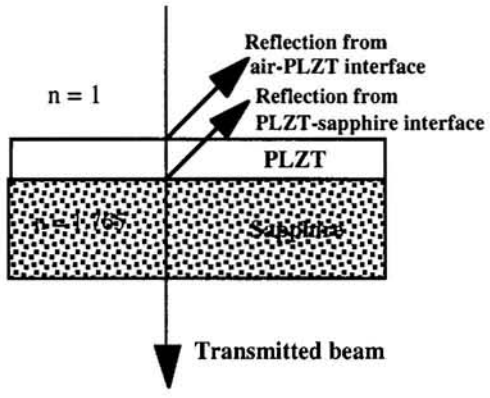


Figure 5-12 The structure used to model the transmittance vs. wavelength of PLZT 9/65/35 film on sapphire.

The approximation of the average transmittance can be expressed as [11]:

$$T_{avg} = t_1 t_2 t_3 \exp(-A)[1+r_2 r_3+(r_1 r_2+r_2 r_3)\exp(-2A) \qquad (5\text{-}2)$$

where r_i and t_i represent transmission and reflection coefficients at interfaces 1 (air-film), 2 (film-substrate) and 3 (substrate-air) and where

$$r_i = \left(\frac{n_i - n_{i+1}}{n_i + n_{i+1}}\right)^2; \qquad i = 1, 2,3 \qquad (5\text{-}3)$$

and $t_i = 1\text{-}r_i$. A is the product of the film absorption coefficient (α) and the thickness. The average index n and approximate value of absorption index k can be determined at the maxima points from T_{max}, T_{int} (center of two adjacent minima) and from the order of interference *m* as a function of wavelength . The *m* can be defined as $m = \lambda_{m+1}/ \lambda_m - \lambda_{m+1}$, where m and m+1 are the wavelength at two adjacent extreme points [11].

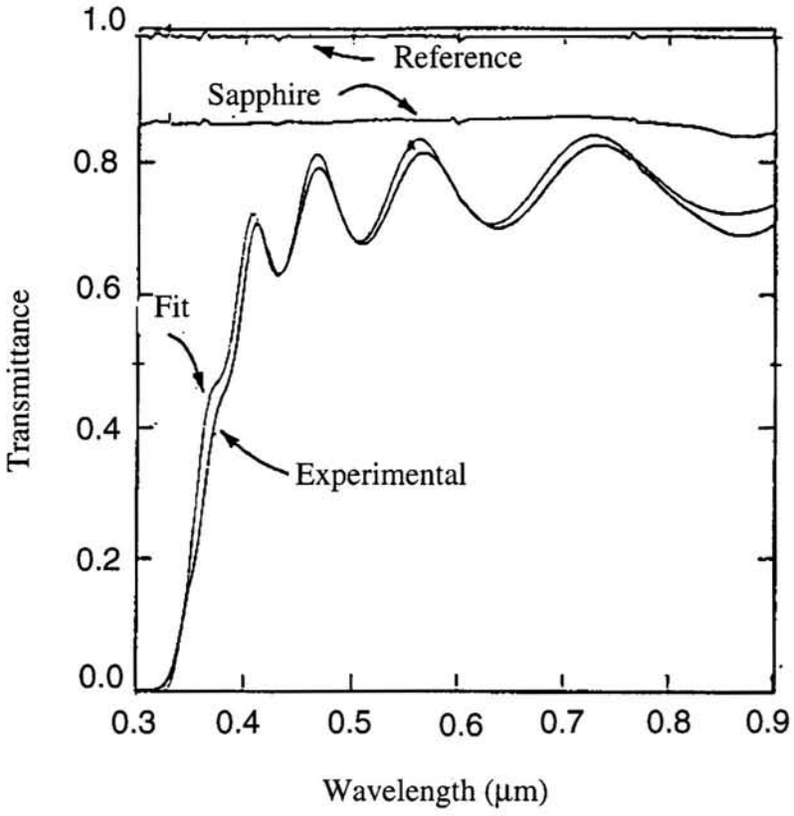


Figure 5-13 The measured and simulated transmission curves for annealed PLZT 9/65/35 film on sapphire, with 0.44 μm thickness.

The simulated transmission curves are obtained from a known transfer matrix calculation as outlined by Born and Wolf [12], by considering an air-PLZT thin film-sapphire substrate structure as shown in Figure 5-12. From the characteristic matrix we can extract the reflected and transmitted intensity. Absorption spectrum was extracted by matching the peak to valley height of the transmittance spectrum. The results of the simulation as well as the transmission measurements of an RTA processed PLZT 9/65/35

thin film on sapphire from 300 nm to 900 nm are seen in Figure 5-13. The annealed PLZT film thickness is calculated to be 0.44 μm, which is in agreement with the thickness obtained from prism-coupling method. The absorption edge of the film is approximately 330 nm, which is lower than the value for bulk PLZT 9/65/35 which is 370 nm. The average transmission of the film was nearly 94% in the visible wavelength range. Figure 5-14 shows the plots of best-fit dispersion curves of refractive index and absorption versus wavelength for the film.

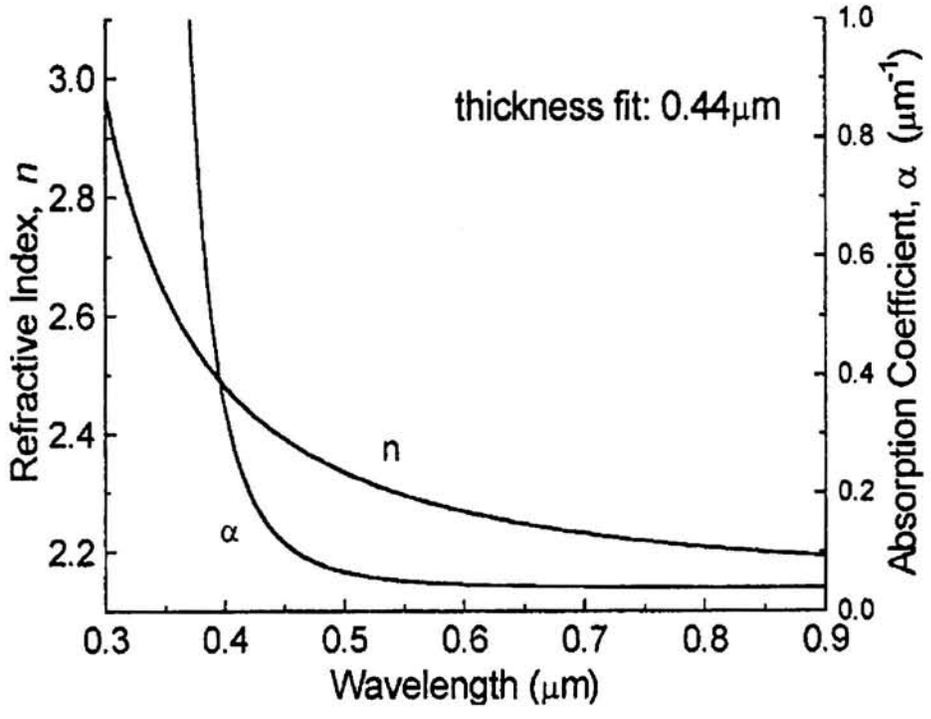


Figure 5-14 Refractive index and absorption coefficient versus wavelength for annealed PLZT 9/65/35 film on sapphire.

In a nonconducting medium, electrons are permanently bound to the atoms comprising the medium. These bound electrons can be considered as classical damped oscillators. In the presence of an applied electromagnetic field such as incidence of light in the medium, the polarization of the electrons (related their displacement) is modified and shows a classical resonance phenomenon. This resonance phenomenon, being related to the absorption of light in the medium, can from Maxwell's equations lead to a description of the index of refraction of the medium. The refractive index $(n^2\text{-}1)^{-1}$ can be represented as function of λ^{-2} in connection with the single-term Sellmeier dispersion formula for one dominant electronic oscillator [11]:

$$n^2(\lambda) - 1 = \frac{S_0 \lambda_0^2}{1 - \lambda_0^2 / \lambda^2} \qquad (5\text{-}4)$$

where S_0 is an average oscillator strength and λ_0 is an average oscillator wavelength obtained from the slope and the 'infinite wavelength' intercept of the extrapolated straight line. For most transparent dielectrics these oscillators (resonant optical frequencies) lie in the UV range. For the PLZT 9/65/35 thin films examined here, the parameters S_o and λ_0 are found to be $7.9\text{x}10^{15}\text{m}^{-2}$ and 0.220 μm, are in good agreement with values reported in reference [11]. The values here are slightly different than those reported for bulk PLZT possibly due to density difference, sincefilms usually have lower densities.

The refractive index of the films extracted from transmittance correlated well with the guided-wave mode index from prism coupling experiments on both as-deposited and annealed films. Figure 5-15 shows the output trace of mode-index measurement where

three TE modes prism coupled into as-deposited PLZT 9/65/35 film on sapphire, using a He-Ne laser with 632.8 nm. $n_{sapphire}$ is given as 1.765 at this wavelength. The thickness of this film was determined to be 0.67 μm and the measured guided-mode refractive index was 2.29 at 632.8 nm. The refractive index was measured to be 2.34 for the annealed (RTA) film [13] and higher at shorter wavelengths (UV), closely matching the bulk PLZT values. The thinner films < 0.4 μm supported only one guided mode and the thickness had to be known to extract the refractive index.

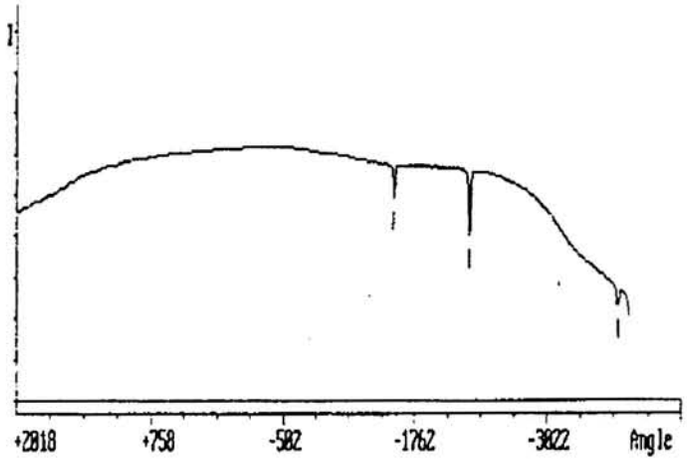


Figure 5-15 Three TE modes prism coupled into as-deposited PLZT 9/65/35 film on sapphire.

5.3 Electrooptic properties of PLZT films

Measurement of the electrooptic (EO) properties of thin film PLZT consists of measuring the refractive indices (from two orthogonal directions) as a function of applied electric field. The largest EO coefficients of PLZT are cross terms, which means we need

to apply a transverse electric field with respect to the light propagation direction. Since we are using thin films, a transverse electric field requires two surface electrodes on the surface of the film, with the space between the electrodes serving as the optical clear aperture.

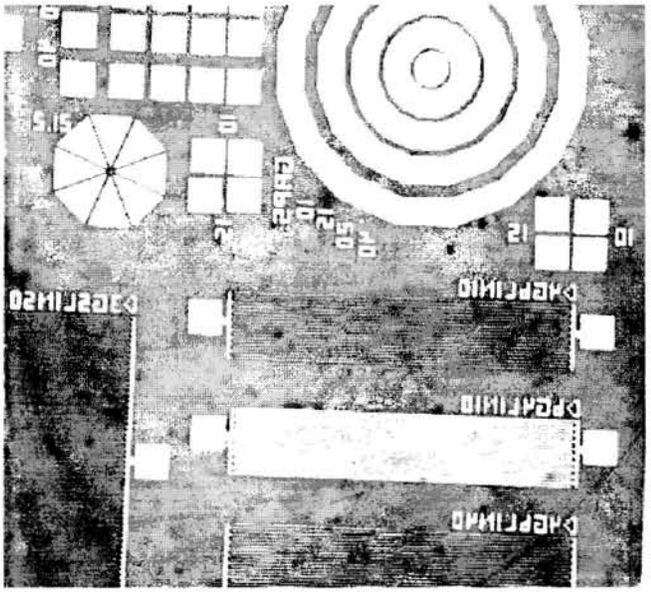


Figure 5-16 Surface electrode (Cr/Au) patterns on a PLZT film on sapphire used for EO measurements.

Figure 5-16 shows an optical micrograph of variety of electrode patterns (Cr/Au) on PLZT/sapphire used in this work. Instead of independently measuring refractive indices in orthogonal directions, an alternative approach is to measure the static isotropic refractive index and the voltage-dependent birefringence of the film. To obtain the electric field-induced birefringence, researchers generally measure the difference in the intensity of

orthogonal polarization states before and after application of the electric field. However, the sensitivity obtained in such measurements of intensity by lock-in amplifiers is poor due to possible intensity fluctuations and thus a better scheme is necessary for measuring the EO effect in thin films especially at low electric fields. Figure 5-17 shows the theoretically minimum thickness required to achieve a retardation change of 0.5° as a function of applied voltage for PLZT film using published EO data by Krishnakumar et al. [4] and bulk PLZT by Kirby [14].

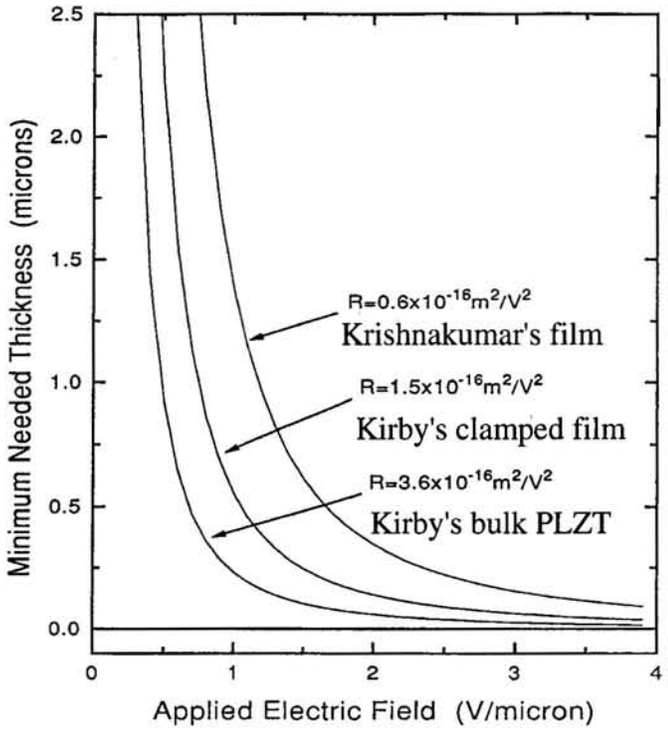


Figure 5-17 Calculated minimum needed film thickness vs. electric field to achieve a retardation of 0.5 degrees.

A high detection sensitivity can be achieved (a retardation sensitivity of 1 nm) by measuring the phase of Young's fringes that are generated by the interference of orthogonal polarizations. The method was used by Nakadate [15] for characterizing waveplates and EO modulators. This method was used in this study for EO characterization of PLZT thin films and a schematic diagram of the experimental setup is shown in Figure 5-18.

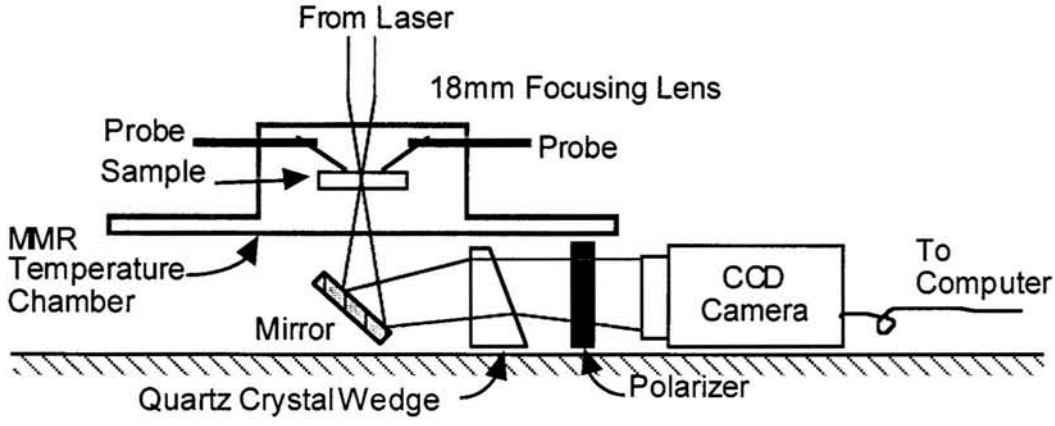


Figure 5-18 Experimental setup used for electrooptic measurements of PLZT thin films.

This EO measurement technique consists of a common-path polarization interferometer as a phase detector of Young's fringes. The setup utilizes a birefringent wedge to create a spatially linear phase difference between two orthogonal polarizations which interfere to form equidistant and straight fringes, called Young's fringes. The phase of these intensity fringes is linearly proportional to the net retardation of the optical

system before the wedge. The signals from the CCD camera are processed by a computer before and after the retarder (sample) to be measured is inserted into the path of laser beam. An argon laser was used in this work, with a wavelength of 514 nm.

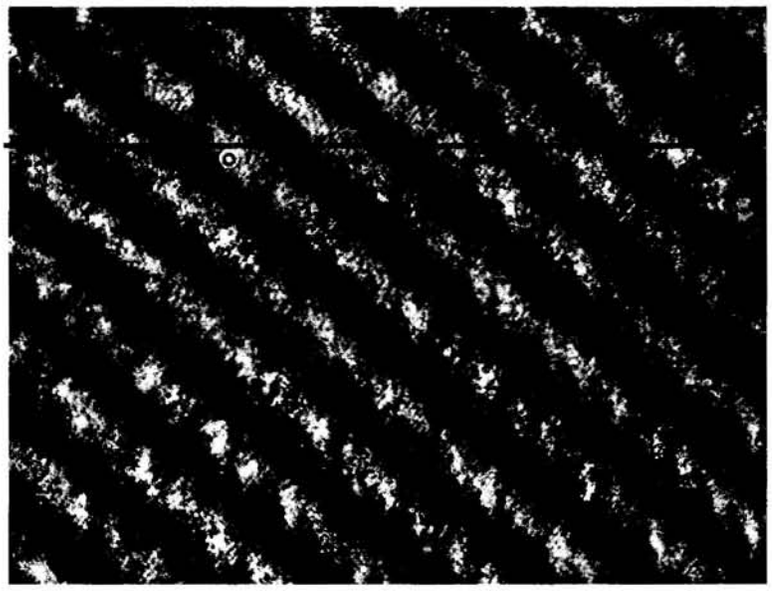


Figure 5-19 Sample intensity pattern obtained with CCD camera. The transect line used for the intensity values is shown on top.

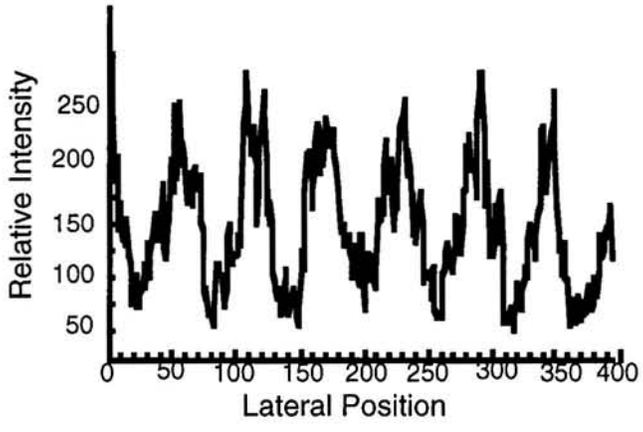


Figure 5-20 Intensity transect values.

The polarization direction of the light beam is aligned 45° with respect to the principal axes of the sample. The optical axis of the birefringent wedge is aligned with one of the principal axes of the retarder, and the output polarizer is aligned 45° with respect to the principal axis of the wedge. A theoretical analysis is presented by Nakadate [15].

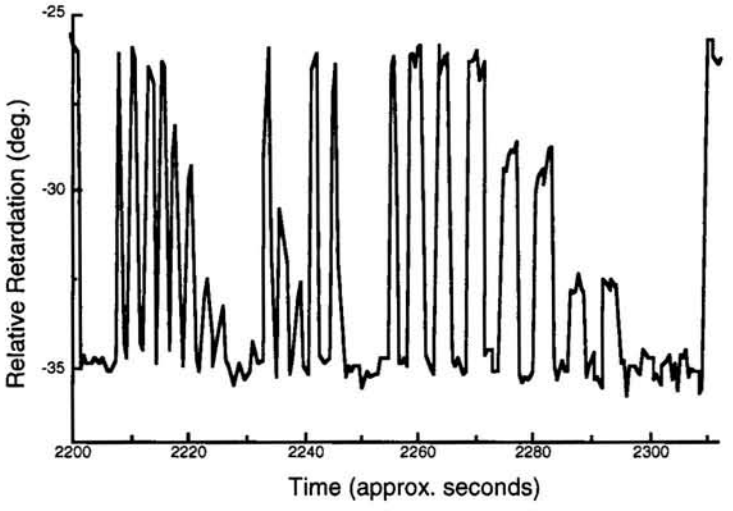


Figure 5-21 Retardation changing as a function of time, as the voltage applied to a PLZT thin film modulator is varied in discreet steps.

The total retardation is a function of birefringence Δn and the path length t according to the relationship; $\Gamma = \Delta n\, t$, where Γ is the total retardation and t is the thickness of the film. After Γ is measured, given the thickness the field-induced birefringence can be calculated for a PLZT film. Using the following equation, R (quadratic EO coefficient) can also be determined at an applied electric field E.

$$\Delta n = - (1/2)\, n^3\, R\, E^2 \qquad (5\text{-}5)$$

A sample intensity pattern obtained with CCD camera is illustrated in Figure 5-19. The transect line used for intensity values is shown on the top and the intensity is plotted as a function of lateral position (Figure 5-20). Figure 5-21 shows the change in retardation as function of time as the voltage (+ and -) applied to a PLZT thin film modulator in discrete steps.

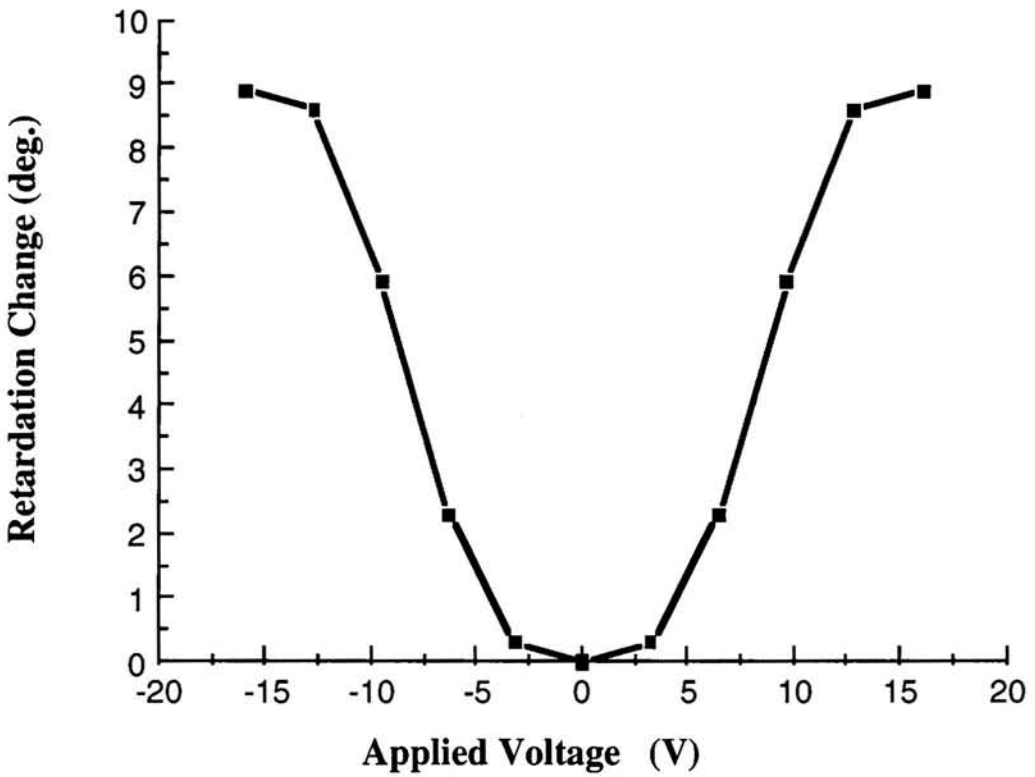


Figure 5-22 Remarkably large electrooptic effect in a 0.6 μm-thick PLZT 9/65/35 film on r-sapphire. The electrode gap was 10 μm.

PLZT thin films (0.6 μm to 0.9 μm) on r-sapphire which were furnace annealed showed EO response dominantly quadratic in nature. The EO response was correlated with processing conditions of the films. For instance, films which were rapid thermally annealed usually showed extremely weak electrooptic effect, corresponding to R = $1.0x10^{-16}m^2/V^2$. This is most likely because of the internal stress and smaller grain size in these films. A PLZT film (0.8 μm) deposited at 450 °C and then furnace annealed to 700°C, exhibited a quadratic effect with an electrooptic coefficient R of ~ $0.7x10^{-16}m^2/V^2$. However, a 0.6 μm PLZT film deposited at 490°C and furnace annealed at 700°C for 20 min exhibited an enormously large electrooptic effect, effectively five times larger than the reported EO effect ($3.8x10^{-16}m^2/V^2$) in bulk PLZT 9/65/35, as shown in Figure 5-22. An extremely symmetric quadratic response is observed in EO effect, reaching a saturation at high electric fields. EO coefficients equal to or slightly larger than the bulk values were reported earlier for PLZT films 7/0/100 on SiO_2 and 9/65/35 on PLT/c-sapphire [16,17] but the responses were very asymmetric and hysteretic. This would pose a serious problem in switching response of the thin film modulators. Krishnakumar et al [4] reported a quadratic EO effect with a coefficient of $0.6x10^{-16}m^2/V^2$ in sputtered PLZT 9/65/35 film on r-sapphire previously. The effective electrooptic effect seen in this study constitutes the largest effect thus reported in electrooptic thin films.

In summary, we studied the effect of post-deposition annealing on the dielectric, optical and EO properties of magnetron sputtered PLZT 9/65/35 films. The values of peak dielectric constant were moderate in the range 800 - 1200 with T_c = 110°C - 130°C

for RTA films and high in the range 1700 - 2800 with higher T_c = 130°C - 190°C for FA films, respectively. The frequency dispersion in dielectric constants of the films were found to be relatively small and dielectric losses were also very low. The dielectric constants and EO coefficients of RTA processed PLZT films were smaller than the corresponding values for FA processed films and this was thought to be due to smaller grain sizes and the presence of residual compressive stresses in the former. Optical transparency of the films were excellent and a very large quadratic EO effect was observed in a 0.6 μm-thick PLZT 9/65/35 film after FA processing.

Next two chapters will study another important electrooptic material, potassium tantalate niobate (KTN), the sol-gel process of KTN and thin films from sol-gel and magnetron sputtering are analyzed.

References

1 G. W. Farnell, I. A. Cermak, P. Silvester and S. K. Wang, "Capacitance and field distributions for interdigital surface-wave transducers," *IEEE Trans. Sonics Ultrason.*, **SU-17**, 188, 1970.

2 H. Adachi, T. Mitsuyu, O. Yamazaki and K. Wasa, "Ferroelectric (Pb,La)(Zr,Ti)O_3 epitaxial thin films on sapphire grown by rf-planar magnetron sputtering," *J. Appl. Phys.*, **60**, 736, 1986.

3 T. Kawano, T. Sei and T. Tsuchiya, "Preparation of ferroelectric (Pb,La)(Zr,Ti)O_3 thin films by sol-gel process and dielectric properties," *Jpn. J. Appl. Phys.*, **30**, 2178, 1991.

4 S. Krishnakumar, V. H. Ozguz, C. Fan, C. Cozzolino, S. C. Esener and S. H. Lee, "Deposition and characterization of thin ferroelectric lead lanthanum zirconate titanate (PLZT) films on sapphire for spatial light modulators applications," *IEEE Ultra., Ferroel., and Freq. Contr.*, **38**, 585, 1991.

5 Y. S. Hwang, S. H. Paek, J. H. Lee, C. S. Park, J. S. Choi, J. K. Jung and Y. N. Kim, "Formation and characteristics of lead lanthanum zirconium titanate thin films formed by using the rf sputtering method," *J. Mater. Sci. : Mater. Elecronics*, **7**, 309, 1996.

6 G. H. Haertling, "An acetate process for bulk and thin film PLZT," Proc. IEEE 7th Intl. Symp. Appl. Ferroelectrics, p. 292, 1990.

7 M. Ishida, H. Matsunami and T. Tanaka, "Preparation and properties of ferroelectric PLZT thin films by rf sputtering," *J. Appl. Phys.*, **48**, 951, 1977.

8 G. Teowee, M. P. Mebes, C. D. Baertlein, E. L. Quackenbush, E. A. Kneer, J. M. Boulton and D. R. Uhlmann, "Compositional tailoring of the dielectric and ferroelectric properties of sol-gel derived PLZT thin films," *Integ. Ferroelectrics*, **10**, 131, 1995.

9 D. E. Dausch and G. H. Haertling, "The domain switching and structural characteristics of PLZT bulk ceramics and thin films chemically prepared from the same acetate precursor solutions," *J. Mater. Sci.*, **31**, 3409, 1996.

10 W. E. Paradise, F. Wang and G. H. Haertling, "Effects of applied stress on the dielectric properties of PLZT thin films," Proc. IEEE 9th Intl. Symp. Appl. Ferroelectrics, p. 785, 1994.

11 J. Krempasky, L. Wang, M. Proctor, A. Pignolet and F. Levy, "Optical properties of PZT and PMZT sputtered thin films," *Solid State Comm.*, **78**, 1039, 1991.

12 M. Born and E. Wolf, Principles of Optics, Pergamon Press, 1987.

13 B. Tunaboylu, P. C. Harvey, F. Deng, C. Fan and S. C. Esener, "Ferroelectric PLZT thin films deposited by rf triode magnetron sputtering for spatial light modulators," Proc. IEEE 10th Int. Symp. Appl. Ferroelectrics, 1996 (in press).

14 C. J. Kirkby, "Electrostriction and strain-optic phenomena in PLZT 9/65/35," *Ferroelectrics*, **37**, 567, 1974.

15 S. Nakadate, "High precision retardation measurement using phase detection of Young's fringes," *Appl. Optics*, **29**, 242, 1991.

16 H. Adachi and K. Wasa, "Basic thin film process for perovskite ferroelectric materials," Mater. Res. Soc. Symp. Proc., vol. **200**, p. 103, 1990.

17 J. F. Roeder, S. M. Bilodeau, P. C. Van Buskirk, V. H. Ozguz, J. Ma and S. H. Lee, "Liquid delivery CVD of PLZT thick films for electro-optic applications," Proc. IEEE 9th Intl. Symp. Appl. Ferroelectrics, p. 687, 1994.

6. KTN

6.1 Background: Crystal properties

Potassium tantalate niobate ($KTa_{1-x}Nb_xO_3$), a continuous solid solution of $KTaO_3$ and $KNbO_3$, is a perovskite ferroelectric with great potential because of its remarkable piezoelectric, pyroelectric and electro-optic properties [1,2,3]. KTN has a large quadratic and linear EO coefficients [4] and has been demonstrated [5] as an efficient EO modulator. The half wave voltage for phase retardation in KTN was seen to be nearly one hundredth of that of KDP (KH_2PO_4) and nearly half of that for $BaTiO_3$ [6]. High sensitivity optical recording/storage in KTN has been demonstrated [7] with a sensitivity more than 5000 times that in $LiNbO_3$ or any other storage medium. Photorefractive effects associated with a large quadratic EO effect in the cubic paraelectric phase as well as in tetragonal phase with dopants have also been observed in KTN, which reflect the holographic storage possibilities [2,8,9]. Finally, light modulation and beam deflection via the large quadratic EO effect in KTN [1] points to it as a leading candidate material along with PLZT for EO light modulator applications.

Besides the EO effect, because of its strong nonlinear dependence of the dielectric constant [10] and high permittivity [8,11] it is being considered for RF/microwave phase shifters. It is also very attractive as a pyroelectric material for uncooled IR detectors due to its extremely large bulk pyroelectric coefficient, p′, 8.0 μCoulombs/cm^{2}K [2] and thin film p′ = 20 μCoulombs/cm^{2}K (bias 3V/μm) , with the largest reported figure-of-merit [12,13].

The Curie temperature (T_c) of KTN (ferroelectric⇔paraelectric transition) and thus its properties can be adjusted with the molar Ta/Nb ratio [14]. High optical quality single crystals of KTN having Curie point near room temperature are not avaliable and therefore its technological potential has not yet been exploited as a bulk material. The as-grown large KTN crystals were mainly handicapped due to striations and compositional gradients and recently some progress has been made to minimize them [11,15,16,17]. The major roadblock, however, in obtaining high quality bulk KTN ceramics and thin films has been the difficulty of getting uniform and stoichiometric potassium contents in the materials. It has been difficult to overcome the K_2O volatilization in hot-pressing (HP) or sinter-forging of KTN ceramics [18,19]. It is known that the vapor deposition methods require very dense targets of stoichiometric and homogeneous KTN in a single phase for optical quality thin films for device applications [19,20]. Because of these issues, part of this study involved investigation of fabricating stoichiometric, chemically uniform and dense KTN ceramic discs for utilization as sputtering targets. Stoichiometric targets from sol-gel derived fine powders were produced by hot-isostatic pressing (HIP). The sol-gel process was used to make fine powders for stoichiometric and uniform ceramic discs as well as thin films from its precursors. The advantages of sol-gel process combined by HIPing over conventional processes are discussed for KTN fabrication in the next chapter.

6.1.1 Phase diagram and crystal structure

KTN ($KTa_{1-x}Nb_xO_3$) is a solid solution of two perovskite materials, potassium tantalate ($KTaO_3$) and potassium niobate ($KNbO_3$) which have nearly the same unit cell size (3.989 Å and 4.021 Å [11]) but very different ferroelectric Curie temperatures $KTaO_3$, T_c = 4 K and $KNbO_3$, T_c = 698 K [14]. The Curie temperature for the cubic (pm3m) - tetragonal (p4mm) transition varies linearly with composition over the range 0 > x > 1, and especially for lower (x = 0.50) values two other phases form in sequence upon cooling, orthorombic and rhombohedral (Figure 6-1 [14]). Therefore, it is possible to tailor the T_c and thus the main properties of KTN.

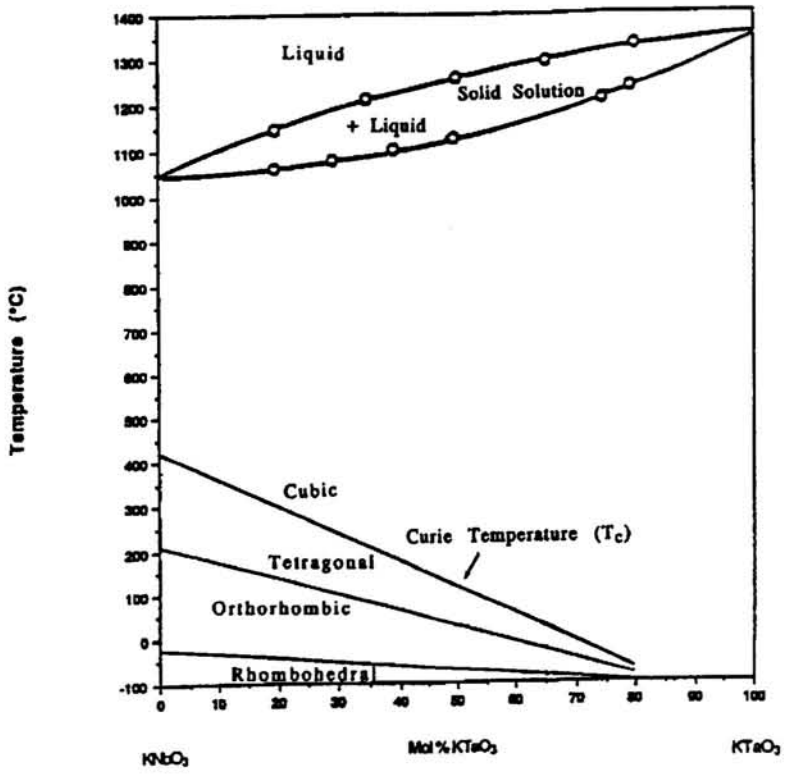


Figure 6-1 Phase diagram of $KTaO_3$- $KNbO_3$ [14].

In the perovskite cubic phase, KTN is optically isotropic and transparent and shows large quadratic electrooptic effect. For the quadratic EO effect in EO light modulators, KTN is best operated at just few degrees above the primary Tc in its paraelectric cubic phase. This is possible by achieving T_c of about 5° to 15°C. From the solid solution transitions in the phase diagram by Triebwasser [14], an approximate T_c can be estimated as a function of the stoichiometry parameter 'x' according to:

T_c (°C) = 435 - 686 x for the primary cubic to tetragonal transition and

T_c (°C) = 210 - 396 x for the secondary tetragonal to orthorombic transition.

Thus the primary T_c for KTN can be continuously changed from nearly -256°C to 437°C, with a near room temperature T_c occurring for $KTa_{.63}Nb_{.27}O_3$. At few degrees above the T_c, KTN is paraelectric (normal nonlinear dielectric of high permittivity) cubic while below T_c it is ferroelectric and shows hysteresis of polarization with electric field. As the 'x' parameter changes, the lattice parameter increases linearly with Nb^{5+} substitution into the B-site of perovskite $KTaO_3$ as seen in Figure 6-2 [11]. This characteristic of KTN which allows its growth on different substrates such as MgO, $SrTiO_3$, Si, GaAs, sapphire.

The single crystal KTN growth have been done by growing small crystals from melt (incongruent nature) usually with excess potassium (K_2CO_3) in the inital molten charge for growth periods of days to obtain cm-size crystals [17]. Figure 6-3 shows the binary phase diagrams of K_2CO_3 versus Nb_2O_5 and Ta_2O_5 [21,22].

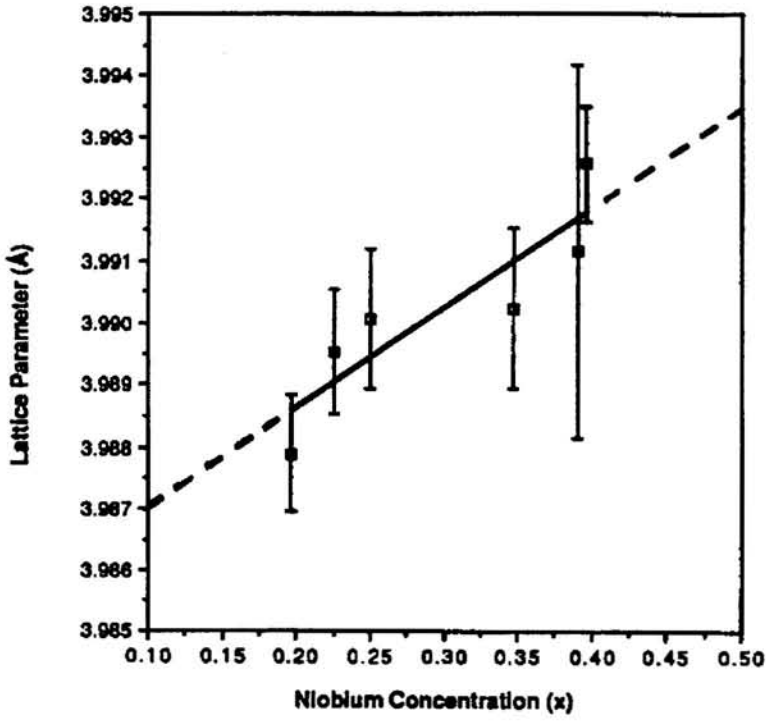


Figure 6-2 Composition dependence of the lattice parameter of $KTa_{1-x}Nb_xO_3$ [11].

Compositional gradients possibly promoted by temperature gradients during cooling of the melts result in crystals with striations which hamper the reproducibility of electrooptic response of KTN and this limits its immediate use as a bulk electrooptic material as compared to PLZT, KDP or $LiNbO_3$. Therefore, the striation-free crystals are needed for EO applications to exploit its remarkable properties. Unfortunately, the hot-pressed KTN does not have the desired transparency due to scattering from grain boundaries and chemical inhomogeneities. Another avenue, of course, is the thin-film growth of KTN which would also ease the packaging requirements in integrating KTN

with IC devices. However, thin film deposition is relatively new and encountering again to the issue of potassium volatility which will be discussed in the forthcoming sections.

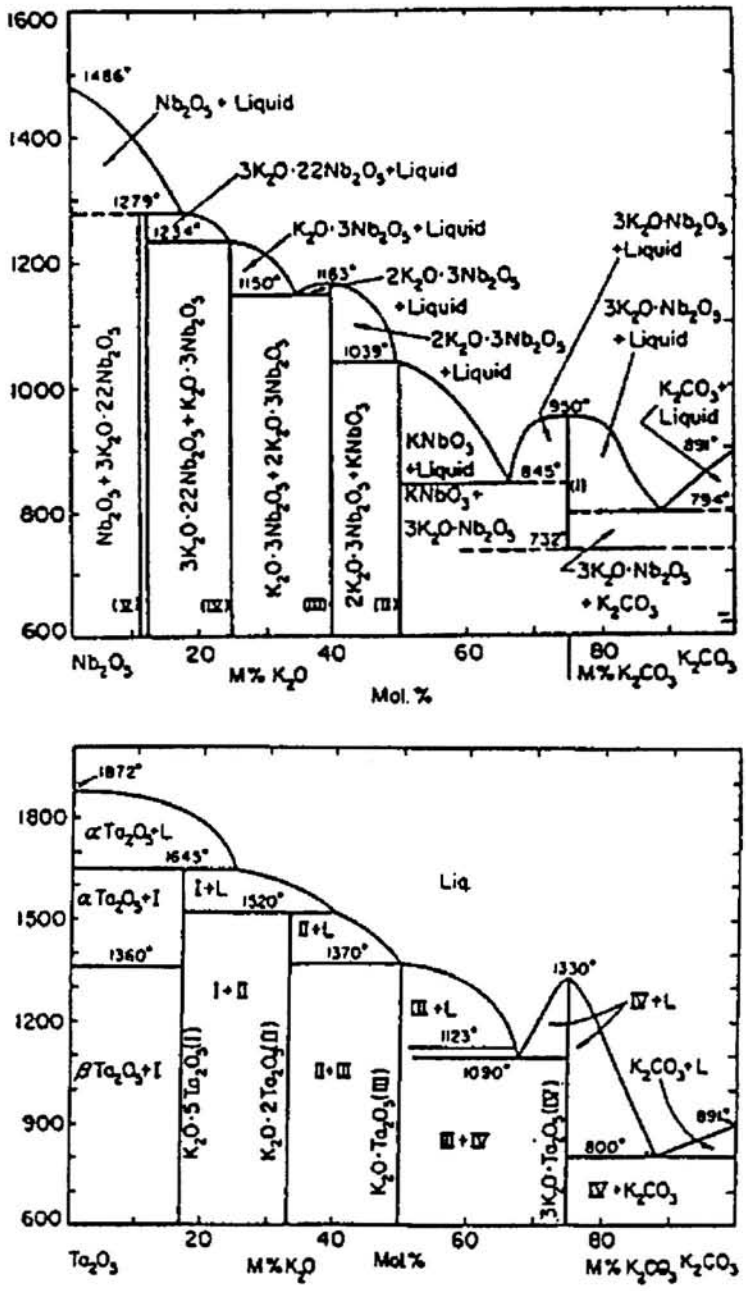


Figure 6-3 Phase diagrams of system K_2O-Nb_2O_5 (a) and K_2O-Ta_2O_5 (b) [21,22].

6.1.2 Dielectric, optical and electrooptic properties of KTN crystals

Figure 6-1 shows the temperatures of transitions observed in KTN crystals and the Curie temperature change. The dielectric transitions are very sharp in KTN and believed to be thermodynamically first-order transition. This makes dielectric constant sensitive to temperature variations as compared PLZT with diffuse phase transitions. The dielectric constant reaches very high values going through the T_c which is explained by the soft phonon modes and follows the Curie-Weiss law in the paraelectric phase. In fact, the T_c is obtained by plotting the inverse of the dielectric constant in paraelectric phase versus temperature and extrapolating the intercept of this line with the temperature axis. The Curie point may shift due to inhomogeneities in the samples of identical composition. Triebwasser [14] made a study in the $KTaO_3$-$KNbO_3$ system and determined that (1) the Curie temperature of KTN decreases with increased $KTaO_3$ content, (2) the peak ε increases with increasing $KTaO_3$ content, and (3) the thermal hysteresis between heating and cooling curves generally decreases with increasing $KTaO_3$ concentration. Figure 6-4 shows the relative dielectric constants of KTN of different 'x' parameter as function temperature [11]. The peak ε value is nearly 19000 for $x = 0.347$ and T_c is observed to be near to 0°C.

The sharp peak in can be very useful in pyroelectric applications where dielectric mode (bolometer mode) is utilized since it can offer large polarization changes (thus, a large p') very near to its transition. Ferroelectric KTN shows spontaneous polarization at room temperature which can be enhanced by poling where most of the dipoles oriented

along a certain direction (electric-field direction). Several different domain structures have been observed by polarizing microscope in orthorombic and tetragonal KTN single crystals [23]. Application of bias fields caused the Curie temperature to shift toward higher temperatures and the value of the dielectric constant at the peak to be reduced [10]. The dielectric loss of KTN crystals were high (tan delta of 0.2-0.6 without bias) at T_c and was reduced similarly upon application of a field.

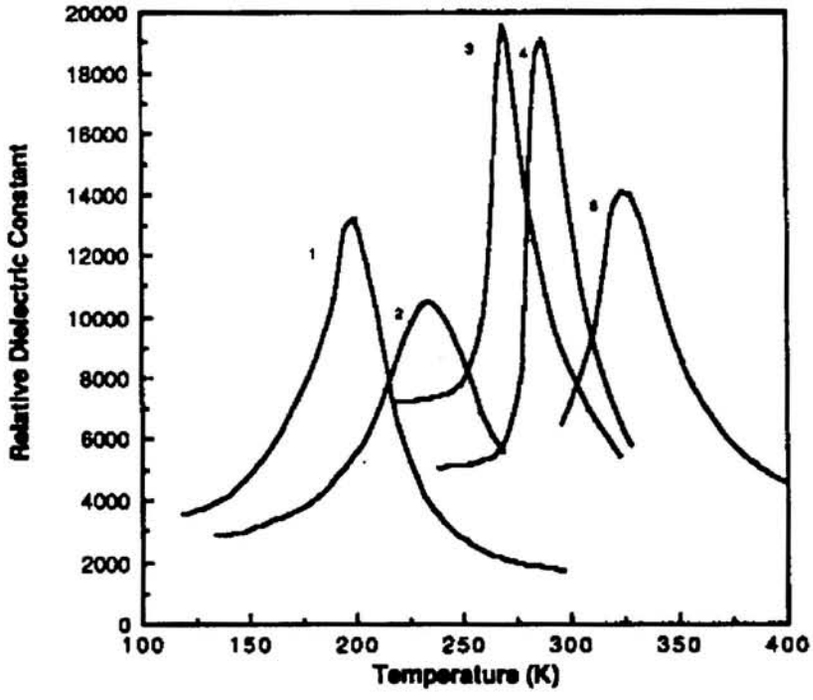


Figure 6-4 Dielectric constant as a function of temperature for $KTa_{1-x}Nb_xO_3$ crystals. Values for x are: 0.226 for 1, 0.249 for 2, 0.347 for 3, 0.391 for 4 and 0.425 for 5 [11].

In KTN crystals with Nb concentrations of 3.5 at% and 15.7 at%, remanent polarization existed well above T_c [24]. This remanent polarization was attributed to off-

center Nb ions. Further changes as a function of frequency (hysteresis behavior) were reportedly shown to be due to the slow relaxation of randomly distributed off-center ions interacting in clusters (polar nanoregions approx. 20 - 100 Å in size). This change in the frequency dependence (lowering with higher frequency) of the system was claimed to reflect a dynamical slowing of the dipoles.

The transmission spectrum of KTN (x = 0.38) is shown in Figure 6-5 [15]. The absorption edge lies at 380 nm and the crystals are transparent in the IR up to 5 μm. The transmission curve with blue coloration represented in the plot is due to oxygen deficiency in the sample with high conductivity.

The tetragonal KTN with symmetry group P4mm (below T_c) is optically negative uniaxial and exhibits birefringence which is measured to be $n_c - n_a = -0.0012$ where n_c and n_a are the refractive indices along c-axis and a-axis of the lattice respectively [4]. Compositions lying at high Ta concentrations are cubic at room temperature with symmetry group Pm3m and optically isotropic. The refractive index is 2.20 at 1.6 μm and goes up to 2.35 at 0.5 μm. The dispersion in the refractive index n is represented by the well-known single-term Sellmeier equation [1]

$$n^2 - 1 = \frac{3.7994}{(1 - \frac{\lambda_s^2}{\lambda^2})} \qquad (6\text{-}1)$$

where λ_s = 201.1 nm. Further anomalous dispersion from transverse optical modes at higher wavelenghts make significant contribution to the equation which can be inserted by adding higher terms in the Sellmeier equation.

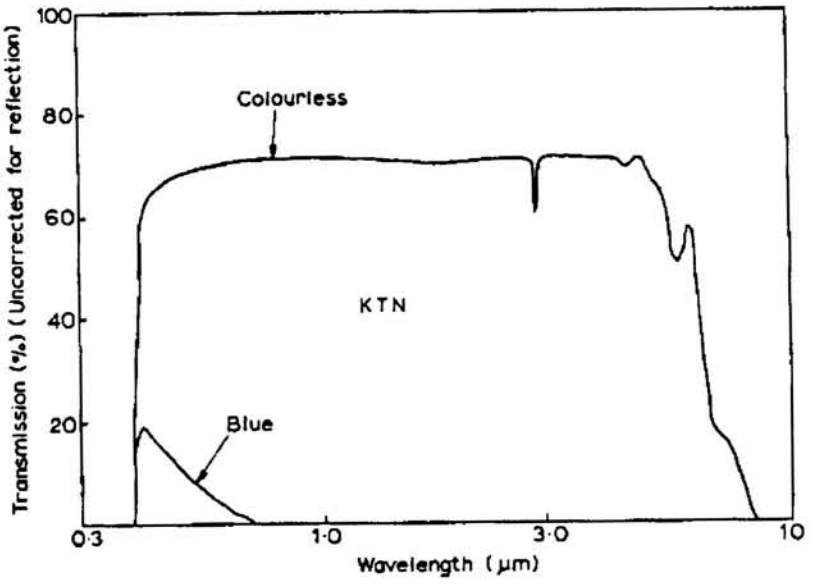


Figure 6-5 Transmission spectrum of KTN crystal [15].

Cubic centrosymmetric paraelectric KTN shows a dominantly quadratic EO coefficients (Kerr effect) in its first-order electrooptic coefficients over the linear EO coefficients. The large coefficients in the paraelectric phase make KTN attractive for transverse light modulators where the light propagates normal to the applied electric-field direction. For a stress-free paraelectric KTN, the optical impermeability tensor under an applied electric field can be described as [25]

$$\eta_{ij}(E) - \eta_{ij}(0) = s_{ijkl}E_kE_l \qquad (6\text{-}2)$$

The electrooptic tensor of cubic KTN is similar to that of cubic PLZT and using the usual contraction of indices and symmetry operations used in chapter 2, leads to the principal refractive index expression for an electric field in perpendicular to light propagation direction (see also Appendix for further information),

$$n_o = n - \frac{n^3 s_{12} E^2}{2} \tag{6-3}$$

$$n_e = n - \frac{n^3 s_{11} E^2}{2} \tag{6-4}$$

The electric-field induced birefringence is given by

$$\Delta n = \frac{n^3}{2}(s_{11} - s_{12})E^2 \tag{6-5}$$

and the phase retardation of the light beam is related to birefringence by the equation

$$\Gamma = \frac{2\pi d \Delta n}{\lambda} \tag{6-6}$$

where d is the thickness of KTN and λ is the wavelength of the light beam. The Γ can be measured directly by Young's fringes method as described in chapter five.

For KTN (Ta/Nb:0.63/0.37) whose Curie temperature is -3°C, the electrooptic coefficients measured at room temperature were [1]

$s_{11} = 22.58 \times 10^{-16}\ m^2/V^2$

$s_{12} = 6.31 \times 10^{-16}\ m^2/V^2$

$s_{44} = 24.4 \times 10^{-16}\ m^2/V^2$

Yariv and Yeh [25] also reported the term as s_{11}-s_{12} = $2890 \times 10^{-18}\ m^2/V^2$ for cubic $KTa_{.63}Nb_{.37}O_3$ at room temperature. However, using smaller EO coefficients from the former reference and assuming an electric field of 2 V/μm, a dielectric constant ε_r of 2000 (room temp.) and n_{ave} = 2.30, the birefringence of cubic paraelectric phase of KTN is calculated to be $\Delta n = 3.95 \times 10^{-2}$. This value is the highest among the ferroelectric materials.

Noncentrosymmetric tetragonal KTN possess dominantly linear EO coefficients (Pockel's effect). It has only three different, non-zero electro-optic coefficients as shown in the following matrix [25]

$$\begin{pmatrix} 0 & 0 & r_{13} \\ 0 & 0 & r_{33} \\ 0 & 0 & r_{33} \\ 0 & r_{51} & 0 \\ r_{51} & 0 & 0 \\ 0 & 0 & 0 \end{pmatrix} \tag{6-7}$$

The tetragonal KTN is suitable for structures using longitudinal effect and especially useful if the KTN film can be deposited on substrates with a-axis lying parallel to the substrate and c-axis normal to substrate and so that electric-field is along a-axis, light propagation normal to the film surface. For this case, the equation for the index ellipsoid in tetragonal KTN can be written as

$$\frac{x^2}{n_o^2} + \frac{y^2}{n_o^2} + \frac{z^2}{n_e^2} + 2zxr_{51}E = 1 \tag{6-8}$$

After transformation of coordinates and extraction of index ellipsoid, the following relations can be obtained

$$n_x = n_o - \frac{n_o^3 r_{51}^2 E^2}{2(\frac{1}{n_o^2} - \frac{1}{n_e^2})} \qquad \text{and} \qquad n_y = n_o \tag{6-9}$$

The birefringence can be calculated from above as $\Delta n = n_y - n_x$. The birefringence is related to phase retardation as given earlier, thus measuring the retardation we can obtain birefringence and the electrooptic coefficients of the films. The linear EO coefficient r_{51} is

reported as $3000x10^{-12}$ m/V [6]. By using this value in the above equation and assuming an applied field of 2 V/m, the electric-field induced birefringence is calculated to be $\Delta n = 3.7x10^{-2}$. This is a large value but smaller than the one calculated for cubic paraelectric KTN ($3.95x10^{-2}$), thus paraelectric compositions with Ta contents more than 62 at% are more desirable for SLMs. Also it has been difficult to grow thin films of KTN with c-axis normal to substrate plane.

Similarly from the equation obtained for index of refraction of $KNbO_3$, the electric-field induced birefringence was derived and calculated assuming again an applied field of 2 V/μm. $KNbO_3$ is orthorombic with $n_1 = 2.280$, $n_2 = 2.329$ and $n_3 = 2.169$ [26].The linear EO coefficient of $KNbO_3$, r_{42}, was reported to be $380\pm50x10^{12}$ m/V [27]. The orthorombic structure however makes it optically biaxial and not particularly useful for SLMs but attractive with its low dielectric constant of 137 for aligned waveguide structures. We calculated the Δn as $0.86x10^{-2}$ using the equations derived by Gunter [27].

The electrooptic coefficients of KTN listed here also include a secondary contribution arising from electrostrictive strain which produces an elasto-optic deformation of the index ellipsoid. This contribution is negligible for frequencies in MHz regime or higher. Because thin films are effectively clamped to the substrate (zero-strain), essentially no crosstalk will exist between modulators due to electrostrictive effects. The electrooptic coefficients of KTN at dc and 100 Mhz have been similar and the frequency response of EO effect in KTN will be limited by dielectric dispersion which was reportedly above 200 Ghz making it feasible for devices operating in millimeter

wavelengths. Rytz et al [28] have done measurements of dielectric constants and loss tangents of paraelectric KTN at frequencies as high as 94 Ghz. Their study suggested that the refractive index of KTN ranged between 15 and 26 while tan δ between 0.006 and 0.06. These results indicate possibilities in KTN for RF microwave components and also fast ferroelectric modulators operating in the GHz regime.

The effective paraelectric EO coefficient of cubic KTN is larger than that of PLZT. The effective birefringence of paraelectric KTN is also larger than its ferroelectric tetragonal counterpart and is also preferable since contrast ratios obtainable in paraelectric phase is better due to negligible hysteresis. However, the dielectric constant of KTN is larger than that of PLZT which translates into higher switching energies for KTN.

6.2 Previous work in KTN thin films

There have been relatively few studies on KTN thin films, early work on its deposition were mainly by sol-gel method and MOD [29,30,31]. However, more recently the deposition was also done by pulsed laser ablation and magnetron sputtering [19,20,32,33]. Although growth and in some cases epitaxy were reported on several substrates including primarily $SrTiO_3$, MgO, platinum, sapphire, $LaAlO_3$ and GaAs, only few studies reported electrical and optical/EO properties. Among the published reports, only the work by Sashital et al [20] using magnetron sputtering and by Yilmaz et al [19] using laser beam ablation reported the EO effect on the KTN films.

Nazeri [34] deposited KTN films by spin-on sol-gel method on platinum and observed a dielectric constant of 700 at room temperature and decreased to 450 after applying a dc bias of 20 V. The observed grain size of the films was around < 0.1 μm. MOD-grown thick ~ 12 μm-films were annealed in almost bulk-like conditions, at 1070-1250°C for 10-60 min. They exhibited significant porosity and grain sizes in the order of 2-3 μm [31] and dielectric constants were as high as 15000 at the peak with a broad phase transition unlike $KTa_{0.64}Nb_{0.40}O_3$ crystals of identical composition.

Laser deposited nominally $KTa_{0.91}Nb_{0.09}O_3$ films also exhibited peak dielectric constants around 10000 at ~ 50K [32]. Films were usually oriented (100) on single crystal (100)$SrTiO_3$, (100)MgO, r-sapphire or GaAs and more random on other substrates like quartz, platinum. Bohac and Kaufmann [35] attempted the growth of single-crystal KTN films on (100)-$KTaO_3$ substrates by liquid phase epitaxy. The absorption was reduced and waveguiding observed in the films by addition of 1-2 mol% TiO_2 to the molten flux during epitaxy. The starting molten solution contained certain ratios of KVO_3, K_2O and $KNbO_3$-$KTaO_3$ mixture, and deposited layers were observed to have much higher Ta than the starting solution. However, no dielectric data or electrooptic properties were reported. A summary of the results of KTN film deposition with different techniques on a number substrates in literature was presented in Table 6-1.

Table 6-1 KTN thin films deposited on different substrates.

Substrate	Method of Deposition	Preferred Orientation	Phase(s), PE/PY
$SrTiO_3$ (100, 110)	sol-gel, laser beam ablation, ion beam deposition, RF-sputtering	(100, 110)	PE
MgO (100)	sol-gel	(100)	PE
Pt (poly)	sol-gel, MOD	NPO	PE
*Pt/Si (100)	sol-gel	PO	PE/PY
Si (111, 100)	sol-gel, sputtering	NPO	PY
*GaAs (100)	RF-Mag. sputtering	(100)	PE, PY
*R-Sapphire (1102)	sol-gel, RF-Mag. sputtering	(100)	PE, PY
C-Sapphire (0001)	sol-gel	NPO	PE/PY

*** Substrates used in our work**

Although pyrochlore ($K_2Ta_2O_6$) formation was noted to be a problem, the main roadblock is the potassium deficiency at the deposition temperatures for all deposition techniques used in the studies. When low deposition temperatures used as in chemical deposition methods, then an annealing was required to obtain perovskite at elevated temperatures 700°C or above which triggered potassium (K) evaporation. K-deficiency was addressed by either annealing films either at K-rich atmospheres [31] or depositing from K-enriched targets in oxygen environments for laser-ablation [19,32]. However,

stoichiometric perovskite films were not obtainable reproducibly which would show bulk-like electrical and EO characteristics.

Potassium deficiency leads to porosity in the films leading to reduction in transparency as well as secondary phase formation and a broader phase transition as a function temperature [19,32,33]. The deficiency is usually considered to be accountable for poor electrical and optical characteristics.

As it will be discussed in detail in the forthcoming chapter, potassium deficiency in the KTN films is not solely due to evaporation during or post-deposition processing but also due to a nonstoichiometric target to start with. For successful deposition of optical quality stoichiometric KTN films, the sputtering target has to possess uniform, stoichiometric composition or higher potassium content. Therefore, we developed a sol-gel process to reproducibly derive fine, stoichiometric KTN powder over conventional methods to fabricate uniform stoichiometric targets and finally densified them into discs by HIPing. In this study, KTN films were deposited by both spin-on sol-gel and magnetron sputtering. Sol-gel processing had a dual purpose in that both fine stoichiometric KTN powders were produced as well as solutions which were precursors for spin-on. In the next chapter, we discuss the sol-gel process which was developed to make fine powders with stoichiometric and excess potassium contents and HIP process to fabricate targets and finally spin-on thin films. In addition, we present and discuss the results from magnetron sputtered films obtained using sol-gel derived and HIPed KTN targets in the next chapter.

References

1 F. S. Chen, J. E. Geusic, S. K. Kurts, J. G. Skinner and S. H. Wemple, "Light modulation and beam deflection with potassium tantalate niobate crystals," *J. Appl. Phys.*, **37**, 388, 1966.

2 O. M. Stafsudd and M. Y. Pines, "Characteristics of pyroelectric detectors," *J. Opt. Soc. Am.*, **62**, 1153, 1972.

3 R. Orlowski, L. A. Boatner and E. Kratig, "Photorefractive effects in the cubic phase of potassium tantalate niobate," *Opt. Commun.*, **35**, 45, 1980.

4 W. Haas and R. Johannes, "Linear electrooptic effect in potassium tantalate niobate crystals," *Appl. Opt.*, **6**, 2007, 1967.

5 A. J. Fox, "Nonlinear longitudinal KTN modulator," *Appl. Opt.*, **14**, 343, 1975.

6 J. A. Van Raalte, "Linear electrooptic effect in ferroelectric KTN," *J. Opt. Soc. Amer.*, **57**, 671, 1967.

7 D. von der Linde, A. M. Glass and K. F. Rodgers, "High-sensitivity optical recodring in KTN by two-photon absorption," *Appl. Phys. Lett.*, **26**, 22, 1975.

8 V. Leyva, A. Agranat and A. Yariv, "Fixing of a photorefractive grating in $KTa_{1-x}Nb_xO_3$ by cooling through the ferroelectric phase transition," *Opt. Lett.*, **16**, 554, 1991.

9 S. Loheide, S. Riehemann, R. Pankrath and E. Kratzig, "Influence of Fe doping on the photorefractive properties of $KTa_{1-x}Nb_xO_3$," *Ferroelectrics*, **160**, 213, 1994.

10 A. F. Dugan and W. M. Doyle, "Field-dependent dielectric properties of $KTa_{1-x}Nb_xO_3$," *IEEE Trans. Electron Dev.*, **ED-16**, 522, 1969.

11 K. W. Goeking, R. K. Pandey, P. J. Squattrito, A. Clearfield and H. R. Beratan, "Temperature gradient transport growth of potassium tantalate niobate $KTa_{1-x}Nb_xO_3$ single crystals," *Ferroelectrics*, **92**, 88, 1989.

12 N. W. Schubring, J. V. Mantese, A. L. Micheli, A. B. catalan and R. J. Lopez, "Charge pumping and pseudopyroelectric effect in active ferroelectric relaxor-type films," *Phys. Rev. Lett.*, **68**, 1778, 1992.

13 B. M. Kulwicki, A. Amin, H. R. Beratan and C. M. Hanson, "Pyroelectric imaging," Proc. IEEE 8th Int. Symp. Appl. Ferroelectrics, p. 1, 1992.

14 S. Triebwasser, "Study of ferroelectric transition of solid-solution single crystal of $KNbO_3$-$KTaO_3$," *Phys. Rev.*, **114**, 63, 1959.

15 P. W. Whipps, "Growth of high-quality crystals of KTN," *J. of Crystal Growth*, **12**, 120, 1972.

16 V. A. Kandur and R. K. Pandey, "Crystal growth and properties of potassium tantalate niobate, $KTa_{1-x}Nb_xO_3$, ferroelectric," *Ferroelectrics*, **158**, 55, 1994.

17 T. Imai, S. Yagi, Y. Sugiyama and I. Hatakeyama, "Growth of potassium tantalate niobate single crystal fibers by the laser-heated pedestal growth method assisted by a crystal cooling technique," *J. Crystal Growth*, **147**, 350, 1995.

18 P. E. Debely, P. Gunter and H. Arend, "Preparation and electrooptic properties of the hot-pressed potassium niobate-tantalate ceramic," *Ceram. Bull.*, **58**, 606, 1979.

19 S. Yilmaz, R. Gerhard-Multhaupt, W. A. Bonner, D. M. Hwang, A. Inam, J. A. Martinez, T. S. Ravi, T. Sands, B. J. Wilkens, X. D. Wu and T. Venkatesen, "Electro-optic potassium-tantalate-niobate thin films prepared by pulsed laser deposition from segmented pellets," *J. Mater. Res.*, **9**, 1272, 1994.

20 S. R. Sashital, S. Krishnakumar and S. Esener, "Synthesis and characterization of rf-planar magnetron sputtered $KTa_{1-x}Nb_xO_3$ thin films," *Appl. Phys. Lett.*, **62**, 2917, 1993.

21 A. Reisman and F. Holtzberg, "Phase equilibria in the system K_2CO_3-Nb_2O_5 by the method of differential thermal analysis," *J. Am. Chem. Soc.*, **77**, 2115, 1955.

22 A. Reisman, F. Holtzberg, M. Berkenbilt and M. Berry, "Reactions of the group VB pentoxides with alkali oxides and carbonates. III. Thermal and x-ray diagrams of the system K_2O or K_2CO_3 with Ta_2O_5 ," *J. Am. Chem. Soc.*, **78**, 4514, 1956.

23 X. R. Huang, S. S. Jiang, X. Y. Xu, J. Y. Wang, Q. C. Guan, J. H. Jiang and D. Deng, "Ferroelectric domain structures and phase transitions in crystals," *Phys. Stat. Sol.*, **148**, 611, 1995.

24 L. A. Knaus, B. E. Vugmeister and J. Toulouse, "Polarization switching and long-time relaxation effects in $KTa_{1-x}Nb_xO_3$ and $K_{1-y}Li_yTaO_3$," *Ferroelectrics*, **157**, 251, 1994.

25 A. Yariv and P. Yeh, Optical Waves in Crystals, Wiley-Interscience Publication, 1984.

26 E. Wiesendanger, "Optical properties of $KNbO_3$," *Ferroelectrics*, **1**, 141, 1970.

27 P. Gunter, "Electro-optical properties of $KNbO_3$," *Opt. Commun.*, **11**, 285, 1974.

28 D. Rytz, M. B. Klein, B. Bobbs, M. Matloubian and H. Fetterman, "Dielectric properties of $KTa_{1-x}Nb_xO_3$ at millimeter wavelengths," *Jap. J. Appl. Phys.*, **24-Suppl. 2**, 1010, 1985.

29 S. Hirano, T. Yogo, K. Kikuta, T. Morishita and Y. Ito, "Preparation of potassium tantalate niobate by sol-gel method," *J. Am. Ceram. Soc.*, **75**, 1701, 1992.

30 A. Nazeri and M. Kahn, "Preparation of $KTaO_3$ and $KNbO_3$ solid solutions through sol-gel processing," *J. Am. Ceram. Soc.*, **75**, 2125, 1992.

31 J. V. Mantese, A. L. Micheli, N. W. Schubring, A. B. Catalan, Y. L. Chen, R. A. Waldo and C. A. Wang, "Characterization of potassium tantalate niobate films formed by metalorganic deposition," *J. Appl. Phys.*, **72**, 615, 1992.

32 H. B. Cherry, E. E. Haller, R. P. Reade, J. W. Beeman, G. S. Hubbard and R. E. Mc Murray, Jr., "Potassium tantalate niobate thin films for spaceborne pyroelectric detectors," *Integ. Ferroelectrics*, **15**, 261, 1997.

33 C. M. Cotell and R. E. Leuchtner, "Phase composition and microstructure as a function of deposition conditions for potassium tantalate niobate thin films grown by pulsed laser deposition," Mater. Res. Soc. Symp. Proc., vol. **285**, p. 367, 1993.

34 A. Nazeri, "Crystallization of sol-gel deposited potassium-tantalate-niobate thin films on platinum," *Appl. Phys. Lett.*, **65**, 295, 1994.

35 P. Bohac and H. Kaufmann, "KTN optical waveguides grown by liquid-phase epitaxy," *Electronics Lett.*, **22**, 861, 1986.

7. This work : Synthesis of sol-gel KTN and deposition of KTN films by sol-gel and magnetron sputtering

It is known from the previous work that the vapor deposition methods require very dense targets of stoichiometric and homogeneous KTN in a single phase for optical quality thin films for device applications [1,2]. Therefore, we developed a sol-gel process to reproducibly derive fine, stoichiometric KTN powder over conventional methods to fabricate uniform stoichiometric targets and finally densified them into discs by HIPing.

In this study, KTN films were deposited by both spin-on sol-gel and magnetron sputtering. Sol-gel processing had a dual purpose in that both fine stoichiometric KTN powders were produced as well as solutions which were precursors for spin-on. In the next section, we discuss the sol-gel process which was developed to make fine powders with stoichiometric and excess potassium contents and HIP process to fabricate targets and finally spin-on thin films. In addition, we present and discuss the results from magnetron sputtered films obtained using sol-gel derived and HIPed KTN targets in this chapter.

Homogeneous KTN solutions were prepared using potassium acetate and metal alkoxides in 2-methoxyethanol by controlled hydrolysis with 1:2 (KTN/H_2O) molar ratio. We report on the synthesis of sol-gel KTN for both the fabrication of homogeneous, dense and stoichiometrically correct ceramic discs and deposition and characterization of spin-on thin films as well as sputtered thin films. For the first time, sol-gel derived pure

and homogeneous powders were densified successfully by hot isostatic pressing (HIP) into bulk KTN ceramics, circumventing the potassium deficiency. The spin-on KTN films on Pt/Si or r-sapphire were polycrystalline and stoichiometric, however, sputtered films on r-sapphire were fully (100) oriented and polycrystalline on GaAs substrate with some potassium deficiency. The refractive indices of sputtered dense KTN films on sapphire were between 2.00 and 2.05 in the wavelength range of 800 to 1150 nm.

7.1 Sol-gel derived KTN

7.1.1 Sol-gel synthesis

Sol-gel processing of ceramics offer many advantages such as excellent compositional control, homogeneity on the molecular level due to mixing of liquid precursors, high purity and fine particle size and usually lower processing temperatures over conventional methods. Hot pressing (HP) of sol-gel derived KTN powders resulted in more homogeneous materials [3]. Metal alkoxide processing of potassium niobate, potassium tantalate and their solid-solution powders and spin-coated KTN thin films primarily on MgO, $SrTiO_3$ and Pt have been previously reported [4,5,6].

In this section we report on the synthesis of sol-gel KTN for both the fabrication of homogeneous, dense and stoichiometrically correct ceramic discs and the deposition of thin films from precursor solutions. The hot isostatic pressing (HIP) process used for densification is also described. Unlike HP, sintering or sinter-forging, the HIPping benefits from a uniform hydrostatic pressure and a closed atmosphere where elemental

volatilization can be totally avoided. The results of spin-coated sol-gel KTN thin films on various substrates are also presented.

The basic principle of the sol-gel process is to form a solution of the elements of the desired compound in an organic solvent, polymerize the solution to form a gel and dry and fire this gel to displace the organic components and form a final inorganic oxide. Important and typical precursors for making sol-gel solutions are alkoxides of the general composition M(O-R)n, where R is an alkyl radical (CH_3, C_2H_5, etc.). Their properties and reactions affect the preparation process and determine the product features. Inorganic and organic salts can also be used for introducing some oxides into multicomponent systems. The prescursors are dissolved in a suitable organic solvent to form the solution. In order to get a solution with high concentration of the necessary components and proper viscosity, surface tension and boiling point, the solvent must be carefully selected.

In order to obtain suitable solution for making thin films, various properties of the solution are adjusted. Different alkoxides of different elements show a wide range of reactivity toward water which makes the preparation of multicomponent homogeneous systems difficult also presents difficulties with premature gelation during film processing. In general, metal alkoxides are popular precursors because they react readily with water. They hydrolyze to hydroxides:

$$M(OR)_n + nH_2O \rightarrow M(OH)_n + nROH \qquad (7\text{-}1)$$

then polymerized to form the following oxides:

$$M(OH)_n + M(OH)_n \rightarrow 2MO_{n/2} + nH_2O \quad (7\text{-}2)$$

$$M(OH)_n + M(OR)_n \rightarrow 2MO_{n/2} + nROH \quad (7\text{-}3)$$

By hydrolysis and condensation of alkoxides a polymeric product is formed, leading to the gelation of the solution. To some extent it may be possible to control the degree of gelation using the proper amount of water. Other parameters which have been found empirically to affect the gelation process are solvent, temperature, complex ligands and pH value, although the method and rate of water addition are also very important.

7.1.2 Experimental : Preparation of the precursor solutions of KTN

Potassium acetate (KOAc = $KOOCCH_3$) was chosen as the source of potassium for the KTN solutions since the mixing of the metal (Ta and Nb) alkoxides with potassium ethoxide followed by hydrolysis suffered from irreproducible loss of potassium [4]. Tantalum ethoxide $Ta(OC_2H_5)$, and niobium ethoxide $Nb(OC_2H_5)$, and 2-methoxyethanol ($CH_3OCH_2CH_2OH$) as the solvent were used for the preparation of KTN precursor solutions. Anhydrous 2-methoxyethanol (2-ME) was used instead of ethanol, due to its extremely low water content of 0.003%. The process was done under dry nitrogen atmosphere conditions to avoid uncontrolled hydrolysis due to extreme moisture-sensitivity of compounds used. The potassium acetate (99.98% purity) was dissolved in 2-ME to form a 0.4 molar solution by constantly stirring it at 120 °C for 24 h. An appropriate molar ratio of tantalum ethoxide (99.999%) and niobium ethoxide (99.999%) were mixed in 2-ME while stirring the solution and holding it at 50 °C for 4 h to prepare a

0.375 molar solution. The KOAc and the metal ethoxide solutions were then mixed together with constant stirring at 80 °C for 24 h. Distilled water mixed with 2-ME (1:10 H_2O/2-ME) was added to controllably hydrolyze and then polymerize the solution while stirring at room temperature for 24 h, followed by a cycle at 85 °C for 3 days. A molar ratio of 1:2 (KTN/H_2O) was adopted after testing certain ratios. The homogeneous coating solution was prepared then after concentrating it at 124 °C, the refluxing it, in N_2 atmosphere. The refluxing at 124 °C is necessary for gel formation.

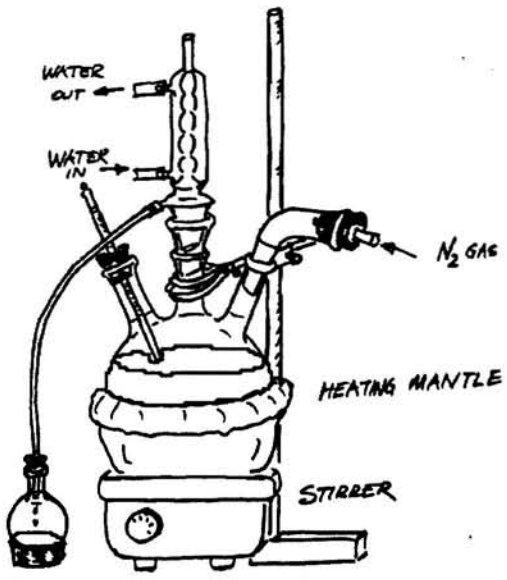


Figure 7-1 Experimental setup for sol-gel synthesis of KTN.

The KOAc coupling with $M(OEt)_5$, ($M = Ta_{1-x}Nb_x$) produces an ester, (EtOAc, ethyl acetate), during dissolution at 80°C while KOH coupling produces alcohol [4]:

$$KOH + M(OEt)_5 \rightarrow K\text{-}O\text{-}M(OEt)_4 + EtOH \qquad (7\text{-}4)$$

$$KOAc + M(OEt)_5 \rightarrow K\text{-}O\text{-}M(OEt)_4 + EtOAc \quad (7\text{-}5)$$

Therefore, the dissolution process has to be carried out in a closed environment such as glove box because of potentially hazardous nature of ester. The following sketch illustrates the experimental set-up we devised for the sol-gel synthesis of KTN (Figure 7-1).

7.1.3 Calcination and annealing

The powder was obtained by first precalcination at 150 °C in air for 4 h followed by grinding the aggregates into small particles by a mortar and pestle. Afterwards the ground powders were calcined in air at 600 °C for 10 h for the burn-out of organics and finally the powder was annealed at 800 °C in high purity O_2 gas (2 lt./min.) for 2 h to obtain completely carbon-free white KTN powder in big quantities. The annealed powder was then further ground by ball-milling (ZrO_2 media) and passed through a 100 mesh sieve to get fine KTN powders necessary for HIP cycles. The average particle size was smaller than 0.5 μm. The pyrolysis process was analyzed by differential thermal analyzer (DTA) up to 1000 °C using a 10 °C/min. heating rate. X-ray diffraction (XRD) was used to determine the phase transformations and the crystal structures. The composition was analyzed by the electron microprobe and the microchemical analysis by energy dispersive X-ray microanalysis (EDS). Scanning electron microscope (SEM) was used to observe the particle morphology and size.

7.1.4 Hot isostatic pressing (HIP)

HIPing technique was utilized for KTN bulk ceramic fabrication mainly to avoid K_2O volatilization problem and ensure the uniformity and homogeneity. To introduce excess potassium into the discs, potassium superoxide (KO_2) was added at certain quantities to obtain 5 at% K to 100 at% K in the powder by mixing the sol-gel derived powder and KO_2 by ball-milling in sealed containers. The HIPping process was as follows: Powders were cold-pressed into a preformed compact at 133 MPa in dry inert atmosphere to finally form (1) 25.4 mm, (2) 101.6 mm in diameter, 6.35 mm-thick discs. The preformed compact was encapsulated with stainless steel, sealed and then welded. The proper encapsulant liner for KTN powder was found to be boron nitride. The encapsulated compact was preHIPed at 700 °C under 33 MPa for 1 h to impart higher green densities prior to full consolidation. The temperature and pressure were then raised simultaneously to HIPing conditions, 1250 °C and 167 MPa, respectively and for a duration of 3 h in dry Ar or O_2 environment. The pressure was released while the sample was at 900 °C to avoid macrocracking. Subsequently, the sample was cooled to room temperature with a 5°C/min cooling rate. Finally, the consolidated pellet was machined out of the can.

7.1.5 Preparation of thin films

KTN thin films were prepared by spin-coating the precursor solution of 0.2 - 0.4 molar concentration with a spin speed of 3000 rpm on sapphire and silicon or Pt/Si substrates. After spin-on, the samples were dried at 120 °C for 1 min on hot-plate in air and then further dried at 200 °C for 10 min in an oven. The pyrolysis was done at 300 - 350 °C in O_2 or H_2O/O_2 gas mixture for 30 - 40 min and then final annealing to crystallize films was carried out at 600 - 750 °C in O_2 atmosphere for 1 h in a furnace. Alternatively, thin films were crystallized by rapid thermal annealing, at 600 - 750 °C for 30 to 90 sec under N_2 flow. The films were coated in many layers sequentially to build up thickness.

Table 7-1 KTN precursor and its hydrolysis with water.

KTN Molarity (mol/L)	**KTN:H_2O**	**Stability - physical changes**
0.75	1:4	cloudy, precipitation
0.75	1:2	cloudy
0.375	1:2	clear
0.375	1:4	cloudy, precipitation

Precursor solutions prepared with potassium acetate in 2-ME were dark yellow and clear before refluxing. Some solutions came out cloudy or contained fine precipitates after

refluxing and hydrolysis depending on the molarity of the solution as well as the molar ratio of KTN:H_2O. No chemical modifiers were added to avoid unintentional prehydrolysis. 0.4 molar precursor solutions prepared with water contents of 1:2 (KTN:H_2O) turned out transparent and homogeneous and had a shelf life of at least two years provided they were properly sealed. The KTN solutions prepared with KOAc in ethanol, however, came out cloudy and showed precipitation as reported earlier [6]. Table 7-1 reflects 0.06 mole KTN solutions hydrolyzed with different amounts of water.

7.1.6 Thermal analysis and crystallization of powders

Figure 7-2 shows the DTA spectrum of KTN powders of composition $KTa_{.10}Nb_{.90}O_3$. The broad endothermic peak, at around 180 °C, results from the evaporation of adsorbed water and residual solvent. There are nearly six notable exothermic peaks which are thought to be associated with pyrolysis (burnout) of organics or crystallization of the amorphous powder. The large exothermic peak at 446 °C indicates the onset of crystallization of powders whose exact temperature depends on the molarity and water content used in the precursor and also of CO_2 evaporation. The exothermic double-peaks at 643 °C and 682 °C are attributable to pyrolysis since it was found by XRD that the perovskite phase forms at temperatures below 600 °C. The first of the double-peak is probably due to $KTa_{1-x}Nb_xO_3.nH_2O$ and burn-out goes to completion at 682°C. The XRD of KTN powders annealed at 500 °C in air indicates partial crystallization as seen in Figure 7-3.

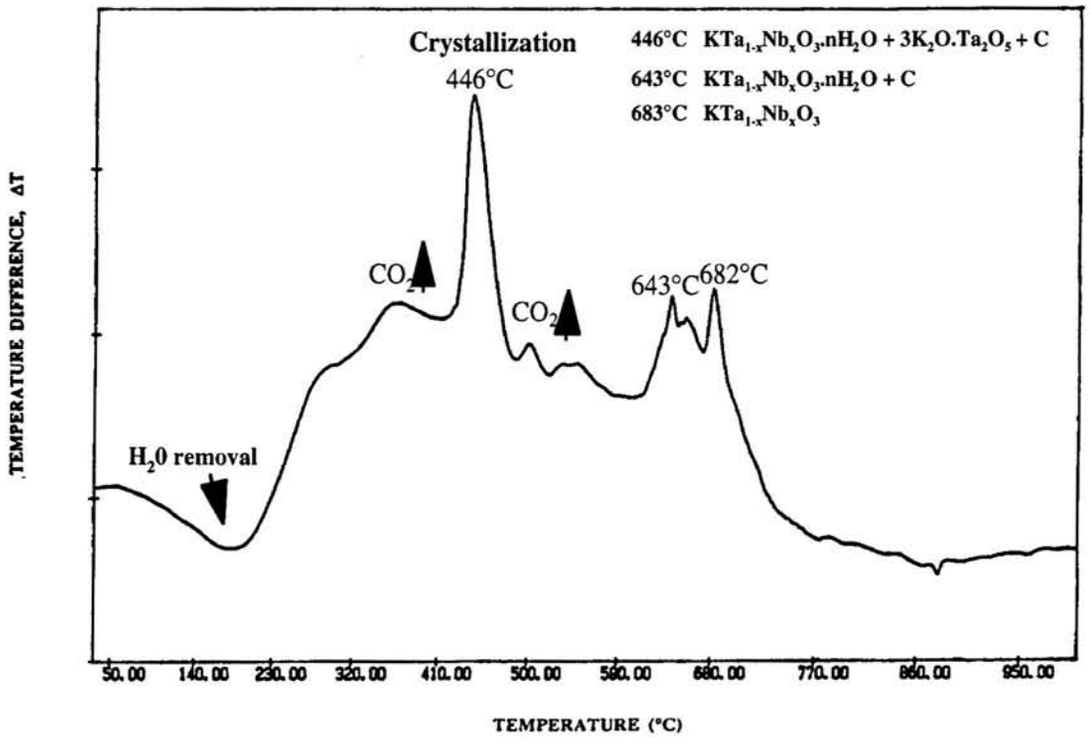


Figure 7-2 DTA spectrum of sol-gel KTN powder. The heating rate: 10°C/min, atm: air.

It was reported that only pyrochlore phase formed when sol-gel derived KTN powders were annealed at 650 °C [5,6]. In contrast to these reports, we observed the full perovskite phase formation taking place with a small pyrochlore remaining after annealing at 600 °C in O_2 for 1 h. However, the annealing in air did not result in similar transformations, necessitating higher annealing temperatures. The complete carbon burnout required oxygen annealing atmospheres as the pyrolysis proceeds much slower in air at annealing temperatures. The pyrochlore that usually formed was found to be $K_2Ta_2O_6$. The KTN powders annealed below 750 °C in air had gray color due to

remaining carbon in them. On the other hand, a two-step anneal was used to anneal large batches of KTN powder (>30 g) since the combustion of organics can take place at high annealing temperatures in oxygen environment.

Figure 7-4 shows XRD spectrum of fully perovskite KTN ($KTa_{.64}Nb_{.36}O_3$) white powder which was obtained by annealing in air for 10 h at 600 °C and in oxygen at 800 °C for 2 h. Long exposures to oxygen or air at 800 °C causes potassium deficiencies, up to 1 - 8 at% K, in KTN powders as determined by electron microprobe. Therefore, the addition of excess potassium into the KTN precursor and thus to KTN powders was tested. The preliminary results show that perovskite KTN with a trace amount of K_3NbO_4 form after powder annealing (Figure 7-5). The powder indicated a composition of $K_{1.13}Ta_{.66}Nb_{.34}O_3$ by microprobe from a KTN starting precursor composition of Ta/Nb (64/36), with 15 at% K excess.

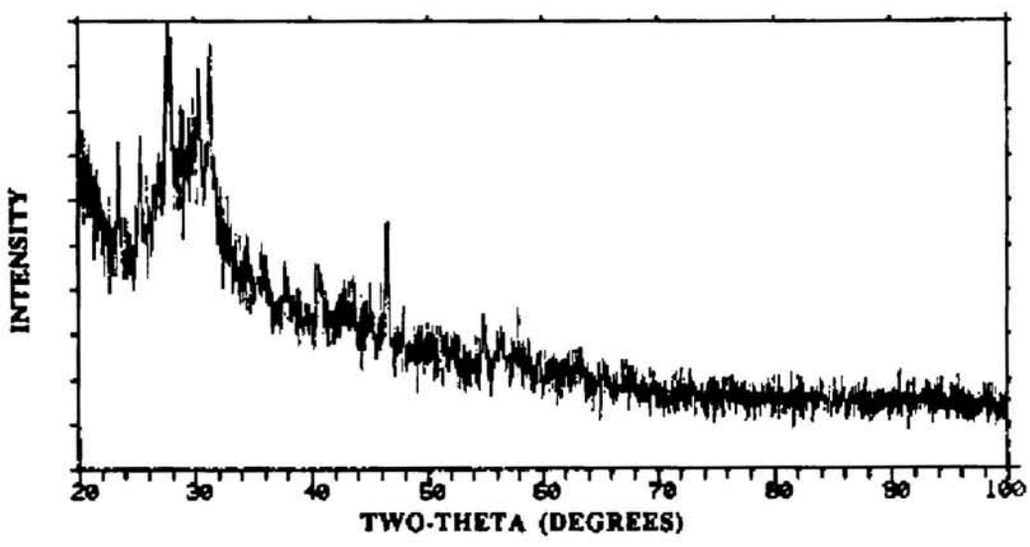


Figure 7-3 X-ray diffraction of KTN (10/90) sol-gel powder annealed at 500°C in air.

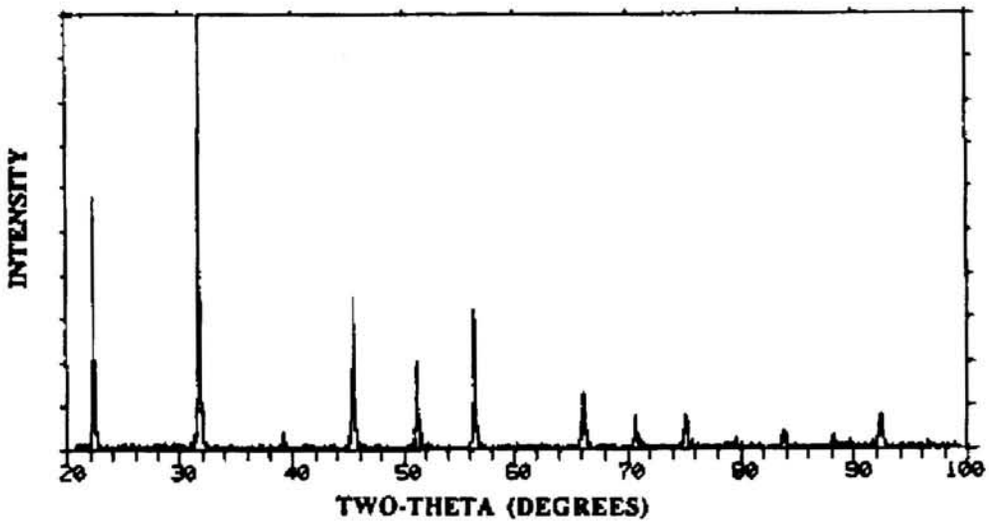


Figure 7-4 X-ray diffraction pattern of KTN (64/36) sol-gel powder annealed at 600°C in air for 10 h, followed by an anneal at 800°C in O_2 for 2 h. All peaks belong to the perovskite phase.

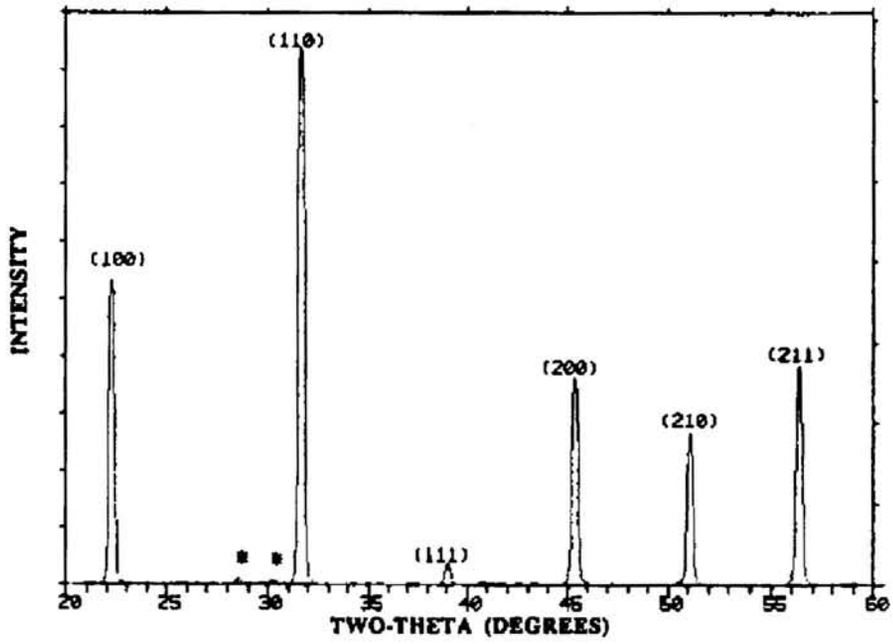


Figure 7-5 X-ray diffraction of annealed KTN (64/36) sol-gel powder with 15% excess K. The (*) denotes the secondary phase, the indexed peaks representing the perovskite phase.

The lattice parameters of KTN with different compositions were determined by powder X-ray diffraction. Table 7-2 lists three distinct compositions synthesized by sol-gel process.

Table 7-2 Lattice constants of sol-gel derived $KTa_{1-x}Nb_xO_3$ powders.

Composition (x)	**Lattice constant (Å)**	**Crystal structure**
0.90	a = 5.688, b = 5.716, c = 3.991	orthorombic
0.42	a = 3.999, c = 4.014	tetragonal
0.36	a = 4.000	cubic

7.1.7 Results obtained from hot isostatic pressing of powders

The HIPing process consists of applying a high isostatic pressure at a high temperature in order to sinter powders to full density using either an inert gas or oxygen as the pressurizing medium. A suitable pressure-tight encapsulation technique must be employed to ensure that the high gas pressure is transmitted to the powder during the HIPing cycle [7]. Our work was the first-time findings in HIP densification of KTN powders in the literature [8]. The alumina was at first used as a liner for the encapsulant to sinter KTN powder with KO_2 excess, was found to be ineffective because alumina (Al_2O_3) reacted with KTN and contaminated the specimen, analyzed by EDS and electron

microprobe. BN (boron nitride), however, provided favorable results as a liner for the HIP can. Samples densified in Ar atmosphere had black surfaces possibly due to oxide decomposition (i.e. oxygen loss), inside the capsule. The oxygen atmosphere processing was more effective in maintaining high total oxygen partial pressure in the environment, to avoid the oxide decomposition. Densities of 95 % of theoretical were obtained in samples that contained 15 % K excess introduced by KO_2 additions. However, the presence of moisture-sensitive KO_2 powder with particle sizes greater than KTN powders is thought to inhibit higher densification. Surface layer of ceramic discs were found to be extremely KO_2-rich for KTN powders that contained 25, 55 or 100 at% K excess.

The HIP densification became more difficult as the concentration of KO_2 increased in the KTN powder. The HIP temperature and pressure were very critical in the densification of KTN. The density increased as the HIP temperature was raised to 1220 °C from 1150 °C under the same HIP pressure in dry oxygen environment. The cooling through 1000° to 845°C has to be done very slowly for potassium excess reaching 50% K because a eutectic reaction ($KNbO_3$+liquid) in the already densified sample causes a regional collapse and fracture. It was noted that a limited amount of excess K can be introduced into KTN discs through HIP cycles but this is achieved at the expense of achieving full densities. The stoichiometric KTN with full density was achievable by HIPing. Near full densities were possible for KTN powders containing 5 at% KO_2-excess or less. The HIPed KTN sample will be milky with a slight grayish tone in color when fully densified.

7.2 Sol-gel derived KTN thin films

KTN thin films with a composition $KTa_{.64}Nb_{.36}O_3$, were spun on r-sapphire, c-sapphire or silicon substrates from the KTN precursor. The pyrochlore phase was the only crystalline phase that formed in those films after pyrolysis at 350 °C for 30 min. in O_2 or H_2O/O_2 and the furnace annealing at 750 °C for 1 h in O_2 atmosphere. The perovskite mixed with pyrochlore phase was obtained when the films on r- or c-sapphire were rapid thermally annealed at 750 °C for 60 - 90 sec in nitrogen after the regular pyrolysis step.

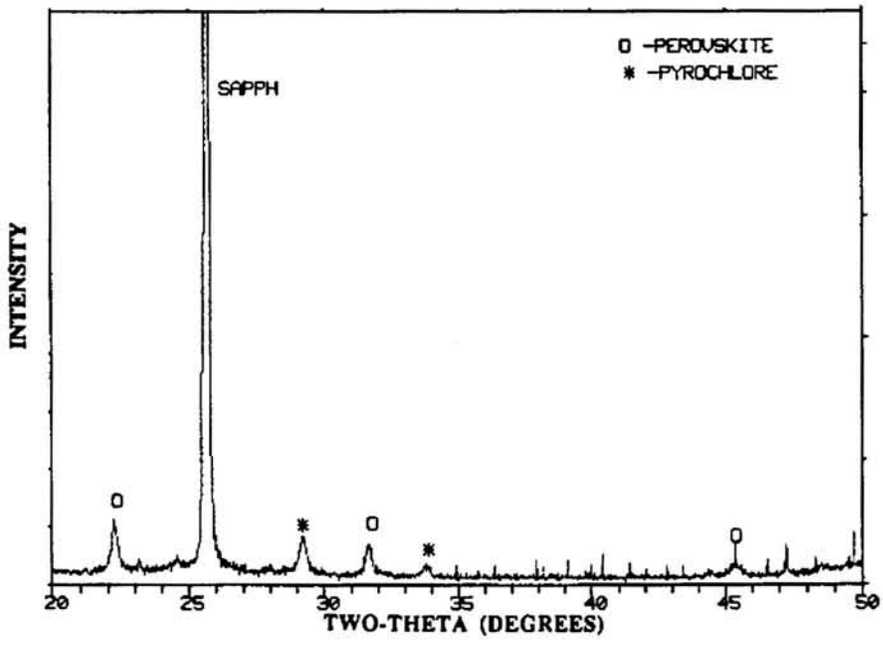


Figure 7-6 XRD pattern of sol-gel KTN thin film on r-sapphire after RTA.

Figure 7-6 shows the XRD pattern of spin-coated KTN thin film on r-sapphire which was rapid thermally annealed at 750 °C for 90 sec. It suggests that the perovskite

phase is nearly 55 % while the pyrochlore content is 45 %. The films on silicon did not yield to any perovskite phase, were purely pyrochlore and indicated some non-uniformities in composition of Nb and K as determined by RBS shown in Figure 7-7. The niobium probably diffused into the silicon substrate and K nonuniformity leading deficiency is noted. The films which exhibited perovskite did not have preferred orientation. The films had to be annealed at high temperatures after every second layer was spun. Otherwise, highly porous films resulted. The thin films were crack-free and did not have any adhesion problems.

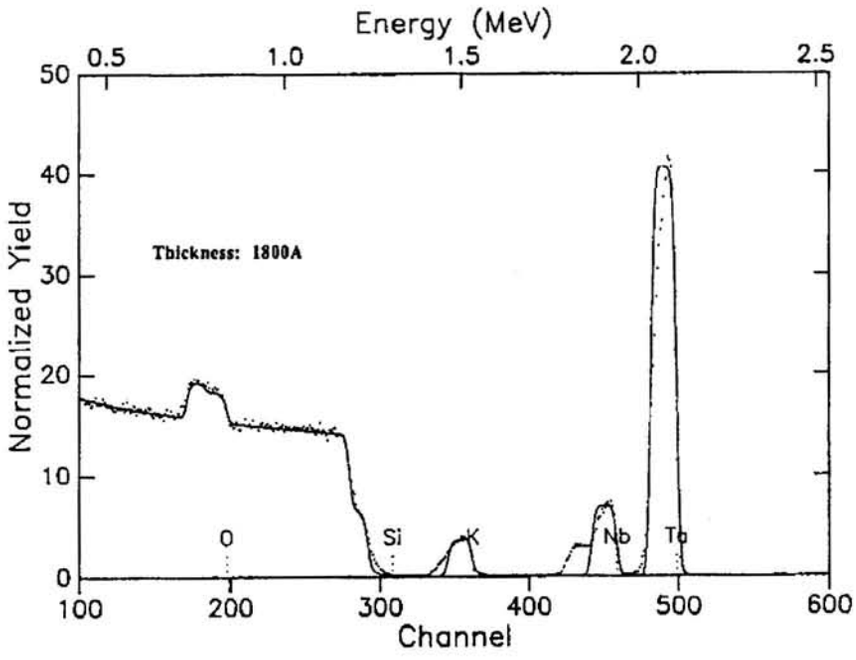


Figure 7-7 RBS spectrum of spin-coated KTN thin film on silicon substrate.

In summary, homogeneous, stable KTN precursors were prepared using metal alkoxides and potassium acetate in 2-methoxyethanol by controlled hydrolysis with 1:2 (Water/KTN) molar ratio. The results of XRD of KTN powders suggested that the crystallization started at or below 500 °C to first form pyrochlore phase and then perovskite phase at temperatures as low as 600 °C in oxygen atmosphere. The feasibility of using HIPing process to densify sol-gel derived fine KTN powders with correct stoichiometry (or with excess K) was demonstrated. The thin films spin-coated on r-sapphire and c-sapphire showed perovskite phase after RTA at 750 °C. The compositions were nearly retained after RTA anneal while films showed little K-deficiency after furnace anneal.

7.3 Magnetron sputtered KTN films

A Perkin Elmer 4400 sputtering machine was used for rf planar magnetron (PM) sputtering of KTN thin films. The substrates were heated during the deposition to ~ 600°-610°C by resistive heaters, and the deposition was done in argon ambient with a base pressure approximately 10 mTorr. Earlier investigations using this system with conventionally prepared targets led to potassium deficiencies as reported in reference [1]. The K-deficiency in the film was not solely due to evaporation during or post-deposition processing but also due to a nonstoichiometric target to begin with. Other researchers were also experiencing similar problems in physical vapor deposition of KTN films. The sputtering target had to possess a stoichiometric uniform composition at minimum, and

higher potassium contents in the targets were highly desirable, for successful deposition of optical quality stoichiometric KTN thin films. For this reason, we developed a sol-gel process to reproducibly derive fine, stoichiometric KTN powder over conventional methods to fabricate uniform, stoichiometric targets and subsequently densified them into compacts by hot-isostatic pressing, as explained in the previous section.

RF-PM sputtering, a dry deposition method, was chosen due to its compatibility with IC processing for film deposition of large grain, high preferred (PO), epitaxial (if not ideally single crystalline) films. PM sputtering at low power minimizes 'negative ion resputtering' effects seen in standard rf-sputtering. 'Preferential sputtering' effects in multicomponent KTN targets yield films of a different composition from that of the target due to differences in the atomic masses and binding energies of constituents. Further, differences in 'sticking coefficients' of the target constituents for a chosen substrate and deposition temperature result in the deficiency of one or more of the constituents in the film. With KTN, the Ta:Nb ratio in the target is generally replicated in the film. However, 'K' tends to be deficient in the film. To compensate for the deficiency, an excess of K were provided in the sputtered flux, via an excess of K in an appropriately enriched target. Accordingly, 10.16 cm (4-inch) diameter targets with nominal compositions of Ta in the range 60 to 66% with a 5-25 at% K excess were prepared. HIPing of KTN was developed in cooperation with Conway Tech. (Cleveland, OH).

R-plane $(10\bar{1}2)$ sapphire (for integration with SOS devices) and (100) GaAs were used as substrates commonly, some films were also deposited on platinized SiO_2/Si

substrates. The surface sublattice on GaAs (100), defined by the face centering lattice translation vectors, is lattice matched with KTN within 0.3% and promotes excellent epigrowth. However, the As tends evaporate above ~ 450°C during deposition from GaAs substrates leading to very rough surface thus rendering poor quality films. Therefore, a thin protective layer has to be deposited over GaAs substrate before depositition at high temperature, i.e. 600°C.

7.3.1 Composition and structure of sputtered KTN films

Fully perovskite KTN thin films after post-deposition in-situ annealing show highly transparent and colorless. The films on sapphire usually resulted in smoother surfaces as compared to films on GaAs or Pt/Si. The composition of the films was analyzed by RBS using 2.3 MeV He++ beam. RBS analysis of KTN on GaAs or sapphire can be done satisfactorily since there are no significant overlap among the atomic masses of the elements of the film and the substrate. However, Pt peak (z = 195) nearly overlaps with Ta peak thus the RUMP software simulation analysis would not be reliable. The Ga (z =69) and As (74) atomic masses can be separated from both Nb and K patterns in the analysis. The easiest analysis is the analysis of the film on sapphire due to light elements in the substrate, especially on very thin (< 0.3 μm) films.

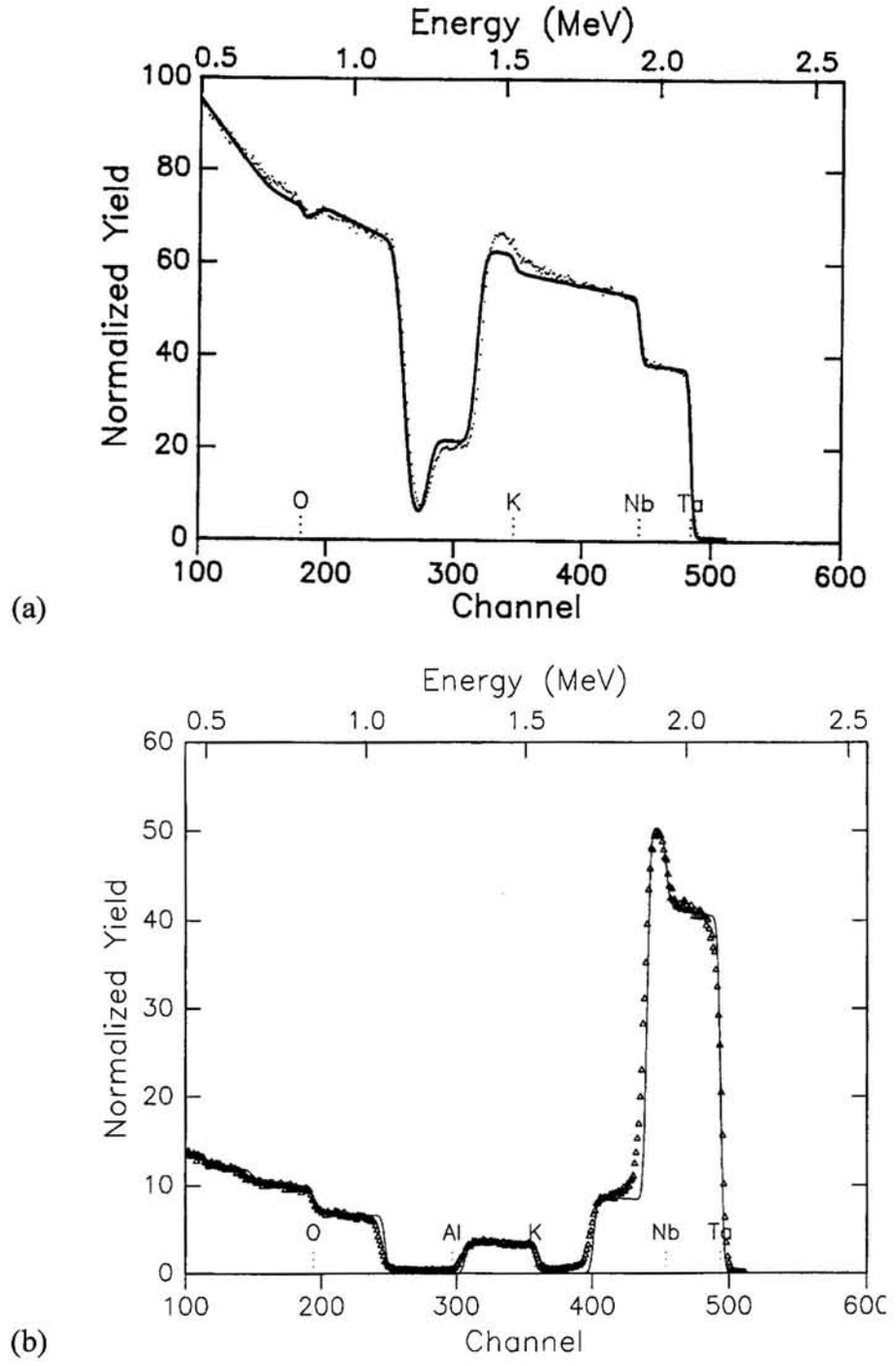


Figure 7-8 RBS spectra of sputtered KTN films on GaAs (a) and sapphire (b) substrates. The film thicknesses are 1.45 μm (a) and 0.55 μm (b) respectively.

Figure 7-8 (a) shows RBS spectrum of 1.45 μm-thick KTN film on GaAs substrate. the film composition was determined to be $K_{0.8}Ta_{0.58}Nb_{0.72}O_{2.90}$. The sensitivity of the analysis to oxygen is very low so it has to be treated with caution. The film reflected the target composition except for the potassium deficiency. The in-situ annealed (700°C) film of 0.55 μm on sapphire analyzed showed potassium deficiency again, with a composition $K_{0.70}Ta_{0.61}Nb_{0.39}O_3$, deposited from different target (Figure 7-8 (b)).

The films with higher nominal Ta ratios indicated similar trends. Films significantly deficienct in 'K' had rough surfaces and pinholes throughout the surface. Some local areas on the surface were observed to be etched away even for as-deposited films, which suggest that negative ion sputtering may be taking place during sputtering.

X-ray diffraction of KTN films indicated fully oriented (100) films on r-sapphire substrate (Figure 7-9 (a)). Perovskite structure was obtained for the as-deposited film (deposition at 600°-610°C), however, trace quantities of pyrochlore ($K_2Ta_2O_6$) observed could be eliminated by post-deposition anneal in O_2 for 1 h. The films deposited on GaAs at 550°C and annealed showed perovskite peaks but were not oriented. However, films were (200) oriented after depositing at 605°C and post-annealing (Figure 7-9 (b)).

When KTN films were in-situ annealed in the sputtering chamber from 700°C to 715°C, the films were observed to be fully oriented on both sapphire and GaAs substrates. The problem with this though is the unacceptably high potassium evaporation.

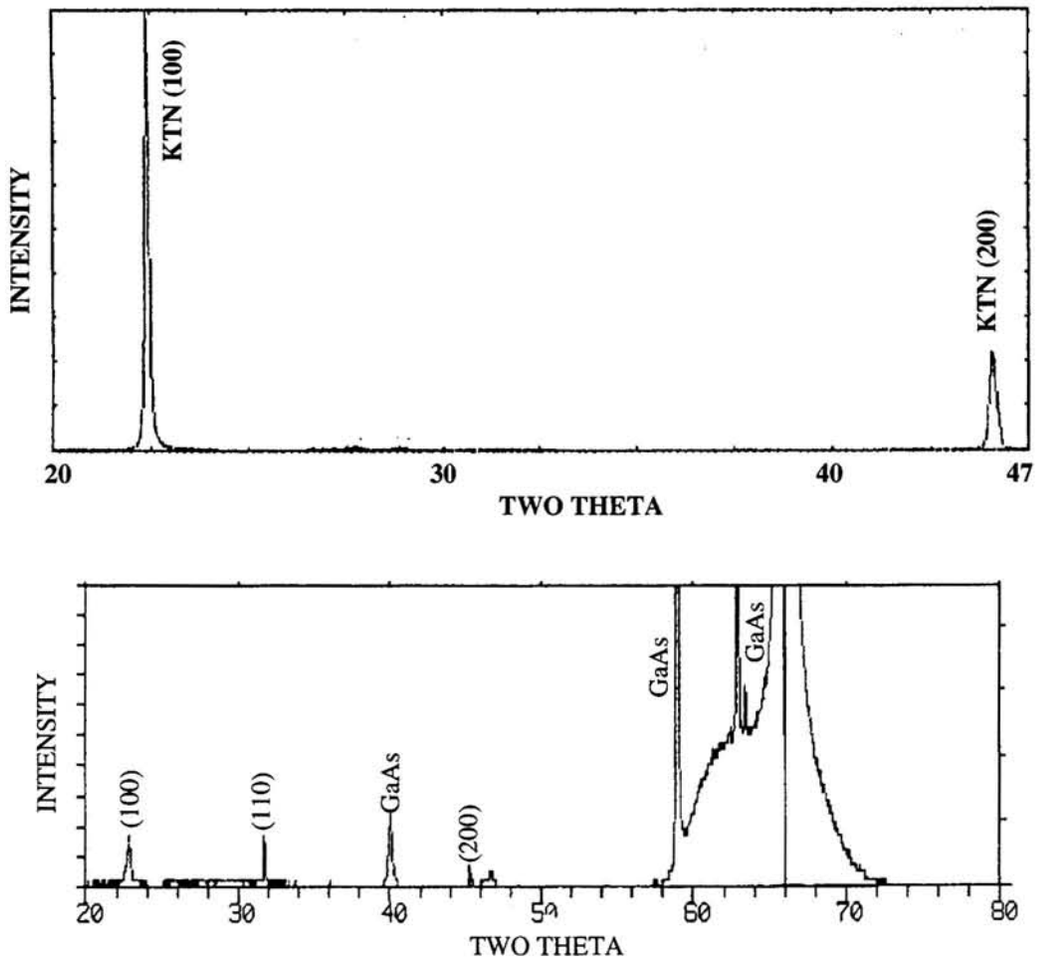


Figure 7-9 XRD patterns of sputtered KTN films on sapphire (top) and GaAs (bottom) substrates.

7.3.2 Electrical and optical properties of sputtered KTN films

Dielectric constant as a function of temperature of KTN film on $Pt/SiO_2/Si$ substrate at 200 Hz and 20 kHz is shown in Figure 7-10. The measurement was done by using parallel plate capacitor structure. The peak of the curve is at approximately 80°C with max of 390, with a broad transition. This peak point can be assumed to be the Curie

temperature. This value is fairly small as compared to bulk and other literature values. After the Curie point the curve tails off as expected but rises again after 126°C and continue to rise up to 210°C.

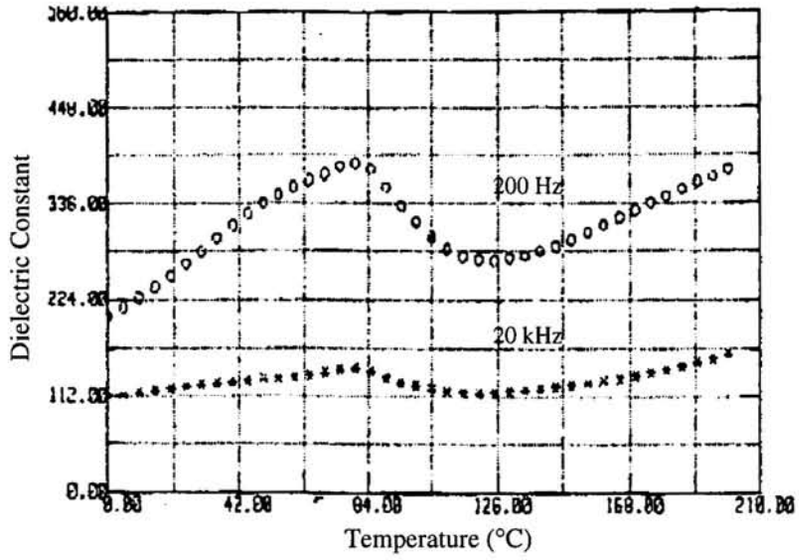


Figure 7-10 Dielectric constant vs. temperature curve for KTN film on GaAs substrate.

Similar kind of Curie behavior is also seen films on sapphire, as shown in Figure 7-11 (a), much more dramatically at 10 kHz and 20 kHz for very thick film of 2.6 μm. The film ε value is nearly 5000 at 150°C and rises to a huge value of 35000 near 300°C. The curve shows no Curie peak at lower temperatures but ε continuously rises. This is an anomaly that has not been reported in literature in any ferroelectric system. From the composition, it is expected that a Curie point be near to room temperature. The ε and tan δ are plotted vs. frequency shows that there is strong frequency dispersion and ε becomes few hundred at higher frequencies, 1 Mhz, (Figure 7-11 (b)). The dielectric loss seems to be fairly high

in the film, peaking at 4%. A low peak ε of 200 was previously reported for KTN film on GaAs but with a sharp Curie transition at 4°C [9]. The reason was attributed to poor crystalline quality or poor contact with the electrodes.

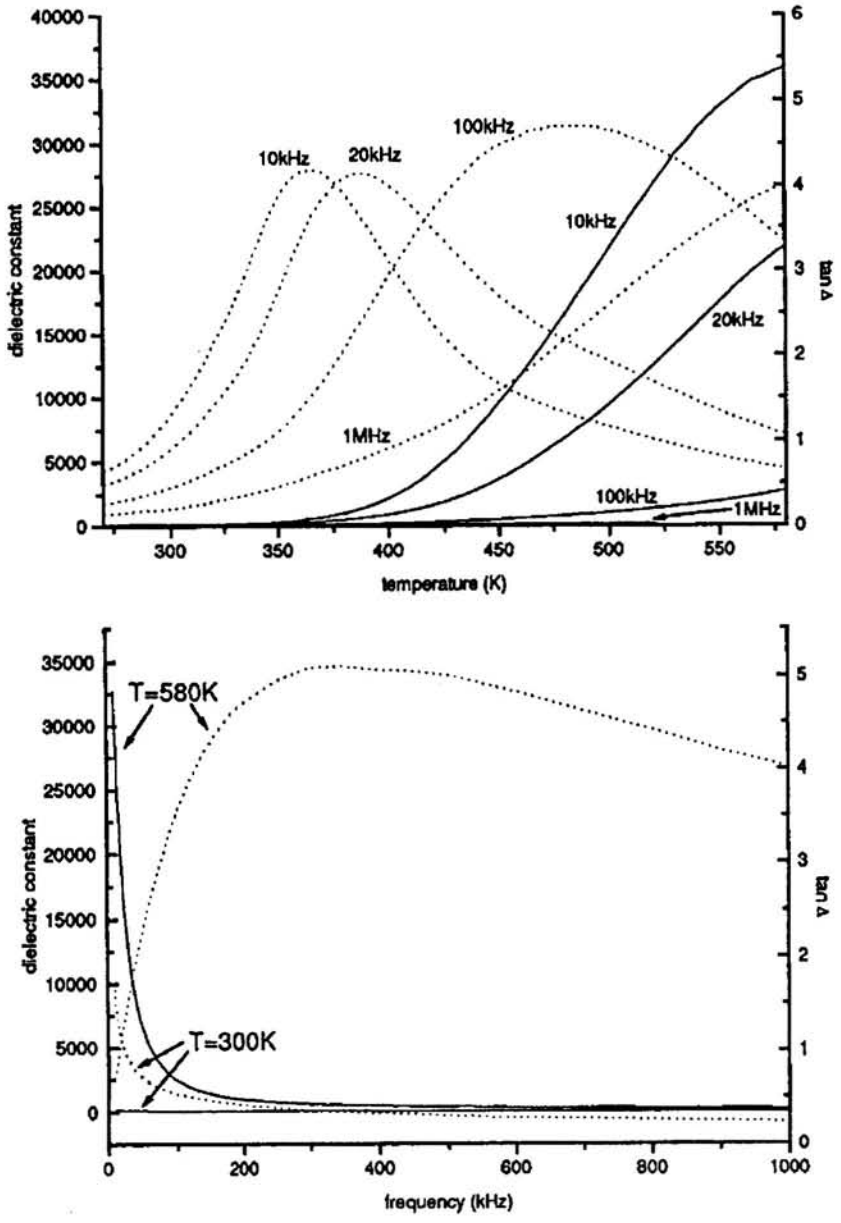
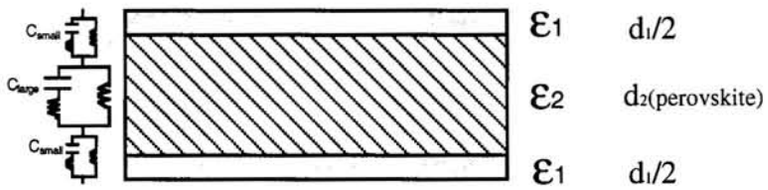


Figure 7-11 Dielectric constant as a function of temperature (top) and frequency (bottom) for a 2.9 μm-thick KTN film on sapphire. The solid lines are dielectric data and dotted lines are tan delta measurements.

The 'K' deficiency in the film is prevalent in the films and it is probable that the surface is especially depleted with 'K^{+}' and also 'O^{2-}' for charge compensation. Thus a defect layer on the surface forming with a low or highly conductive (ionic) which would result in a formation of a Schottky capacitor in series with the capacitance of the perovskite structure with high capacitance. In such a case (see Figure 7-12, the sketch on the left is the capacitor equivalent circuit with series and leakage resistors, d_i : thickness), the low-ε_i layer will dominate the capacitance, effectively reducing the total dielectric constant of the perovskite film (ε).The dielectric loss is high in the films because of ionic conductivity due to defects formation (K and O vacancies). Although the space charge associated with the electrode/film interface would also alter the capacitance by injecting electrons into the film, it is still difficult to account for increasing dielectric constants at higher temperatures. However, the interface of the film with sapphire is expected to be relatively defect-free as compared to Pt-interface which is known to react more easily. Another possibility is that the space-charge could also be throughout the grain boundaries rather than localized just at the surface. A similar series capacitance formula would hold, effectively lowering the dielectric constant.

Further analysis of the electrical behavior, I-V, C-V studies along with cross-sectional transmission microscopy may shed more light into the interface betweeen ferroelectic KTN films and metal/insulating substrates. Additional work is continuing to characterize the dielectric behavior of the KTN films on sapphire with IDE electrodes.



$$\frac{d}{\varepsilon} = \frac{d_1}{\varepsilon_1} + \frac{d_2}{\varepsilon_2} \quad \text{and} \quad d = d_1 + d_2$$

Figure 7-12 Model structure for a large permittivity perovskite film (ε_2) in series with low permittivity capacitor layers.

Optical reflectance measurements were done using light chopped from a monochrometer coupled with a grating scanning wavelengths ranging from 800 nm to 1150 nm. The chopped light was detected using a silicon photodiode and a lock-in amplifier. A plot of reflectance spectrum of three KTN films on sapphire is given in Figure 7-13 (top), with respect to bare sapphire substrate. Simulations of the light reflected from the KTN film on sapphire were performed by fitting the peaks and valleys of the reflectance spectra. The refractive indices of films thus can be obtained by simulation, as shown in Figure 7-13 (b). The thickness of the films can be extracted as well as the relative density of the films, as noted on the plot. It is seen that KTN 12 showed the lowest density 48% also has the lowest refractive index, 1.60, as compared to other two samples. The film K deficiency seems to correlate well with the results from reflectance measurements. Thicker and denser KTN films showed refractive indices between 2.00 to 2.05, in agreement with the findings on KTN on silicon [9]. The refractive index increases as the

film density increases. The dispersion in refractive index between 800 nm and 1150 nm is negligible.

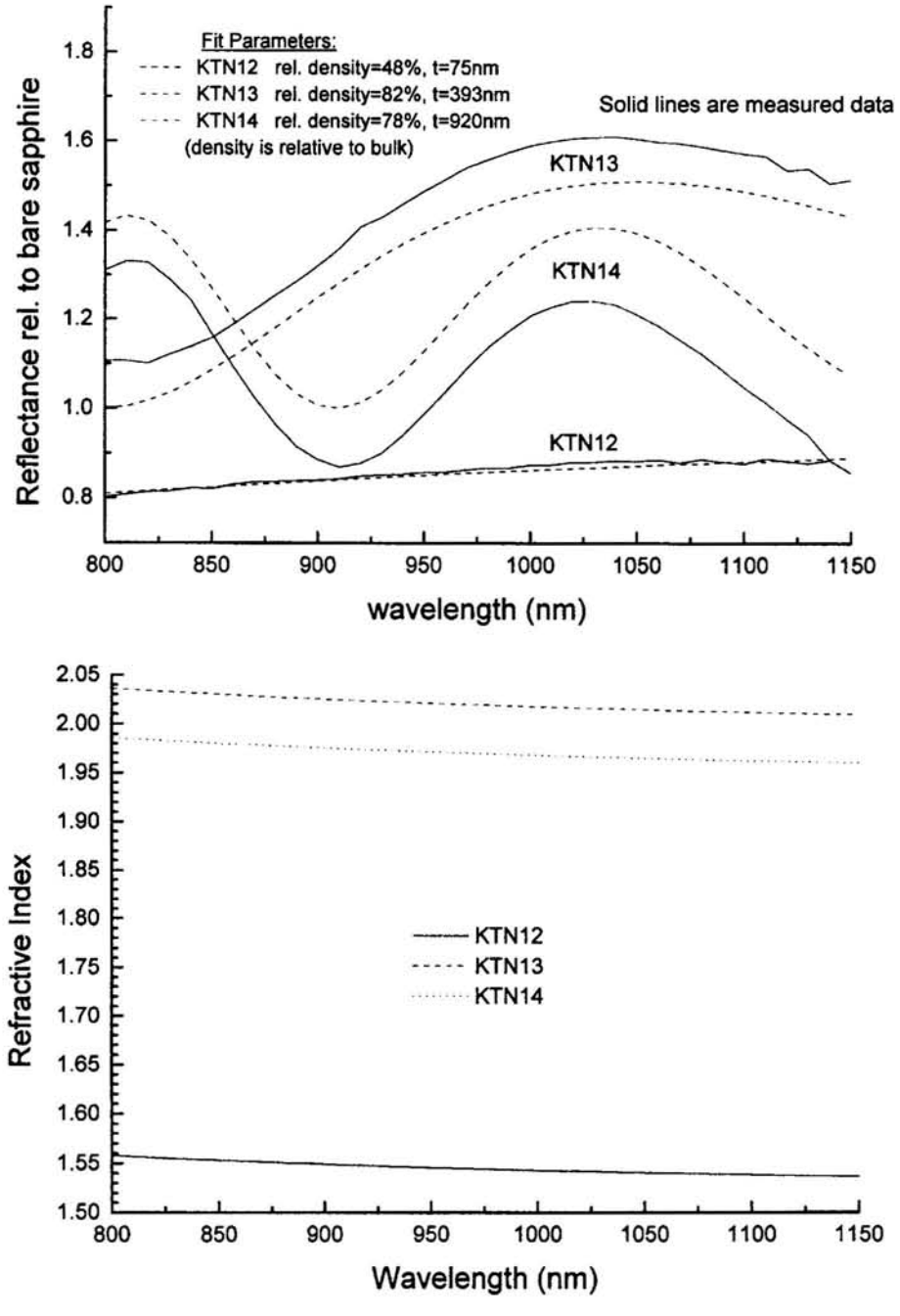


Figure 7-13 Reflectance of KTN films of various thickness on sapphire (top) and the refractive index vs wavelength curve for the films (bottom) obtained through simulation.

We have developed a scheme to produce sol-gel derived powders and fabricate ceramic KTN targets by HIPping that would be useful for any physical deposition process. The 'K' deficiency issue was addressed and solved for targets, however the sputtered films still indicated potassium deficiencies due to the nature of the process. Different sputtering geometries should be used in further investigations.

Spin-on films have very low densities and very small grain sizes and therefore they are not preferable to denser physically deposited films. There is no known etchant to etch KTN surfaces evenly to reveal the grain boundaries. Some strong acid mixture attack KTN at >200°C but quite unevenly leaving pits on the surface. The crystallite size can then only be estimated up to 200 nm by x-ray line broadening measurements. Sol-gel films had large density of pinholes that gave rise to electrical shorts in capacitance measurements. The sputtered films, however, were usually much denser. Chemical deposition processes can be attractive to grow KTN films, perhaps MOCVD, provided that appropriate precursors are available and environmentally safe. MOD-grown films, however, required very high annealing temperatures (~ 1000°C) uncompatible with IC processing and resulted in very porous films so far. R-sapphire seems to be the best substrate to grow high quality KTN films, for compatibility with silicon technology. The KTN films on Pt/Si or GaAs usually have poorer optical and electrical properties.

In summary, homogeneous KTN solutions were prepared using potassium acetate and metal alkoxides in 2-methoxyethanol by controlled hydrolysis with 1:2 (KTN/H_2O) molar ratio. The results of XRD from KTN powders suggest that the crystallization

started just below 500°C to first form pyrochlore phase ($K_2Ta_2O_6$) and then perovskite phase at temperatures as low as 600°C in oxygen atmosphere. The feasibility of using HIP process to densify sol-gel derived fine powders with correct stoichiometry was demonstrated. The spin-on KTN films on r-sapphire and c-sapphire showed perovskite phase after RTA at 750°C. The composition were nearly retained after RTA processing while films showed some K-deficiency after furnace anneal. Sputtered films ususally had potassium deficiency despite the use of stoichiometric sputtering targets. The transparency of the films were very good and the refractive indices were found to be in the range of 1.55 to 2.05 depending on the film density. The film thicknesses were in the range of 1 to 3 μm. The dielectric constant at room temperature for KTN on Pt/Si was about 250 and increased after the Curie temperature slope to very high values. This was attributed to space charge layers formed at the film/electrode interface or possibly a low ε layer around grain boundaries which shows temperature-dependent characteristic. Further studies of structural interfaces in KTN films will shed more light into the anomaly in its dielectric behavior.

References

1 S. R. Sashital, S. Krishnakumar and S. Esener, "Synthesis and characterization of rf-planar magnetron sputtered $KTa_{1-x}Nb_xO_3$ thin films," *Appl. Phys. Lett.*, **62**, 2917, 1993.

2 S. Yilmaz, R. Gerhard-Multhaupt, W. A. Bonner, D. M. Hwang, A. Inam, J. A. Martinez, T. A. Ravi, T. Sands, B. J. Wilkens, X. D. Wu and T. Venkatesen, "Electro-optic potassium-tantalate-niobate thin films prepared by pulsed laser deposition from segmented targets," *J. Mater. Res.*, **9**, 1272, 1994.

3 E. T. Wu, A. X. Kuang and J. D. MacKenzie, "Hot-pressed KTN prepared from ultrahomogeneous oxide powders derived by sol-gel technique. II. Ceramics," Proc. IEEE 6th Int. symp. Appl. Ferroelectrics, p. 391, 1986.

4 D. D. Liu, J. G. Hu, R. C. Pastor and O. M. Stafsudd, "Sol-gel derived stoichiometric KTN," *Mater. Res. Bull.*, **27**, 723, 1992.

5 S. Hirano, T. Yogo, K. Kikuta, T. Morishita and Y. Ito, " Preparation of potassium tantalate niobate by sol-gel method," *J. Am. Ceram. Soc.*, **75**, 1701, 1992.

6 A. Nazeri and M. Kahn, "Preparation of $KTaO_3$ and $KNbO_3$ solid solutions through sol-gel processing," *J. Am. Ceram. Soc.*, **75**, 2125, 1992.

7 D. J. Stephenson and M. Downing, "Hot-isostatic pressing of PM and cast components," *Mater. High Temp.*, **9**, 59, 1991.

8 B. Tunaboylu, C. Fan and S. C. Esener, "Synthesis of sol-gel bulk and thin film $KTa_{1-x}Nb_xO_3$," Proc. III. Int. Ceramic Cong., vol. **2**, p. 349, 1996.

9 S. Krishnakumar, PhD Thesis, University of California, San Diego, 1993.

8. Summary and conclusions

The growing complexity and density of Si very large scale integrated (VLSI) circuits are providing greater electronic computing power, but at the same time, they place greater requirements on interchip and intrachip communication capabilities. Free-space optical interconnects offer an attractive alternative to electrical interchip linkages because they allow for the interconnection of many thousands of internal nodes. A basic active element of such interconnects is the SLM which for best performance should be integrated with logic circuits and have low-power dissipation with a large fan-out. Electrooptic light modulators are prime candidates at present with their large spectral width and low-power dissipation characteristics as compared to MQW modulators or other alternatives such as VCSELs (Vertical Cavity Surface Emitting Lasers) or light emitting diodes.

Ferroelectric materials such as PLZT and KTN offer great advantages since they possess high electro-optic coefficients and are transparent over a large spectral width. They can provide large dynamic range and fanout required for efficient interprocessor communication. They can reduce the thermal dissipation requirements in the design of a smart pixel within a system while improving temperature stability of individual light modulating elements by reducing the 'off' state absorption.

Among the methodologies for the integration of ferroelectrics with electronic substrates, the 'flip-chip' technique is a bulky hybrid method relying on indium bumps for alignments and connections and thus serves only as a short-term solution. However it

was shown that the performance of bulk PLZT modulators is limited by energy requirements due to large capacitances. Therefore the monolithic methods using thin films seems to be indispensable for better long-term prospects.

The ferroelectric thin films must show high optical quality with good dielectric and electrooptic properties. RF magnetron sputtering is highly favored because the technique yields films with good compositional uniformity, transparency and orientation. A high density multicomponent-singular target serves as an important starting point in depositing optical quality thin films, and with correct sputtering geometry it produces highly dense films as compared to other dry or wet deposition techniques. PLZT targets were commercially hot-pressed (dia. 5.715 cm - 2.25″) while larger KTN targets had to be hot isostatically pressed to produce near stoichiometric targets. In order to get right compositions in the deposited films, it is necessary to introduce excess amounts of the volatile components of the multicomponent ferroelectric in the sputtering targets. The volatile components were lead and potassium in PLZT and KTN systems, respectively.

PLZT and KTN thin films were both deposited by magnetron sputtering and compositions were analyzed and and optimized mainly through the use of RBS. The PLZT films were deposited at low deposition temperatures (< 500°C) to control Pb content as a mixture of crystalline phases and later annealed by either furnace annealing or rapid thermal annealing to obtain single-phase perovskite structure.

Generally, PLZT films with identical compositions showed a nearly cubic structure with a very small tetragonal distortion after RTA but were cubic after furnace annealing in

lead-rich oxygen atmosphere. This is reflected in x-ray diffraction measurements. The difference in electrical properties of films is also notable as furnace annealed films showed higher dielectric constants than that of RTA. PLZT films with peak dielectric constants in the order of 2800 and room-temperature values of 2200 were observed in the furnace annealed film. Films after RTA showed smaller peak dielectric constants, around 1200 but with very low loss factors, 0.02. PLZT films on sapphire annealed by either method were characterized by a very good low-frequency dispersion in dielectric constants over 10 kHz to 1 MHz range. Films showed small hysteresis loops in dielectric constant measurements with negative and positive bias voltage. Slimmer loops are desirable with respect to operation speeds in devices.

Optical quality in PLZT films was very high before and after annealing in both cases and the yellow color of deposited films turned colorless upon conversion to perovskite. The refractive indices of the PLZT films on sapphire were in the range of 2.2 to 2.5 which are comparable to bulk values. The films also had very low absorption. The electro-optic response of the furnace annealed PLZT film which was deposited at 490°C was truly remarkable, an unparalleled value of optical phase retardation which is nearly nearly five times that of bulk PLZT ($R_{film}=20x10^{-16}$ $(m/V)^2$. Films deposited at lower temperature (450°-475°C) however showed EO response similar to EO coefficient values reported earlier, $0.7x10^{-16}(m/V)^2$. The electrooptic effect in RTA-processed films were much smaller, in conformity with dielectric measurements.

The pyrochlore to perovskite transformation kinetics was found to be a process with an Avrami reaction order of $n < 2$ and the activation energy formation of perovskite was determined to be 322 kJ/mol. The transformation reached completion in 3 min at 730°C (RTA) while it took much longer at lower RTA temperatures. The nucleation of large number of crystallites at very low deposition temperatures (amorphous/crystallites mixture) gave rise to smaller grain sizes in the films after annealing for both annealing methods. However, films deposited at high deposition temperatures (> 450°C) the grain size was again uniform but larger. The grain size of RTA-processed PLZT films were in the order of 0.1 to 0.8 μm while that of furnace annealed ones were in the range of 0.3 to 1.6 μm depending on deposition/annealing conditions. We believe that differences in dielectric and EO properties of PLZT films annealed by two methods are the result of differences in grain sizes and possibly residual stresses.

Sol-gel derived fine and stoichiometric powders were used in making sputtering targets for depositing KTN films. Spin-on KTN films were deposited on several substrates and perovskite formation was observed in films on sapphire after RTA processing one layer at a time. Films showed pinholes though due to lower densities as compared films derived from sputtering. Hot-isostatic pressing of KTN was developed in collaboration with a company using sol-gel powders and targets of 1-inch (2.54 cm) to 5-inch (12.7 cm) in diameters were successfully densified to high densities. The sputtered KTN films usually had potassium deficiency despite the stoichiometric or slightly potassium enriched targets. The refractive indices were found to be in the range of 1.55 to

2.05 depending on the film density. The film thicknesses were in the range 1 to 3 μm. The dielectric constant at room temperature for KTN on Pt/Si was about 250 and increased dramatically at higher temperatures. This was attributed to space charge layers forming at the film/electrode interface or possibly a low ε layer around grain boundaries which shows a temperature-dependent characteristic. Therefore, further studies of structural interfaces in KTN films are needed to understand the anomaly in its dielectric behavior.

Based on the investigation in this thesis, RF-magnetron sputtered PLZT thin films clearly lead the competition for electrooptic materials for SLMs. For successful integration of these films onto high performance systems, large arrays of modulators in these films should be developed next. Therefore, large (i.e. 25.4 cm - 30.48 cm, 10″-12″) sputtering targets should be used for depositing uniform large-size films. The r-plane sapphire is an ideal substrate for growing high quality PLZT films which allows for transmissive mode modulators. PLZT films deposited at substrate temperatures above 480°C exhibited paired-plates across the surface after annealing and more work needs to be done to understand the formation of such plate-like structures as well as their orientational relationships with the substrate. This presents a novel area of research in ferroelectric PLZT films which may be unique to sputtered films.

Sol-gel KTN films showed large density of pinholes that gave rise to electrical shorts in capacitive measurements. Therefore, much thicker films should be deposited using dip-coating rather than spin-on technique. On the other hand, the sputtered films were usually much denser. In addition, further analysis of the electrical behavior studies are necessary

along with studies of cross-sectional interface of the FE film/insulating and metal substrates. The space charge at the interface should be studied to understand the anomalous dielectric constant behavior as a function of temperature. Alternative to two methods used here, other chemical deposition processes can be suitable to grow KTN films, perhaps MOCVD, provided that appropriate precursors are available and environmentally safe.

Dynamic range of light modulation in thin films can be increased by the use of Fabry-Perot structure. The EO-film should be placed in a self-tuned Fabry-Perot structure with a bottom reflective mirror on the back side of the substrate for best modulation efficiency. Finally, future thrust of the research should be the demonstration of FE thin-film based large arrays of modulators.

APPENDIX

The treatment of electro-optic (EO) effects in crystals for various structures was given by Yariv and Yeh[1]. We present in the following two sections the treatment of electro-optic effects in the cases of a cubic and a tetragonal structure, assuming stress-free crystals (no piezoelectric component), using the equations provided by Yariv and Yeh. It is well known that the optical properties of a crystal are characterized by the index-ellipsoid, or optical indicatrix, defined as

$$\frac{x^2}{n_1^2}+\frac{y^2}{n_2^2}+\frac{z^2}{n_3^2}=1 \qquad (1a)$$

where n_1, n_2, n_3 are the principal refractive indices. The EO effect consists in a distortion of the indicatrix under the influence of electrical field. The equation of the index ellipsoid (deformed indicatrix) in the presence of an electric field can be written[1]

$$\left(\frac{1}{n_x^2}+r_{1k}E_k\right)x^2+\left(\frac{1}{n_y^2}+r_{2k}E_k\right)y^2+\left(\frac{1}{n_z^2}+r_{3k}E_k\right)z^2 \qquad (1b)$$

$$+2yzr_{4k}E_k+2zxr_{5k}E_k+2xyr_{6k}E_k=1$$

where E_k (k = 1, 2, 3) is a component of the applied electric field and summation over repeated indices k is assumed. Here 1, 2, 3 correspond to the principal dielectric axes x, y, z and n_x, n_y, n_z are the principal refractive indices. The dimensions and orientation of ellipsoid (eq. 1a) are dependent on the direction of applied field as well as the matrix elements r_{lk}. From Yariv and Yeh, the quadratic electrooptic tensor for a cubic crystal is given as

$$\begin{pmatrix} s_{11} & s_{12} & s_{13} & 0 & 0 & 0 \\ s_{12} & s_{11} & s_{13} & 0 & 0 & 0 \\ s_{13} & s_{13} & s_{33} & 0 & 0 & 0 \\ 0 & 0 & 0 & s_{44} & 0 & 0 \\ 0 & 0 & 0 & 0 & s_{44} & 0 \\ 0 & 0 & 0 & 0 & 0 & s_{44} \end{pmatrix} \qquad (2)$$

where quadratic EO coefficients $s_{13}=s_{12}$ and $s_{11}=s_{33}$ for cubic PLZT. For an isotropic medium an applied E-field defines the optic axis. The equation of index ellipsoid can be obtained from eq 1b & 2 in the presence of an E-field.

1. PLZT : Using eq. 1b and 2, the index ellipsoid of cubic PLZT is given by [Yariv&Yeh] the following equation by choosing electric field in the z-direction [001], E // E_z.

$$x^2\left[\frac{1}{n^2}+s_{12}E_z^2\right]+y^2\left[\frac{1}{n^2}+s_{12}E_z^2\right]+z^2\left[\frac{1}{n^2}+s_{11}E_z^2\right]=1 \qquad (3)$$

---

[1] A. Yariv and P. Yeh, "Optical Waves in Crystals," John Wiley and Sons, Chp. 7, 1984.

This index ellipsoid can be written as

$$\frac{x^2+y^2}{n_o^2}+\frac{z^2}{n_e^2}=1$$

$$n_o = n-\frac{1}{2}n^3 s_{12}E_z^2$$

$$n_e = n-\frac{1}{2}n^3 s_{11}E_z^2$$

The birefringence (n_e-n_o) becomes

$$\Delta n = n_e - n_o = \frac{1}{2}n^3(s_{12}-s_{11})E_z^2 \qquad (5)$$

where s_{12}-s_{11} = R, n_o is the index of refraction of light polarized normal to the E-field and ne is the index of refraction for light polarized in the direction of E.

Phase retardation (Γ) of light is

$$\Gamma = \Delta n\left(\frac{2\pi}{\lambda}t\right)$$

$$\Gamma = \left(\frac{2\pi}{\lambda}t\right)\left(\frac{1}{2}n^3 RE^2\right) \qquad (6)$$

where t is the thickness of the medium and is the wavelength of the light.

2. Derivation of linear electrooptic effect in KTN.

The EO tensor for tetragonal (4mm) KTN is given by [Yariv and Yeh]

$$\begin{pmatrix} 0 & 0 & r_{13} \\ 0 & 0 & r_{13} \\ 0 & 0 & r_{33} \\ 0 & r_{51} & 0 \\ r_{51} & 0 & 0 \\ 0 & 0 & 0 \end{pmatrix} \qquad (7)$$

Case 1. Assume E-field is along c-axis [001], E // E_z, and optical propagation is along a-axis (x-axis) of the crystal. From eq. 1b and eq. 7 [Yariv and Yeh], it can be written

$$\left(\frac{1}{n_o^2}+r_{13}E\right)x^2+\left(\frac{1}{n_o^2}+r_{13}E\right)y^2+\left(\frac{1}{n_e^2}+r_{33}E\right)z^2=1 \qquad (8)$$

Since no mixed terms appear, the principal axes of the new index ellipsoid remain unchanged.

$$\frac{1}{n_x^2}=\frac{1}{n_o^2}+r_{13}E_z, \frac{1}{n_y^2}=\frac{1}{n_o^2}+r_{13}E_z \text{and}$$

$$\frac{1}{n_z^2}=\frac{1}{n_e^2}+r_{33}E_z$$

then using the relation

$$d\left(\frac{1}{n^2}\right) = -2n^{-3}dn$$

$$\Delta n = -\frac{n^3}{2}\Delta\left(\frac{1}{n^2}\right)$$

and

$$n_x = n_o - \frac{n_o^3}{2} r_{13} E_z$$

$$n_y = n_o - \frac{n_o^3}{2} r_{13} E_z \qquad (9)$$

$$n_z = n_e - \frac{n_e^3}{2} r_{33} E_z$$

$$\Delta n = n_z - n_y = (n_e - n_o) - \frac{1}{2}\left(n_e^3 r_{33} - n_o^3 r_{13}\right)E$$

Phase retardation can be easily found using the birefringence equation 9 for this case.

Case 2. E-field is along a-axis [100] direction ($E//E_x$), the optical propagation along c-axis. The eq 1b. becomes

$$\frac{x^2}{n_o^2} + \frac{y^2}{n_o^2} + \frac{z^2}{n_e^2} + 2zx r_{51} E = 1 \qquad (10)$$

The mixed term zx indicates that there is a rotation about the y axis. The present equation is converted to

$$\frac{x'^2}{n_x^2} + \frac{y'^2}{n_y^2} + \frac{z'^2}{n_z^2} = 1 \qquad (11)$$

and y' = y and we need to rotate in the x, z plane

$x = x' \cos\theta - z' \sin\theta$

$z = x' \sin\theta + z' \cos\theta$

the equation 11 becomes

$$\left(\frac{x'\cos\theta - z'\sin\theta}{n_o^2}\right)^2 + \left(\frac{x'\sin\theta + z'\cos\theta}{n_e^2}\right)^2$$

$$+2[x'\cos\theta - z'\sin\theta][x'\sin\theta + z'\cos\theta] r_{51} E = \frac{x'^2}{n_x^2} + \frac{z'^2}{n_z^2}$$

comparing coefficients of x'z', x'^2, z'^2

$$\frac{-x'z'\sin 2\theta}{n_o^2} + \frac{y'z'\sin 2\theta}{n_e^2} + 2x'z'\cos 2\theta r_{51} E = 0$$

$$\tan 2\theta = \frac{r_{51}E}{2\left[\frac{1}{n_o^2} - \frac{1}{n_e^2}\right]}$$

and r_{51} is small and also the right hand side is small. Taking ($\tan 2\theta \sim \theta$), following approximation is obtained

$$2\theta = \frac{r_{51}E}{2\left[\frac{1}{n_o^2} - \frac{1}{n_e^2}\right]} \qquad (12)$$

Using the substitutions $\cos 2\theta \approx 1$ and $\sin 2\theta \approx 2\theta$ and x'^2 equations, the following can be written

$$\frac{1}{n_o^2} + \frac{1}{2}\frac{r_{51}^2E^2}{\left(\frac{1}{n_o^2} + \frac{1}{n_e^2}\right)} = \frac{1}{n_x^2}$$

$$n_x = n_o - \frac{n_o^3 r_{51}^2 E^2}{2\left(\frac{1}{n_o^2} + \frac{1}{n_e^2}\right)}$$

$$n_y = n_o$$

$$\Delta n = \frac{n_o^3 r_{51}^2 E^2}{2\left(\frac{1}{n_o^2} + \frac{1}{n_e^2}\right)}$$